12-2014

UNUSUALLY LOW THERMAL CONDUCTIVITY IN THE ARGYRODITE Ag8GeTe6 ATTRIBUTED TO STRONG ANHARMONICITY

Dale Hitchcock
Clemson University, daleh@g.clemson.edu

UNUSUALLY LOW THERMAL CONDUCTIVITY IN THE ARGYRODITE Ag_8GeTe_6 ATTRIBUTED TO STRONG ANHARMONICITY

A Dissertation
Presented to
the Graduate School of
Clemson University

In Partial Fulfillment
of the Requirements for the Degree
Doctor of Philosophy
Physics

---

by
Dale Austin Hitchcock
December 2014

Accepted by:
Dr. Jian He, Committee Chair
Dr. Murray Daw
Dr. Terry Tritt
Dr. Apparao Rao
Dr. Catalina Marinescu

ABSTRACT

Arguably the main focus of thermoelectric materials research over the last decade has been the reduction of lattice thermal conductivity through nanostructuring. This approach has proved quite effective in many instances, but has several inherent drawbacks including not only the metastability of many of the nanostructures used, but also difficulty decoupling the effects on the thermal properties of materials from the effects on their electrical properties. Some more recent research has focused on reduced thermal conductivity in materials with strong anharmonicity. In these systems anharmonicty in the crystal structure, whose strength can be gauged by the so-called Gruneissen parameter leads to amorophous–like thermal behavior in crystaline materials.

Ag_8GeTe_6 is one such material which displays an unusually low thermal conductivity (~0.25 W/m*K at room temperature) that can be at least partially attributed to its large mode-averaged Gruneisen parameter, which we have estimated to be ~3.8 at room temperature. Beyond the small magnitude of the thermal conductivity of Ag_8GeTe_6 its temperature dependence is also surprising, and displays a positive temperature coefficient rather than the usual *1/T* dependence expected for crystalline materials. Furthermore, Ag_8GeTe_6 is an unusual example of a material in which superionic conduction and promising thermoelectric performance coexist at 500 K and above. Such coexistence is a surprise as the crystal chemistry requirements for these two phenomena are distinct. Therefore understanding the interplay between the ionic, electronic, and phonon conduction in Ag_8GeTe_6 not only attracts interest in fundamental research but also bridges two realms of energy-related materials research, namely, thermoelectric

materials (electronic conductors for direct heat-to-electricity energy conversion) and electrolyte materials (ionic conductors for energy storage in batteries).

To better understand how Ag_8GeTe_6 evolves and sets the stage for such rare coexistence the coexistence of superionic conduction and promising thermoelectric performance at elevated temperatures, we have conducted temperature variable powder X-ray diffraction, photo-acoustic spectroscopy, heat capacity, thermal conductivity, electrical conductivity (DC and AC electrical conductivity, and ionic conductivity), Seebeck coefficient, and Hall coefficient measurements over a wide temperature range below room temperature. As previous studies on Ag_8GeTe_6 are scarce, these results have brought our understanding of Ag_8GeTe_6 to an unprecedented level.

DEDICATION

I would like to dedicate this work to two amazing women. Grandma Marie you were one of the first reasons I chose to study science and you are my greatest inspiration, and Kayla you are the reason I continue on this path. I love you both.

ACKNOWLEDGMENTS

The work here is the product of five years of research at Clemson University that could not have been accomplished without the help and support of many people.

First of all, I would like to thank my advisor, Dr. Jian He. For the last five years, he has been my greatest resource and mentor. From the moment he asked me to join his group, which consisted of only him at the time, he has gone out of his way to help me succeed. Furthermore, under his guidance, I think I can say that I have learned what it truly means to be a scientist. It has been an honor to be his first Ph.D student. I also need to thank Dr. Terry Tritt. When I came to him in search of a part-time job as an undergrad, I had no idea that it would lead to such a long and fruitful collaboration. Thank you for spurring my interest in condensed matter physics, and showing me what it means to be an experimentalist.

Next, I would like to thank the rest of my committee. Dr. Apparao Rao, Dr. Murray Daw, and Dr. Catalina Marinescu; thank you for your guidance and insight, and Dr. Rao thank you for giving me projects early in my grad school years, which ended up being the foundation of so much of my work.

I would also like to thank not only my own research group, Jian, Zhou, and Yufei, but also Dr. Tritt and Dr. Rao's groups. In particular, I need to thank Dr. Daniel Thompson and Dr. Tim Holgate, I consider you both not only colleagues, but also great friends. Also, Dr. Don Liebenberg, you have freely offered me your knowledge and wisdom and working with you the last couple of years has been a wonderful experience. I

consider you a close friend and mentor. I need to thank my undergrads, Jared Williams and Spencer Waldrop. Though it didn't always seem like we were working, our collaboration was one of the most constructive I have had and for that I am grateful. I hope you were able to learn as much from me as I learned from both of you. Also, Dr. Chad Sosolik, you have been a wonderful mentor and teaching junior lab with you for three years taught me an enormous amount.

During the last five years, I have had too many collaborators to list here, so instead I will (remove "directly") mention only those who have contributed directly to this work: Dr. Joe Brill and his students at the University of Kentucky for DSC data; Dr. Daniel Thompson for specific heat measurements; Dr. TJ Zhu at Zhejiang University for getting me started on this material; Dr. Xing Gao at the Institute of Modern Physics for phonon dispersion calculations; and finally Dr. Shiou-Jhu Hwu, Dr. Colin McMillen, and Dino Sulemanovic for single crystal x-ray data and refinement. To the rest of you, thank you very much, you have all taught me valuable lessons.

Finally, I need to thank my family, especially my parents: Mom and Dad, you have given me so many wonderful opportunities that have allowed me to get to this point in my life; Elliot, (you have at times provided me much needed comedic relief? not sure how to thank Elliot.), and finally Kayla, my beautiful bride, you have made my life so much easier these last five years. Thank you.

TABLE OF CONTENTS

Page

Table of Contents (Continued)

LIST OF TABLES

LIST OF FIGURES

List of Figures (Continued)

Figure Page

List of Figures (Continued)

Figure Page

CHAPTER ONE

INTRODUCTION

1.1 Thermoelectricity and Thermoelectric Materials

The looming fossil fuel shortage coupled with the environmental concerns of burning fossil fuels and our ever-increasing demand for energy impose a pressing need for alternative and sustainable energy conversion technologies.[1] To this end thermoelectricity is the simplest technology applicable to direct heat-to-electricity energy conversion, fitting well into the Department of Energy's renewable energy initiative and the Department of Defense's Sustainability initiative. Though it would be naive to expect thermoelectric materials to be the primary solution to large scale energy production, in certain (*niche*) applications thermoelectric materials are very promising, a fact that was realized as early as the 1950s by Ioffe.[2]

Rather than an exhaustive introduction to thermoelectricity and thermoelectric materials (for an in-depth introduction to thermoelectricity the reader is referred to references [3] and [4]), I will limit my discussion of thermoelectric materials to three specific aspects that I find to be most useful and somewhat less heeded. First I will discuss the thermoelectric effect in the context of Onsager relations because I find the elegance of this simple description of the fundamental phenomenon to be unparalleled. Second I will discuss the basic principles of the Seebeck effect for two reasons: most

obviously because the Seebeck effect is the basis, at least historically, of all of the thermoelectric effects, and second because in my opinion most basic descriptions of the Seebeck effect are at best difficult to understand and in some cases misleading. Finally I will discuss the heat engine analogy of thermoelectric devices because I think this route offers the most insight for the future of the field of thermoelectric materials.

1.1.1 Onsager Relations

As suggested by their name, thermoelectric effects deal with the interplay of two flows; namely charge and heat (or entropy). This relation was pointed out by Lord Kelvin as early as 1854 in the form of the Thompson relations:

$$\mathrm{K} \equiv \frac{d\Pi}{dT} - \alpha, \Pi = T\alpha \tag{0.1}$$

here K is the Thompson coefficient, Π is the Peltier coefficient, and α is the Seebeck coefficient.[5] A much more through and general description of the relation between the charge and entropy flows was given by Onsager in 1931.[6] In his derivation Onsager noted that when two or more processes occur simultaneously in any thermodynamic system there will be an interaction between them. In the simplest case a thermodynamic system under the influence of two processes can be described by the following equation (in this case the driving forces are the electrical field andtemperature gradient)

$$\begin{pmatrix} J_e \\ Q \end{pmatrix} = \begin{pmatrix} L_{11} & L_{12} \\ L_{21} & L_{22} \end{pmatrix} \begin{pmatrix} \nabla V \\ -\nabla T \end{pmatrix} \tag{0.2}$$

Obviously the diagonal terms correspond to the thermal and electrical conductivities ($L_{11} = \sigma$ and $L_{22} = \kappa$) while the cross terms L_{12} and L_{21}, which correspond to interactions between the fluxes describe coupled thermo-electric effects. Using the principle of

microscopic reversibility Onsager further showed that $L_{12}=L_{21}$ though in the current form L_{12} and L_{21} do not correspond to physically meaningful quantities. Later H.B. Callen showed that with proper selection of the driving forces it is possible to obtain a more meaningful description of the system where the off-diagonal elements correspond to physically measurable quantities.[7]

To begin Callen's description we will first consider the total energy flux in the system which can be given by the expression

$$\overrightarrow{J_E} = \overrightarrow{J_Q} + \mu_e \overrightarrow{J_N} \tag{0.3}$$

where $\overrightarrow{J_E}$ is the energy flux, $\overrightarrow{J_Q}$ is the heat flux, μ_e is the electrochemical potential, and $\overrightarrow{J_N}$ is the particle flux. Now if we remember that these fluxes are conjugated to their thermodynamic potential gradients ($1/T$ and μ_e/T respectively) it is possible to write the forces in the system as:

$$\overrightarrow{F_N} = \vec{\nabla}\left(\frac{-\mu_e}{T}\right) \tag{0.4}$$

and

$$\overrightarrow{F_E} = \vec{\nabla}\left(\frac{1}{T}\right) \tag{0.5}$$

Using these forces we can rewrite the equation describing the entire system as

$$\begin{pmatrix} \overrightarrow{J_N} \\ \overrightarrow{J_E} \end{pmatrix} = \begin{pmatrix} L_{NN} & L_{NE} \\ L_{EN} & L_{EE} \end{pmatrix} \begin{pmatrix} \vec{\nabla}\left(-\mu_e/T\right) \\ \vec{\nabla}\left(1/T\right) \end{pmatrix} \tag{0.6}$$

At this point for simplicity and in order to follow Callen's formulation it is useful to replace the energy flux with the heat flux. Additionally, we should remember that

according to Onsager the cross terms should be equal, which leaves us with Callen's formula:

$$\begin{pmatrix} \overrightarrow{J_N} \\ \overrightarrow{J_Q} \end{pmatrix} = \begin{pmatrix} L_{11} & L_{12} \\ L_{21} & L_{22} \end{pmatrix} \begin{pmatrix} -\frac{1}{T}\vec{\nabla}(\mu_e) \\ \vec{\nabla}\left(1/T\right) \end{pmatrix} \tag{0.7}$$

From here it is possible to quickly write down the equations for the thermal and electrical conductivity which correspond to the cases when $\overrightarrow{J_N}$ and $\overrightarrow{J_Q}$ equal zero respectively:

$$\kappa = \frac{D}{T^2 L_{11}} \tag{0.8}$$

and

$$\sigma = e^2 L_{11} / T \tag{0.9}$$

where following Callen's formalism *D* is defined by the relation $D \equiv L_{11}L_{22} - L_{12}^2$.

To describe the Seebeck coefficient we must first recall that it is defined as the ration between the electrochemical gradient and the temperature gradient and therefore given by the relation:

$$\alpha \equiv -\frac{1}{e}\frac{\vec{\nabla}(\mu_e)}{\vec{\nabla}(T)} \rightarrow \alpha = \frac{1}{eT}\frac{L_{12}}{L_{11}} \tag{0.10}$$

the Peltier coefficient on the other hand relates the particle current and the heat current and can therefore be given by the relation:

$$\Pi \equiv \frac{\overrightarrow{J_Q}}{\vec{J}} \rightarrow \Pi = \frac{1}{e}\frac{L_{12}}{L_{11}} \tag{0.11}$$

where $\vec{J}$ is the current density $\left(\vec{J} = \frac{1}{e}\overrightarrow{J_N}\right)$. This returns us to the Thompson relation between the Seebeck and Peltier coefficients given in **Equation (1.1)**.

At this point it is possible to solve the system of equations to obtain all of the kinetic coefficients and rewrite **Equation (1.7)** in terms of measureable quantities.

$$\begin{pmatrix} \overrightarrow{J_N} \\ \overrightarrow{J_Q} \end{pmatrix} = \begin{pmatrix} \left(T/e^2\right)\sigma_T & \left(T^2/e\right)\sigma_T\alpha \\ \left(T^2/e\right)\sigma_T\alpha & T^3\sigma_T\alpha^2 + T^2\kappa_J \end{pmatrix} \begin{pmatrix} -\frac{1}{T}\vec{\nabla}\left(\mu_e\right) \\ \vec{\nabla}\left(1/T\right) \end{pmatrix} \tag{0.12}$$

The final task is to estimate the amount of entropy carried by the charge carriers. To do this the first step is to write out the entropy flux density:

$$\overrightarrow{J_S} = \frac{\overrightarrow{J_Q}}{T} = \frac{1}{T}\left[L_{21}\left(-\frac{1}{T}\vec{\nabla}\left(\mu_e\right)\right) + L_{22}\left(\frac{1}{T}\right)\right] \tag{0.13}$$

With the help of the expression of Ohm's law in the current formalism

$$\vec{\nabla}\left(\mu_e\right) = -\vec{J}\frac{T}{eL_{11}} \tag{0.14}$$

equation (1.12) can be simplified to

$$\vec{J}_S = \frac{L_{21}}{TeL_{11}}\vec{J} + \frac{1}{T}L_{22}\nabla\frac{1}{T} \tag{0.15}$$

This simple expression for the entropy of the system has two distinct terms. The second term describes the entropy associated with the electrochemical potential while closer inspection of the first term reveals that it is the fraction of the entropy carried by each carrier and closely related to the Seebeck coefficient.

1.1.2 Seebeck Effect

The previous discussion gave an adequate theoretical description of the nature of the Seebeck coefficient, however, in practice a more phenomenological description is useful. The following section offers a phenomenological description of the Seebeck coefficient and its different interpretations.

The Seebeck effect was discovered by Thomas Joahnn Seebeck, a German doctor turned physicist, in 1821. In most cases the Seebeck effect and hence the Seebeck coefficient or thermopower are described in the context of the "thermocouple effect". In my opinion, however, this is somewhat misleading and doesn't lead to a proper understanding of the underlying physics. Perhaps this can be attributed to Seebeck's own misinterpretation of the phenomena named after him. In his experiment Seebeck noticed that a compass magnet placed near a junction between two dissimilar metals would be deflected when legs of the junction are held at different temperatures.[8] Seebeck erroneously attributed this observation to magnetism induced by the temperature gradient. Modern knowledge of the Seebeck effect tells us that the compass magnet is actually deflected by a magnetic field induced by a current flowing through the junction. Thanks to Hans Oersted's 1819 discovery of the magnetic field encircling an electric current, the background was in place for Seebeck to properly describe the phenomenon. However, the burgeoning nature of the physical understanding of the coupling between charge currents and magnetism meant that though Oersted's work was published it wasn't widely understood. Indeed the discovery of Faraday's law (changing magnetic field induced current) wasn't until 1831, and Maxwell didn't publish his classic equations unifying electricity and magnetism until 1861.[9]

A much more informative interpretation of the Seebeck effect can be achieved by considering a free electron gas, in the presence of a temperature gradient (**Figure 1.1**). In this way the electrons at the hot side of the material have a higher energy and therefore a higher velocity than the electrons near the cold end of the material, which leads to a net

migration (diffusion) of electrons from the hot end to the cold end. This in turn creates an excess charge on the cold end and therefore an internal electric field and a potential. The system will eventually come into equilibrium when the number of electrons diffusing from the cold side to the hot side equals the number of electrons diffusing in the opposite direction. Specifically, this will occur when the chemical potential, which is the driving force of the diffusion, is counter balanced by the internal electrical field. In actuality this process occurs almost instantly, and can be attributed to two factors: first of which is the fact that electrons move very quickly. The second reason behind the rapid equilibrium is less intuitive, but much more informative: in reality when the potential gradient is generated in the Seebeck effect it does not involve electrons moving all the way from the hot end to the cold end (as may be assumed when looking at the cartoon) but rather a slight distortion of the overall electron distribution. In this way, small perturbations of the electron positions (in the same direction) lead to an overall distortion of the electron density. This phenomena is well described (quantified) by the following equation

$$\nabla V = -\alpha \nabla T \tag{0.16}$$

where the coefficient α is the Seebeck coefficient or thermopower of the material in question. Importantly the above expression for the Seebeck coefficient defines a rank 2 tensor which can in most cases be replaced by its scalar counterpart (the average Seebeck) to obtain the following more common definition

$$\alpha = -\frac{\Delta V}{\Delta T} \tag{0.17}$$

In most cases it is sufficient to consider this scalar representation of Seebeck coefficient, however, there are exceptions to the rule, which like all direction dependent material properties can be exploited for certain technological uses. This preceding picture is obviously oversimplified and offers little information on the *magnitude* of the Seebeck coefficient, but importantly gives a simple phenomenological understanding of the problem at hand.

In a brilliant but somehow less heeded paper Paul Chaikin demonstrates a concise method to estimate the magnitude of the Seebeck coefficient.[10] The first step in this description involves defining the Peltier effect, which is in some sense the "inverse" of the Seebeck effect. Again we consider a free electron gas of charged particles in a box, but this time rather than a temperature gradient the perturbation to the system is an electric current. Since the charge carriers also carry some amount of heat there will be a heat current accompanying the charge current that can be described by the following equations.

$$\vec{j} = ne\vec{v}, \vec{u} = c\vec{v}, \Pi = \frac{cT}{q} \tag{0.18}$$

The Peltier heat is then defined by the equation

$$\vec{u} = \Pi\vec{j} \tag{0.19}$$

and is nothing more than the ratio of the heat current to the electrical current. As discussed in the previous section, the Seebeck coefficient and Peltier coefficient are connected by the combined thermal and electrical transport Onsager relation.

$$S = \frac{\Pi}{T} = \frac{c}{q} \tag{0.20}$$

This simple equation states one of the most informative definitions of the Seebeck coefficient. ***The Seebeck coefficient is proportional to the heat per charge carrier*** (in the case of thermal equilibrium, the proportional factor is in fact unity) or in a more general sense the entropy per charge carrier. This simple observation has proved to be not only very useful in basic understanding of the phenomena but also in the search for new avenues to high performance thermoelectricity. Indeed current research is focused on using new types of entropy to enhance Seebeck.[11]

Though beautiful in its simplicity the *particle-like* treatment of charge carriers in the preceding discussion is oversimplified. A more complete discussion of the Seebeck effect can be formulated in the matter-wave picture. In this case, it is more intuitive to deal with states rather than fundamental particles. In this picture the application of a temperature gradient across a material leads to an instantaneous redistribution of the matter waves, or in another sense changes in the system's wave function and thus its energy eigenvalues.

Furthermore, there is a major contribution to Seebeck from scattering, which is completely missed when we begin by assuming a free electron gas. In this vein, using Mott's formula is more appropriate, for example, in a quasi-equilibrium and diffusive electron transport process, one may relate the energy-specific (differential) electrical conductivity $\sigma(E)$ and the thermopower α in the differential form of the Mott relation upon a few simplifying assumptions,[12]

$$\sigma(E) = n(E)e\mu(E) = n(E)e^2 \frac{\tau(E)}{m^*} \tag{0.21}$$

where the energy-specific carrier concentration *n(E)* is defined as the number of carriers between energy *E and E+ΔE*, $\mu(E)$ and $\tau(E)$ their energy-specific mobility and relaxation time, and m^* the effective mass.

$$\alpha = \frac{k_B}{q} \int_0^\infty \sigma(E) \left(\frac{E - E_F}{k_B T} \right) \left(\frac{\nabla f_0(E)}{\nabla E} \right) dE \Big/ \int_0^\infty \sigma(E) \left(-\frac{\nabla f_0(E)}{\nabla E} \right) dE \tag{0.22}$$

where q is the elementary charge, k_B the Boltzmann constant, E_F the Fermi energy, and $f_0(E)$ the Fermi-Dirac distribution function. The "Fermi window factor" $\left(\frac{\nabla f_0(E)}{\nabla E} \right)$ is usually a bell curve centered at $E = E_F$ and having a narrow width on the order of $k_B T$. Therefore α is, *to the first order*, proportional to $\langle E\text{-}E_F \rangle$. Furthermore, in a degenerate single-band electron system one can rewrite **Equation (1.22)** as:[13]

$$\alpha = \frac{\pi^2}{3} \frac{k_B}{q} (k_B T) \left[\frac{g(E)}{n(E)} + \frac{1}{\mu(E)} \frac{d\mu(E)}{dE} \right] \tag{0.23}$$

where *g(E)* is the electron density of states. It is instructive to note that the two terms in the square bracket of **Equation (1.23)** each corresponds to a mechanism that affects α.

1.1.3 Heat Engine Analogy

Keeping with the formalism of the interaction between two flows (entropy/heat and charge) an excellent and overlooked paper by C.B. Vining shows the correlation

between thermoelectric materials and more traditional gas-cycle engines.[14] In this way the charge carriers in a thermoelectric material can be considered to be analogous to the working fluid in a mechanical engine. Vining begins by noting that the ration between the thermal and electrical conductivities under zero temperature gradient and under adiabatic conditions (zero heat flux) can be directly described by the equation

$$\begin{pmatrix} \vec{i} \\ \vec{s} \end{pmatrix} = \begin{pmatrix} \sigma_T & \sigma_T \alpha \\ \sigma_T \alpha & \lambda_e / T \end{pmatrix} \begin{pmatrix} \vec{E} \\ -\nabla \vec{T} \end{pmatrix} \tag{0.24}$$

where i is the electric current density, E is the electric field, q is the heat current density, s is the entropy current, ∇T is the temperature gradient, σ_T is the electrical conductivity and α is the Seebeck coefficient. λ_E is the thermal conductivity measured under the condition of zero electric field. Hence

$$\gamma_{Ei} \equiv \lambda_E \Big/ \lambda_i = \sigma_T \Big/ \sigma_q = 1 + \sigma_T \alpha^2 T \Big/ \lambda_i = 1 + ZT \tag{0.25}$$

where λ_i is the thermal conductivity under zero current and σ_q is the electrical conductivity under adiabatic conditions. Furthermore Vining pointed out that these ratios play the same role when considering the efficiency of a thermoelectric process as the ratio of C_p/C_v in a traditional gas-cycle. Importantly this suggests that near instabilities the efficiency of a thermoelectric device may be enhanced similar to the enhanced efficiency of a gas-cycle near a critical point in the working fluid. This idea is clearly illustrated in **Figure 1.2** where γ_{PV} of Freon-12 is plotted along with γ_{Ei} for several common n-type thermoelectric materials.[15]

This somewhat unusual approach to describing thermoelectric materials suggests three different routes for improving the efficiency of thermoelectric devices in line with the optimization of gas-cycle engines:

1. *Materials will exhibit an anomalously large γ_{Ei} and therefore ZT near electronic phase transitions similar to the increase in γ_{PV} and efficiency of gas cycles near a gas-liquid critical point.*
2. *The use of materials with strong interactions between charge carriers will cause the transport matrix L to be dominated by solely transport effects.*
3. *Attempt to use a more favorable thermodynamic cycle in a thermoelectric device.*

For the purposes of this thesis **rule number 1 is the most important**. It suggests that ***inherently unstable electron systems*** could display promising thermoelectric properties.

1.2 Mixed Conductor Thermoelectricity

Mixed conductors are materials in which charge and heat are transported by not only electrons or holes and phonons but also mobile ions. In the context of the Onsager relations discussed earlier in this chapter, mixed conduction can be easily included in thermoelectric research by increasing the rank of **Equation (1.6)** to include the flow of ions. A similar expansion of the Onsager relation has been done to accommodate the flow of spin in a material and is reported in reference [16]. The limiting case that the thermoelectric properties of a mixed conductor are dominated soley by the flow of ions and not electrons or holes is an example of the solid state Soret-Ludwig effect.[17]

A special class of mixed conductors is the so called superionic mixed conductors, which as their name suggests, display unusually large ionic conductivities. Until recently this class of materials has been somewhat ignored by the thermoelectric researchers because the coexistence of superionic conduction and good thermoelectric performance in the same material and in the same temperature range is very rare, which can be attributed to the fact that the compositional and structural requirements for these two phenomena are distinct. A large anionic electro-negativity is favored for ionic conduction, while a large electronegativity difference between the constituent elements will lead to more ionic bonding, strong scattering of charge carriers and thus low thermoelectric figure of merit, *ZT*.

Considering the Seebeck coefficient of this class of materials in the context of the entropy per carrier formalism offers an interesting question: Can the increased entropy carried by relatively massive mobile ions lead to an enhancement in Seebeck coefficient? Furthermore, mobile ions have internal degrees of freedom that at least theoretically could offer another route for increasing their entropy. Experimental realization of this theory has been realized in a small number of materials, but a complete understanding of the results is still lacking. An important observation of the existing research is that for the onset of ionic conduction to enhance thermoelectric performance, the charge of the mobile ions should have the same sign as the dominant charge carriers (i.e. in a material where hole conduction dominates the mobile ions should have a net positive charge).

Recent experiments, however, have shown ionic conductors to be promising thermoelectrics for another reason: mixed conductors tend to display very low values of

lattice thermal conductivity. This low thermal conductivity can be attributed to two factors. First, mixed conductors undergo a premelting transition where part of the crystal lattice begins to behave like a liquid (this is generally the onset of ionic conduction). This transition not only allows for more "dynamic" scatterers in the lattice, but also fundamentally changes the way heat is stored and transported in the material by eliminating transverse phonon modes in a part of the lattice.[18] Beyond their liquid like properties a general characteristic of mixed conductors is strong anharmonicity in the crystal lattice. Though it has been known for some time that anharmonicity in the lattice of certain materials leads to low thermal conductivity, the mechanisms governing this observation are not well understood. In this vein, we argue that the anharmonicity plays an equivalent role, at least thermally, in *the time domain* to the role of amorphicity in *the spatial domain*, therefore the thermal conductivity of strongly anharmonic materials is similar to amorphous materials.

1.3 Silver Germanium Telluride (Ag_8GeTe_6)

Ag_8GeTe_6 is an example of a material in which superionic conduction and good thermoelectric performance coexist.[19,20,21] Furthermore, Ag_8GeTe_6 undergoes four first order phase transitions between 155K and 250K, an extraordinary number for such a narrow temperature range, as well as having a molar heat capacity ~30 J/mol-K above the classical Dulong Petit limit suggesting that it is an inherently unstable system. The thermal conductivity of Ag_8GeTe_6 is also unusually low (~0.3W/m*K at room

temperature), which prompted it to be mentioned as a possible high performance thermoelectric material in the CRC Thermoelectrics handbook.[22] For these reasons Ag_8GeTe_6 offers a chance to not only study the enhancement of thermoelectric performance in unstable electron systems as suggested by C.B. Vining but also the thermoelectric properties, especially reduced lattice thermal conductivity, of mixed conductors.

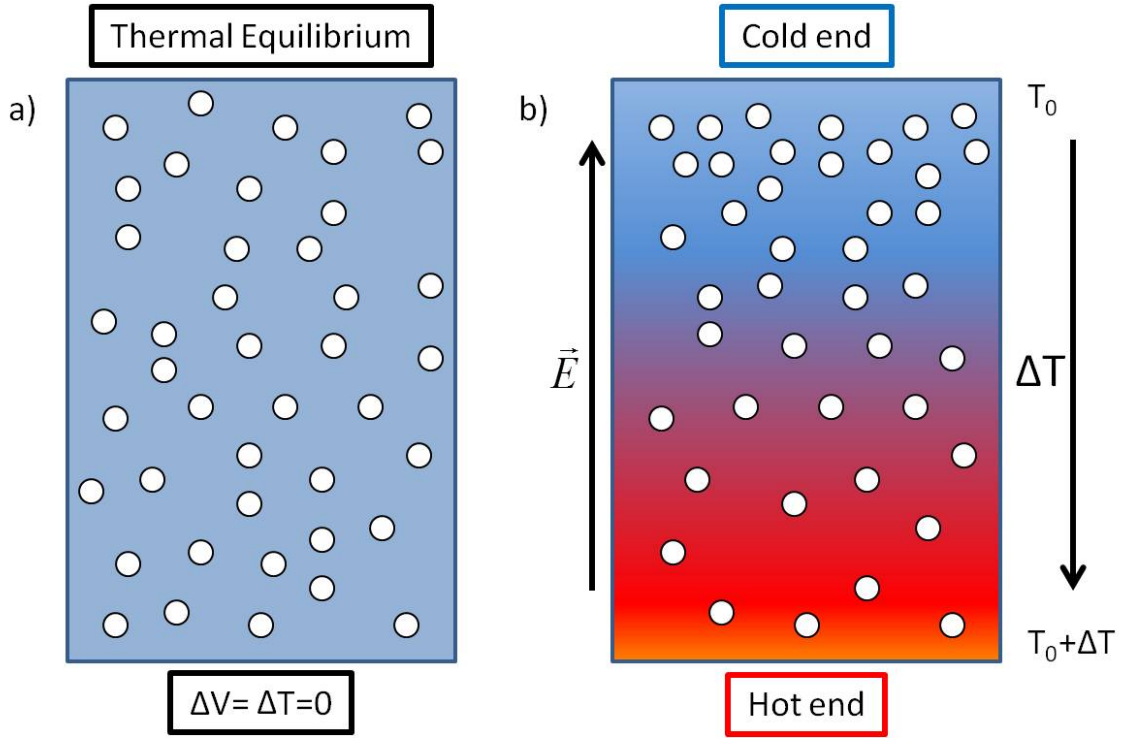

Figure 1.1: a) Charge carrier distribution in a material in equilibrium. b) The charge carrier distribution of a material under a temperature gradient, where the net diffusion of charge carriers from the hot side to the cold side is balanced by an internal electric field.

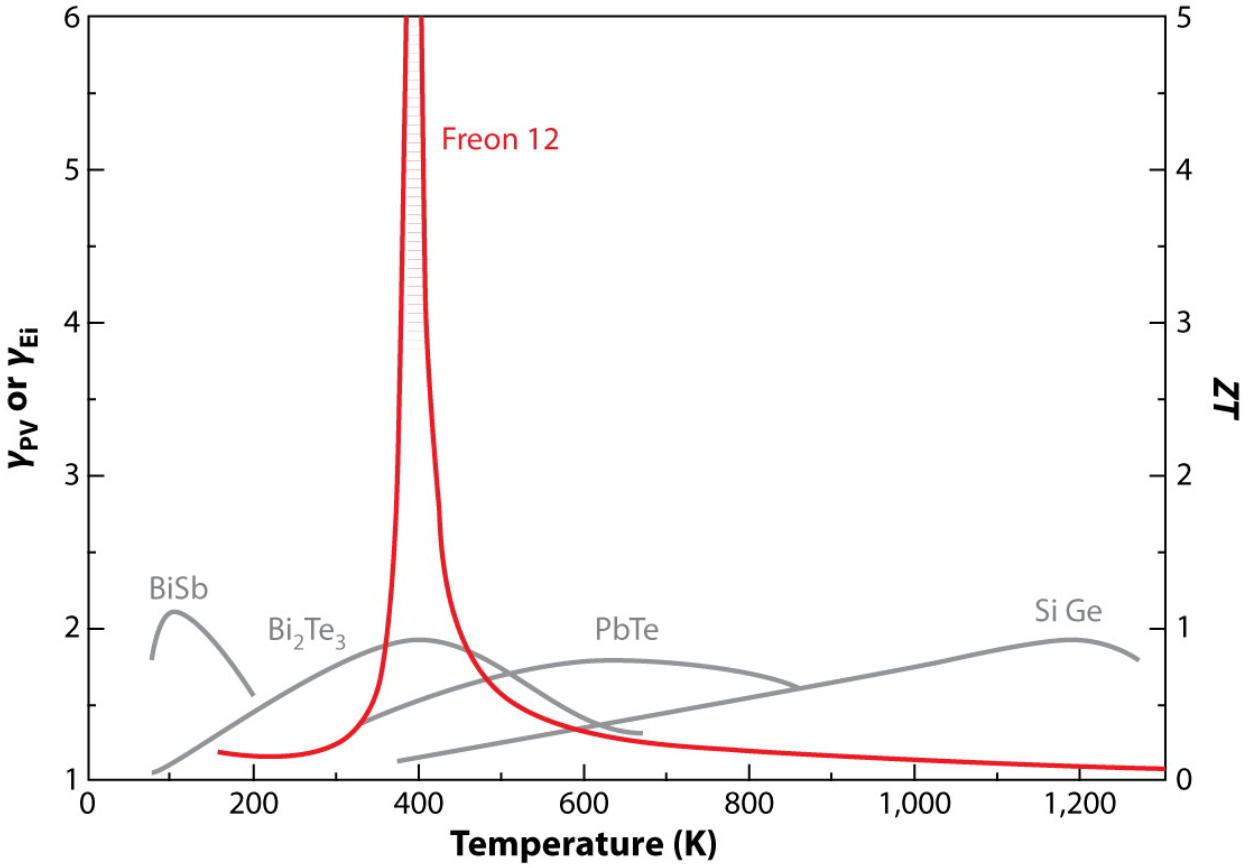

Figure 1.2: $\gamma_{PV}=C_P/C_V$ the ratio of the specific heat at constant pressure (C_P) to the specific heat at constant volume (C_V) for Freon 12 plotted along with $\gamma_{Ei}=\kappa_E/\kappa_i=1+ZT$ for several well known n-type thermoelectric materials as a function of temperature. *Source Ref. [15]*.

CHAPTER TWO

SYNTHESIS

The first and largest hurdle in beginning our study on Ag_8GeTe_6 was the synthesis of high quality samples for transport measurements. To that end, our distinction of a high quality sample is two-fold: (*i*) the sample is large and mechanically strong so it can be appropriately shaped and survive various transport measurements including many heating/cooling cycles; and (*ii*) the sample is phase pure so the results of transport measurements are intrinsic. While criterion (*i*) is specific to this study as Ag_8GeTe_6 is known for its brittleness, criterion (*ii*) is generic but has been somewhat disregarded in previous studies on Ag_8GeTe_6. It took more than one year to address these criteria and not only find a suitable method to grow large, mechanically strong, amply pure samples but also to evaluate the transport data.

The lesson of this struggle is that quality control of samples is of utmost importance in such an exploratory study as the researchers must know from the outset what they are actually measuring. Furthermore, the necessity of conducting transport measurements lies in the fact that theoretical band structure calculations on Ag_8GeTe_6 are still unavailable due to the complicated crystal structure and intriguing consecutive phase transitions.

Previous studies have shown that not only is it difficult to pelletize Ag_8GeTe_6 powder by hot pressing or spark plasma sintering, but also that slight variations in composition can have drastic effects on the transport properties.[19,20,23,24,25,] The second

observation is a reminiscent of a strongly correlated electron system, a category that Ag_8GeTe_6 hardly fits in. Previous authors neither explained the correlation, if any, between these two observations nor elucidated their cause(s). In this thesis these two observations will be satisfactorily explained.

Two previous x-ray diffraction studies and a DSC study were taken on single crystals of Ag_8GeTe_6, though the remainder of the published work, including all examples of transport measurements on Ag_8GeTe_6 were performed on powders densified using a hot press (HP),[21,23,23,24,26,27] To obtain single phased Ag_8GeTe_6, all of these studies began with a melt growth from either high purity single elements or stoichiometric amounts of Ag_2Te, GeTe, and elemental Te. In the present study, we have adopted the single-element recipe. It should again be stressed that Ag_8GeTe_6 is brittle and hard pelletize from powder, and furthermore, the way in which a few percent porosity and the residual stress impact the transport properties of a hot pressed sample is an open question. As such, extra caution should be taken when referencing and comparing the published data.

A quick look at the phase diagram of Ag, Ge, and Te (**Figure 2.1**) confirms that Ag_8GeTe_6 is the *only* ternary phase present which leads us to believe that it should be *straightforward* to form.[28] Our results however, have shown that though it is indeed easy to obtain Ag_8GeTe_6 as a primary phase obtaining samples with high phase purity > 99% is very difficult. We attribute this difficulty to the ***incongruent melting at 645°C*** (**Figure 2.2**). Incongruent melting refers to the phenomenon in which a crystalline phase melts into a solid-liquid mixture where the solid phase and liquid phases have *different*

compositions. Crystal growth from a stoichiometric ratio of starting materials will *inevitably* lead to the formation of secondary phases, as will be discussed in the following chapters [**Chapter 3, 4**]. Additionally, the fact that small amounts of secondary phases in Ag_8GeTe_6 samples can have drastic effects on their properties suggests that Ag_8GeTe_6 is an intrinsically low-carrier-concentration electron system. As such, a crystalline solid *cannot* be obtained by slowly cooling a stoichiometric melt.

When growing crystals from incongruent melting substances, the floating zone method is often used. Indeed we have an optical floating zone furnace in position, however, the volatility of Te at elevated temperatures restricts the use of the optical furnace. Another way of growing crystals from incongruent melting substances is flux growth, which will be briefly addressed in the following sections.

In the following sections we will discuss our attempts to synthesize bulk Ag_8GeTe_6 samples through single element spark plasma sintering, melt growth, hot pressing (HP), vapor transport, and flux growth techniques. Initial characterization of the samples grown using all of the aforementioned techniques was done using our in-house tabletop x-ray apparatus (Rigaku Miniflex).

2.1 Single Crystal Growth

Ideally, single crystals would be used when studying the transport properties because they allow for a better understanding of the intrinsic properties of the material. In most cases, however, limitations on the size and shape of single crystals that can be

grown make this impossible. In the cases of Ag_8GeTe_6, we were unable to grow large enough single crystals to perform transport measurements, but some of our growths did yield small single crystals suitable for x-ray diffraction studies which proved very valuable in our studies of the low temperature crystal structure of Ag_8GeTe_6. In the following section we will discuss the techniques used (some successful and some less successful) to obtain single crystals of Ag_8GeTe_6.

2.1.1 Vapor Transport

For our first attempts to grow single crystals of Ag_8GeTe_6, we used a vapor transport method and followed a procedure similar to those laid out in [19] and [21]. To begin the growth, approximately 2g of Ag_8GeTe_6 powder, synthesized during one of our previous melt growths, was loaded into a 2" diameter quartz tube (~10" long) along with 0.1g of Iodine crystals. The tube was then evacuated to <20mTorr and sealed using a Hydrogen torch. At this point the tube was then loaded into a tube furnace (Lindberg Blue TF55035C-1), and care taken to make sure the charge (both Ag_8GeTe_6 and Iodine) was in the middle, the hottest zone, of the furnace. The length of the tube meant that the other end was near the outer end of the furnace which would create a temperature gradient across the length of the tube as the furnace was heated. Next, the furnace was quickly heated to 500°C and allowed to sit for 5 days. Care was taken when choosing the reaction temperature to avoid the incongruent melting of Ag_8GeTe_6 at 645°C. After soaking at 500°C for five days the furnace was turned off and allowed to cool to room temperature. When the tube was removed from the furnace it was clear that the sample

had reacted in some way. Where there was originally powder now contained a dense ingot covered in small crystallites. X-ray analysis of both the ingot and the crystallites showed that the sample had begun to decompose during the growth as both of the resulting components showed traces of Ag_5Te_3 and Ag_7Te_4 as well as the starting Ag_8GeTe_6 phase.

2.1.2 Flux Growth

Another attempt was made to grow single crystals of Ag_8GeTe_6 using a self flux method. For this growth, stoichiometric amounts of Ag and Ge were loaded into a quartz tube along with an excess of Te (approximately 10 times the stoichiometric amount). A piece of quartz wool was then added to the tube just above the surface of the powder. The tube was then evacuated and sealed using a hydrogen torch. The sealed tube was then loaded into a box furnace (Lindberg Blue model BF51732 with a UP150 temperature controller) and heated to 1000°C. This temperature was maintained for several days before removing the tube and placing it directly in a centrifuge. The excess flux was then spun off before it had a chance to solidify. Ideally this would have left single crystals of Ag_8GeTe_6 in the tube on top of the quartz wool. Unfortunately, this method did not yield any suitable single crystals and was therefore abandoned.

2.1.3 "Lucky" Growth

A breakthrough in our attempts to grow a single crystal came when we noticed the formation of a small cubic crystal on the free surface of one of our melt growths. Initially

we suspected this was a single crystal of Ag_8GeTe_6, however, the mechanisms behind its formation were unclear. Repetition of the type of melt growth that led to the single crystal led to the collection of a number of small crystals. Particularly interesting was the fact that one run yielded nearly 20 crystals while the others normally yielded one. We do not offer an explanation for the behavior, but found it interesting. Clearly a better understanding of the mechanisms governing the formation of single crystals on the free surface of Ag_8GeTe_6 melts would be very useful in further studies. Nonetheless the single crystals we were able to obtain were suitable for single crystal x-ray diffraction measurements, and which to be essential in our efforts to describe the low temperature crystal structure of Ag_8GeTe_6 **(Chapter 3 Section 1)**.

2.2 Polycrystalline Growth

In a perfect world when studying a new material it would always be possible to grow large high quality single crystals in order to pinpoint the intrinsic properties of the material. Obviously this is not the case, and what's more in many cases the effects of grain boundaries and such are technologically useful. In the case of Ag_8GeTe_6 we performed our studies on "coarse grained" polycrystalline samples because suitable single crystals could not be obtained. The classification of our polycrystalline samples as "coarse grained" is important because it distinguishes our work from that of previous authors. Our coarse grained samples, shaped directly from ingots, should display transport properties closer to the intrinsic behavior because they have fewer defects and

grain boundaries than the hand ground and hot pressed samples presented in [19], [20], and [25],.

2.2.1 Spark Plasma Sintering

In an early effort to grow/sinter Ag_8GeTe_6 we attempted to synthesize Ag_8GeTe_6 directly from single elemental powders (Ag powder Alfa Aesar 4-7 micron 99.99%, Ge powder Alfa Aesar -100 mesh 99.999%, and Te powder Alfa Aesar -30mesh 99.99%) using a Spark Plasma Sintering System (SPS), Dr. Sinter SPS-515S made by Fuji Electronic Industrial Co., similar to what we had done for SiGe.[29] The major benefit of this approach is that it offers a way to approach the desired phase from the "bottom" of the phase diagram rather than the "top" **(Figure 2.2)**. This is because the process is far from equilibrium and therefore allows for growth at temperatures lower than the bulk melting point so as to avoid the incongruent melting that plagued our attempts to grow Ag_8GeTe_6 using more traditional methods. Initially this technique appeared promising as x-ray analysis of the first few attempts showed the sintered products to be made up of a combination of the desired phase and unreacted elemental powders, as shown in **Figure 2.3**. After many attempts, however, it was clear that it would be impossible to obtain a complete reaction using on the SPS and I moved on to melt growth.

Furthermore, it should be mentioned that we attempted to densify phase pure Ag_8GeTe_6 powders using the SPS however that attempt also failed. SPS is a powerful technique that can densify most materials, however, from experience (we have

SPSed~400 samples per year for the last five years) our group has come up with two conspicuous exceptions:

1. Materials with high electronic density of states (e.g., LAST materials, we know from Dr. Drymiotis' samples)[30]
2. Materials with strong anharmonicity, such as many oxides and chalcogenides, because of the large thermal expansion coefficient and fast ramping rate in a typical SPS process.

In actuality the fact that Ag_8GeTe_6 could not be SPSed was our first hint that Ag_8GeTe_6 has strong anharmonicity, which is the key to many of its unusual properties and will be discussed in the following chapters.

2.2.2 Melt Growth

Based on many growths basically following a procedure of trial-and-error (each growth took somewhere between a few days and 3 weeks to complete) we came to the conclusion that melt growth is the most promising way to obtain the physically solid high purity samples that are required for transport measurements. In order to melt grow Ag_8GeTe_6 stoichiometric amounts of elemental Ag and Te powders and Ge pieces were massed out, mixed, and loaded into a ½" diameter quartz tube (Ag powder Alfa Aesar 4-7 micron 99.99%, Ge pieces Alfa Aesar 3-9mm, and Te powder Alfa Aesar -30mesh 99.99%). The tube was then evacuated and sealed using a hydrogen torch. At this point the sample was loaded into a box furnace (Lindberg Blue model BF51732 with a UP150 temperature controller) and heated using the temperature profile shown in **Figure 2.4** similar to that found in [25]. The resulting samples were analyzed using our tabletop x-

ray powder diffraction system and were found to be single phased, but far too brittle to be used for transport measurements. Further attempts to melt grow Ag_8GeTe_6 proved that though it is simple to get the proper phase using this technique obtaining a solid sample capable of being cut or shaped for further measurements is very difficult.

A breakthrough came when a sample was loaded into the furnace at an acute angle. The initial idea for this setup was that it would maximize the ratio of the free surface of the liquid to the surface in contact with the quartz tube. By varying the angle between the tube and the bottom of the furnace I was able to control this ratio and therefore gain some control over the mechanical properties of the resulting samples. The best angle for growth was found to be ~30^o. Finally though the samples were still too brittle to cut using a diamond or wire saw we were to shape bar and disc shaped samples for transport and laser flash measurements using a small file. This process was quite time consuming but proved to be the only way to shape Ag_8GeTe_6 samples that were strong enough to survive our measurements.

2.2.3 Hot Pressing (HP)

In an attempt to obtain mechanically strong samples we also tried to HP hand ground Ag_8GeTe_6 powders from our previous melt growths. From the onset we were cautions with our expectations as we knew from interactions with Dr. Zhu the author of [20] that the samples they were able to obtain were very brittle even after HP, and only sintered in a very narrow temperature range (+/- 20° C) around 400° C. Furthermore as mentioned above early reports on the thermoelectric properties of Ag_8GeTe_6 were very

inaccurate due to problems in attaining properly densified samples using HP. For our study we followed a procedure similar to [19] and [20]. We began with hand ground Ag_8GeTe_6 powders (~3.5g) synthesized during one of our previous melt growths and loaded them into ½" graphite HP dies. The samples were pressed using a force of 640Kg (Thermal Technology Inc. Model # HP20-4560-20). The temperature profile for the pressing included a quick ramp (~15min.) to the holding temperature of 420°C followed by a two hour hold at 420°C and finally furnace cooling to room temperature. The sample was cooled without pressure in order to lessen the chance of cracking during the cooling process. The sample obtained from this procedure was exceedingly brittle and therefore not suitable for further studies. Approximately 15 samples were hot pressed using different conditions, however, we were never able to obtain samples that displayed better mechanical stability that our file shaped ingots.

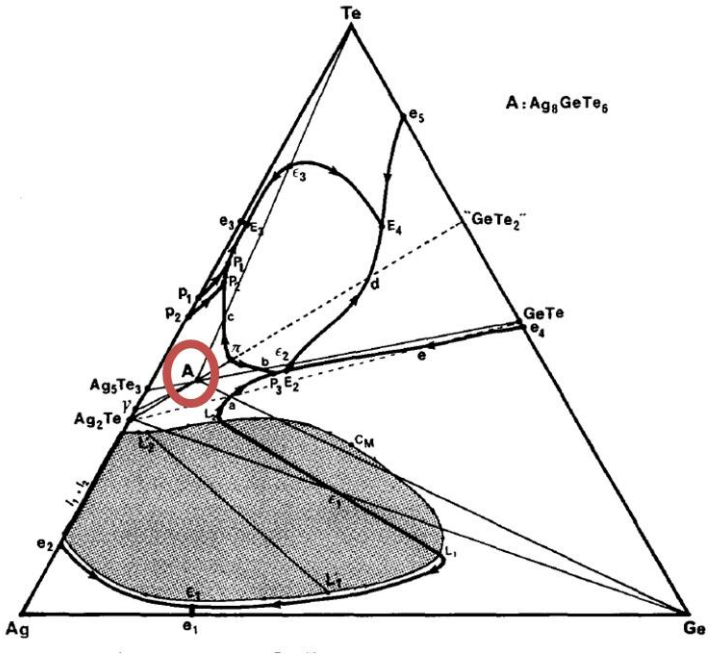

Figure: 2.1 Ternary Phase Diagram of Ag, Ge, and Te. *Source Ref [28]*.

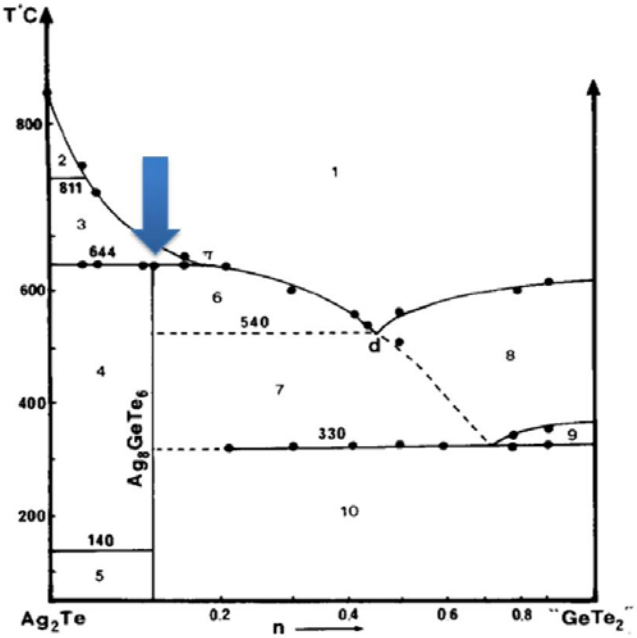

Figure: 2.2 Psuedo Binary Ternary Phase Diagram of Ag_2Te and $GeTe_2$ which shows the incongruent melting of Ag_8GeTe_6 at 644 C. *Source Ref [28]*.

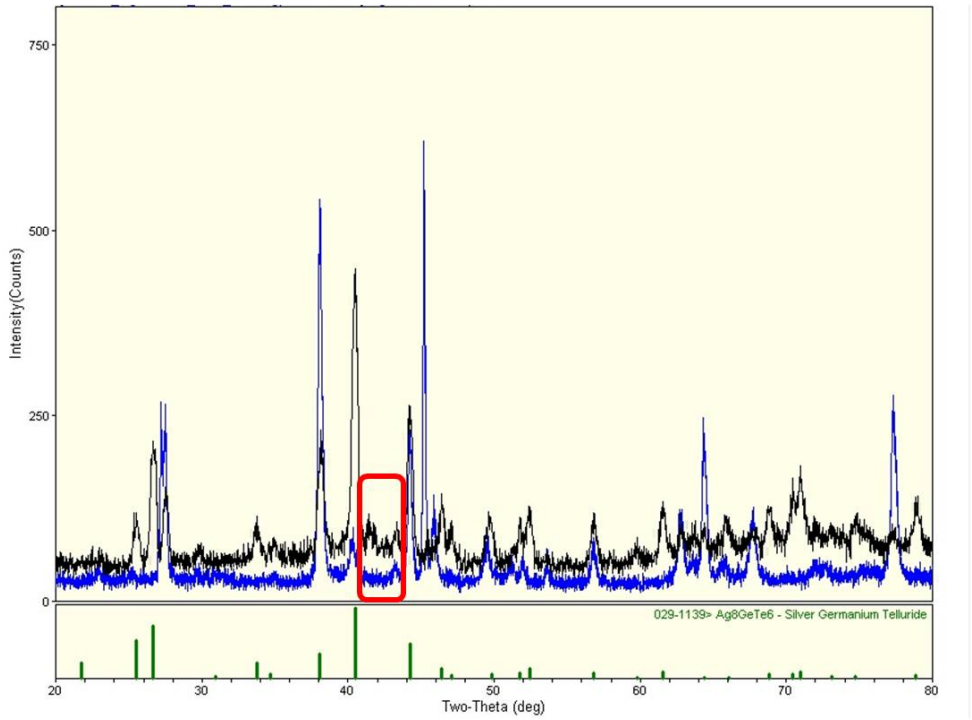

Figure 3: X-ray pattern of the post SPS Ag_8GeTe_6 samples shown in black the blue pattern is the starting material and green peaks are the known pattern for Ag_8GeTe_6. The presence of the strong peaks in the post SPS pattern around 28^o and 77^o are evidence of unreacted starting material. The peaks in the post SPS pattern between 41^o and 45^o (circled in red) most likely correspond to either Ag_2Te or Ag_5Te_3.

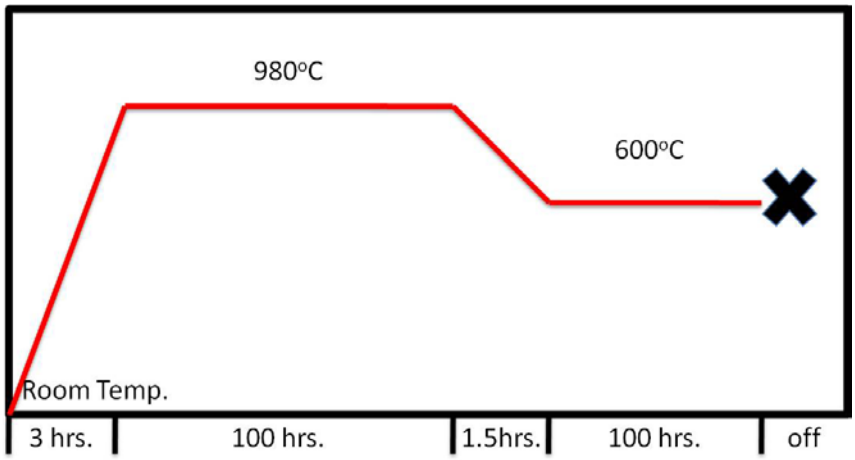

Figure 2.4: Temperature profile used in the melt growth of Ag_8GeTe_6.

CHAPTER THREE

STRUCTURE AND MAGNETIZATION

3.1 Crystal Structure

Many of the unusual material properties of Ag_8GeTe_6, especially the migration of silver ions at elevated temperatures, can be directly attributed to it unusually complicated crystal structure.[31] Perhaps unsurprisingly the room temperature crystal structure of Ag_8GeTe_6 was a topic of debate for some time with several conflicting reports published on the subject in the 1970s [26], [32], and [33]. Indeed the reports suggest similar symmetries, either cubic ($F\bar{4}3M$) or pseudocubic (R3), but offer slightly different interpretations of the structure. Specifically trouble describing the locations, occupancies, and displacement parameters of the Ag sites have led to discrepancies in the descriptions that become particularly evident when the Ag-Te and Ag-Ge bond distances are considered. In general these discrepancies have been attributed to the strong silver disorder related to the ionic conductivity. More recently F. Boucher *et al.* have offered a much more complete description of the crystal structure of Ag_8GeTe_6 at both room temperature and 400 K going as far as to map the Ag^+ diffusion path through the crystal.[21] The key to the refinement was the use of an ***anharmonic*** model to describe the locations of the Ag ions. Indeed Boucher *et al.* were able to accurately describe the structure of Ag_8GeTe_6 using a similar model to the previous studies with the inclusion of three distinct Ag sites with anharmonic ADPs. This treatment of the structure allowed for

a description of the Ag diffusion path through the crystal which is shown in **Figure 3.1c**. This structure, space group $F\bar{4}3M$ with $Z=4$, was confirmed by our single crystal x-ray results performed in the Department of Chemistry at Clemson University. A diagram of the structure is shown in **Figure 3.1b**.

Though the room temperature structure of Ag_8GeTe_6 is well understood the low temperature structure is still unknown with no published work discussing the subject. It is well known that the Argyrodite family of compounds undergoes multiple phase transitions below room temperature, which in many cases have been shown to be structural in nature.[34,35,36] Ag_8GeTe_6 undergoes at least four phase transitions between 0K and room temperature, and while it has been suggested by some authors that they are all first order others have suggested that they are related to Ag^+ ordering.[27,37] The heat capacity of Ag_8GeTe_6 measured by Kawaji and Atake is shown in **Figure 3.2,** and clearly shows the four phase transitions below room temperature at 156 K, 169 K, 223 K, and 245 K. In order to elucidate the nature of these phase transitions we performed powder x-ray diffraction measurements at 140K, 160K, 210K, 220 K, 230 K, 240 K, 260 K, and 295 K. The measurements were performed using the rapid access portal at Beamline 11-BM-B at the Advanced Photon Source (APS) at Argonne National Lab. It should also be noted that due to the high *Z* (atomic mass) of the constituent elements in Ag_8GeTe_6 our samples were diluted with amorphous silica in order to lower the absorption (the actual composition of the measured samples was Ag_8GeTe_6-$(SiO_2)_5$).

The x-ray diffraction pattern of Ag_8GeTe_6 taken at different temperatures is shown in **Figure 3.3**. From the data it is clear that Ag_8GeTe_6 undergoes at least one if not

more symmetry changes between 140 K and room temperature. Most likely the sample undergoes two symmetry changes that correspond to the onset of new peaks in the diffraction pattern. One symmetry change occurs between 240K and 250K while the second occurs between 210K and 220K. This suggests that the transition observed by Kawaji and Atake at 223K and 245K are indeed first order (structural) while the transitions at 156K and 170K are second order. The fact that the second transition (223K in DSC) is observed at a slightly lower temperature in x-ray than DSC can likely be attributed to uncertainty in the temperature measurements made during the x-ray experiment.

Refinement of the high temperature data using the published space group ($F\bar{4}3M$ at 295 K) confirmed that the samples were indeed Ag_8GeTe_6, but did offer one surprise. Though measurements performed on our in-house x-ray apparatus showed our powder samples to be single phased the higher resolution of the synchrotron data allowed us to detect a small amount (~1%) of secondary phase, most likely Ag_5Te_3. At this point it was still difficult to accurately refine the low temperature diffraction patterns because we did not have enough information about the space group. For this reason we measured single crystal x-ray diffraction at 190 K in the chemistry department at Clemson University. Unfortunately the data didn't show enough reflections to be refined so the crystals were sent to Rigaku Ltd. to be measured on a higher resolution instrument.

The single crystal x-ray diffraction pattern of Ag_8GeTe_6 was measured at Rigaku using an Xta LAB® P200 diffractometer with a 30W MicroMax003 Mo/Cu X-ray generator. Two studies were performed using MoKα radiation (λ=0.071075 Å): First a

temperature study between 293 K and 173 K was performed where 30 images of 0.5 deg. oscillation and 10 sec. exposure were measured at different temperatures: 25 °C, -10 °C, -20 °C, -30 °C, -40 °C, -50 °C, -60 °C, -70 °C, -80 °C, -100 °C (298 K, 263 K, 253 K, 243 K, 233 K, 223 K, 213 K, 203 K, 193 K, 173 K. From the change in the diffraction images, shown in **Figure 3.4**, it is clear that there are two structural transitions one occurring between -30°C and -40°C (243K and 233K) and the other occurring between -40°C and -50°C (233K and 223K). Furthermore the diffraction patterns did not indicate additional transitions between -50°C and -100°C (223K and 173K). It should also be noted that when the crystal was warmed back up to 293K the original diffraction pattern was again observed, indicating that the structural transitions are fully reversible, without compromising the crystal. The second study involved taking full data collections at both 293K and 173K in order to determine the detailed structure. The room temperature data unambiguously confirmed that structure from previous studies: face centered cubic, space group $F\bar{4}3M$, a = 11.56. As expected after the temperature dependent study the low temperature phase (173K) has many more diffraction spots, which initially appeared to correspond to a face-centered cubic structure with a = 23.05. Further refinement, however, showed this structure to be incorrect. The onset of these new diffraction spots however can be explained by a combination of two factors:

1) The low temperature structure is instead of lower symmetry - primitive cubic with a = 11.51 with the best results appearing to be in space group P2(1)3.

2) During the phase transition the crystal also experiences twinning, which, like the phase transition, is reversible and non-destructive. This twinning also produces an additional set of reflections, which gives the appearance of higher symmetry.

Interestingly, both of these structural features are observed in other members of the Argyrodite family including Ag_7PSe_6 and Cu_7PSe_6 where similar transitions occur (albeit at different temperatures).[34,35] Prior to that work, most reports suspected that the low temperature structure of Argyrodite compounds was an ordered supercell with a ~ 23.00 Å based on simple photographs and powder data,[21,27] though the idea of space group P2(1)3 with a ~ 11.50 Å was proposed by Gorochov.[38] With this in mind we refined the single crystal data using a primitive cubic unit cell (P2(1)3) with a = 11.51 Å coupled to a twin refinement to account for the extra reflections and were able to get a reasonable structure solution. Additionally the twins appear to be present in about a 1:1 ratio, explaining why the intensities of the additional diffraction reflections are so significant that they give the appearance of the (nearly exactly) doubled unit cell parameter of a = 23.05 Å.

With this in mind we attempted two refinement approaches on the single crystal Ag_8GeTe_6 data in order to identify the atomic positions: one based on the proposed structure by Gorochov and one based on the well-refined structure of Ag_7PSe_6 by Evain. Clearly, in the latter case we were able to identify another Ag atom in our data to bring the stoichiometry to Ag_8GeTe_6. Both approaches yielded a reasonable R-value of about 0.16. Unfortunately we were not able to obtain an unambiguous solution to the structure from our refinement.

In a final attempt to determine the low temperature structure of Ag_8GeTe_6 we attempted to refine the low temperature powder x-ray data from the APS using the space groups suggested by our single crystal results. We attempted two solutions both of which were used space group P2(1)3 and a lattice constant of 11.5206Å. Unfortunately neither of these refinements yielded a good solution to the crystal structure, both of the fits had an R-value of about 16%. The results of the refinements are shown in **Figure 3.5**.

3.2 Magnetization

The D.C. magnetization of Ag_8GeTe_6 was measured on a Quantum Design Physical Properties Measurement System (PPMS®) using a Vibrating Sample Magnetometer (VSM®) option. The magnetization was measured between 10K and 300K at fields between 100 Oe. and 10,000 Oe., additionally a measurement at 5,000 Oe. was taken between 10K and 350K to verify that the observed behavior continues above room temperature. The field dependence of the magnetization was also measured at several temperatures. As can be seen in **Figure 3.6** all of the measurements showed Ag_8GeTe_6 to be diamagnetic with a slight positive temperature dependence except for the 100 Oe. measurement that is too close to the lower limit of the resolution of the instrument to resolve a trustable value.

3.2.1 Magnetic Units

Before continuing with my analysis of the magnetization data it is very useful to discuss the units used in magnetization measurements, because in many cases keeping track of the units is the most difficult part of understanding any magnetic data. In general this confusion arises from the fact that most data is reported in emu's though most analysis is performed using Gaussian or S.I. units. Additionally many scientists use Tesla as a unit of applied field ($\vec{H}$) though in the strictest sense Tesla is a unit of the magnetic field ($\vec{B}$), where depending on the system of units $\vec{B} = \mu_0(\vec{H} + \vec{M})$ (S.I.) or $\vec{B} = \vec{H} + 4\pi\vec{M}$ (Gaussian or cgs).[39] Beyond the improper use of the units of Tesla the biggest hurdle to an inexperienced scientist interpreting magnetic data is the fact that emu is a system of units and not a unit of magnetization. In most cases magnetization data is presented in the units of *emu/g* or *emu/mol* which is easy enough to understand until a conversion to S.I. units in needed. This conversion is the main sticking point when inexperienced scientists try to interpret magnetic data, because it is not always clear as to which conversion factor to use. In this sense it is critical to completely unify the system of units before beginning to analyze any magnetic data. A convenient table that outlines these considerations is given in **Figure 3.7**.

3.2.2 Measurements

The measurement was performed using a Vibrating Sample Magnetometer (VSM®) option on a Quantum Design PPMS®, which is notable because this type of measurement is normally performed using a Superconducting Quantum Interference

Device (SQUID®). In general SQUID measurements are much more precise (several orders of magnitude) than VSM measurements, though the equipment need for a SQUID measurement is much more expensive than the relatively simple VSM apparatus. As shown in **Figure 3.8** the VSM has three main parts: 1) the pickup coil, 2) the linear motor, and 3) the sample stage which are all coupled to the PPMS which controls both the temperature and the applied field.

The operation of the VSM is very simple. First the applied field and sample temperature are set by the PPMS, and then the sample is "vibrated" inside the pickup coil by the linear motor at 40Hz. To obtain data the VSM takes advantage of the fact that the static applied field will not induce a current in the pickup coil while the changing field of the vibrating sample will induce an electric current proportional to the magnetic moment of the sample. The time dependent voltage of the coil induced by the vibrating sample is given by the equation

$$V_{coil} = \frac{d\Phi}{dt} = \left(\frac{d\Phi}{dz}\right)\left(\frac{dz}{dt}\right) \tag{2.1}$$

Where Φ is the magnetic flux enclosed by the coil, z is the vertical position of the sample, and t is time. Now if we assume the motion of the sample is in the form of sinusoidal oscillation the voltage can be given by the equation

$$V_{coil} = 2\pi fCmA\sin(2\pi ft) \tag{2.2}$$

Where C is a coupling constant, m is the DC magnetic moment of the sample, A is the amplitude of the oscillation and f is the frequency of the oscillation. This simple equation is the basis for all VSM measurements.

3.2.3 Data Analysis

It is now possible to analyze the measured magnetization of Ag_8GeTe_6. It is clear that Ag_8GeTe_6 is negative (diamagnetic) through the entire temperature range (10K-350K). This in addition to the observation that the magnetization is essentially independent of temperature suggests that Ag_8GeTe_6 is an insulator. Indeed this is the case at low temperatures, though at higher temperatures (room temperature and above) it is well known that Ag_8GeTe_6 behaves like a semiconductor. For this reason I have calculated the ionic contribution to the diamagnetic response with the goal of subtracting the ionic contribution from the total measured signal to end up with the carrier contribution. The ionic diamagnetic susceptibility was calculated by assuming the oxidation states of the ions to be Ag^{+}, Ge^{4+}, and Te^{2-}, and then performing a weighted sum on values for each species found in the literature: $-24x10^{-6}$ emu/mol [Ag^{+}], $-7x10^{-6}$ emu/mol [Ge^{4+}], and $-70x10^{-6}$ emu/mol [Te^{2-}].[40] The resulting calculated value for the ionic diamagnetic susceptibility is $-6.18\ x10^{-4}$ (*emu/mol*formula unit*). From here it is possible to calculate the contribution to the magnetization from the free carriers, but first we must consider the assumptions that go into this calculation: First we have assigned a fixed valence to each of the species though any deficiency of Ag, Te, or even Ge would certainly lead to a shift in valance of at least one of the species. We have also assumed that all of the signal is due to either Pauli Paramagnetism (Pauli PM) or full shell diamagnetism (DM), which is clearly too simple because the measured data displays a slight field dependence though both Pauli PM and DM should both be field independent. Further it is difficult to rigorously justify the shift of the magnetization from negative to

positive after the diamagnetic subtraction. Indeed if directly measured the sign of a value can nearly always be trusted, however, in our case a signal was measured and a slightly larger signal subtracted which changed the sign of the final product. We can argue that most likely the positive signal is real, but with the current information it is impossible to rule out the possibility that the original measured signal was shifted slightly due to a systematic error or inherent uncertainty in the system. The magnitude of the Pauil PM signal obtained by subtracting the ionic diamagnetic susceptibility from the measured signal is shown in **Figure 3.9**.

At this point it is possible calculate the carrier concentration from the Pauli PM contribution to the magnetic signal. First the magnitude of the Pauli term must be calculated using the calculated value of the ionic diamagnetic susceptibility (-6.18×10^{-4} *emu/mol*formula unit*) and the value of the magnetization measured at 3000 Oe. (4.4×10^{-4} *emu/mol*formula unit*) which gives a value of 1.8×10^{-4} (*emu/mol*formula unit*). We can calculate the density of states at the Fermi level, $g(E_F)$, using the relation $\chi_{para} \approx \mu_0 \beta^2 g(E_F)$. Then if we assume the free carriers act as a 3-D Fermi gas we can then calculate the carrier concentration from $g(E_F)$ *that* gives a value of $\sim 10^{16}$ cm^3. It should also be noted that beyond the assumptions mentioned above, in the previous calculation band effects, van Fleck magnetization, and electron-electron interactions have been ignored.

At this point it is important to note that the above analysis is consistent with the low carrier concentration obtained from Hall coefficient measurements (**Chapter 4**). Furthermore we expect that the ground state of Ag_8GeTe_6 is non-magnetic and probably

insulating electron system. Therefore the orbital degree of freedom plays a negligible role in phase transitions mentioned in the introduction and discussed in more detail in the following section.

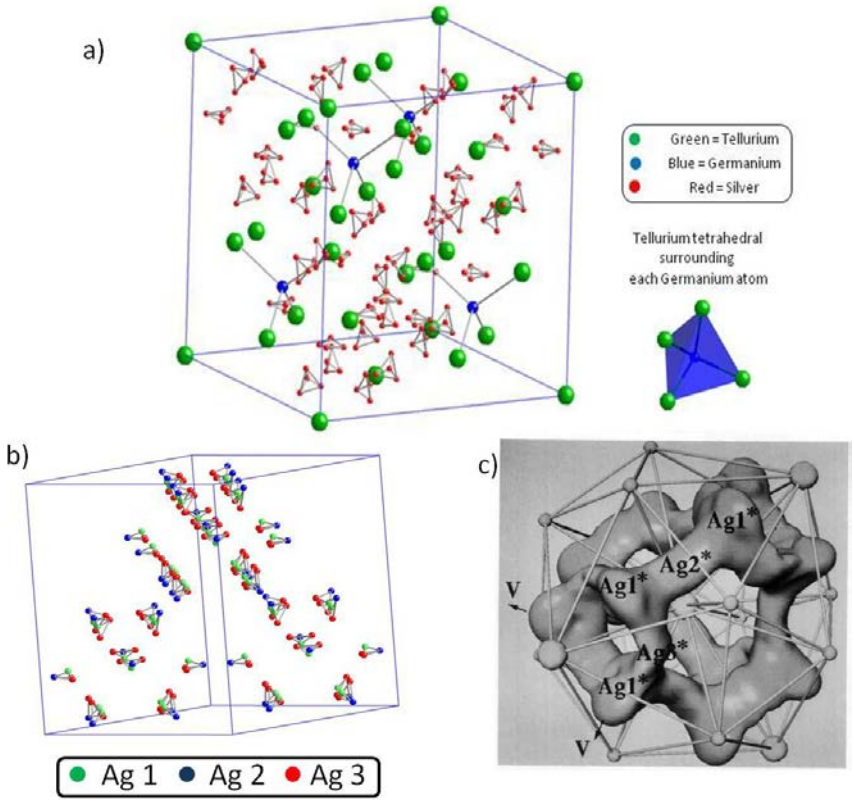

Figure 3.1: a) Complete crystal structure of Ag_8GeTe_6 b) the three distinct silver sites, and c) the ionic diffusion path *Source Ref.[21]*.

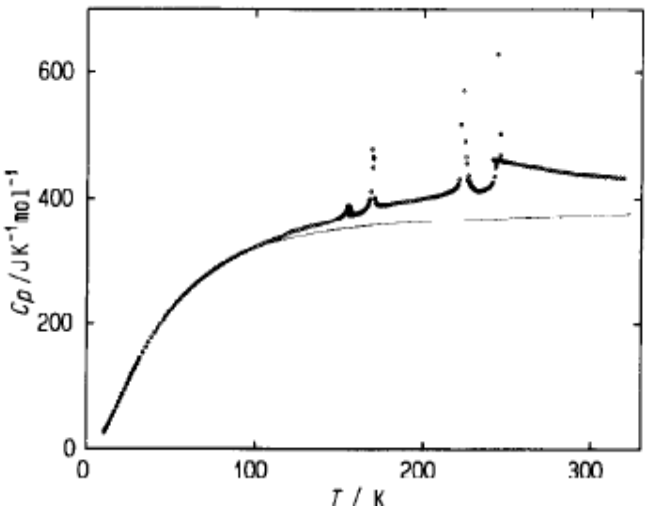

Figure 3.2: Heat Capacity of Ag_8GeTe_6 measured by Kawaji and Atake using a precision DSC. *Source Ref.[37]*

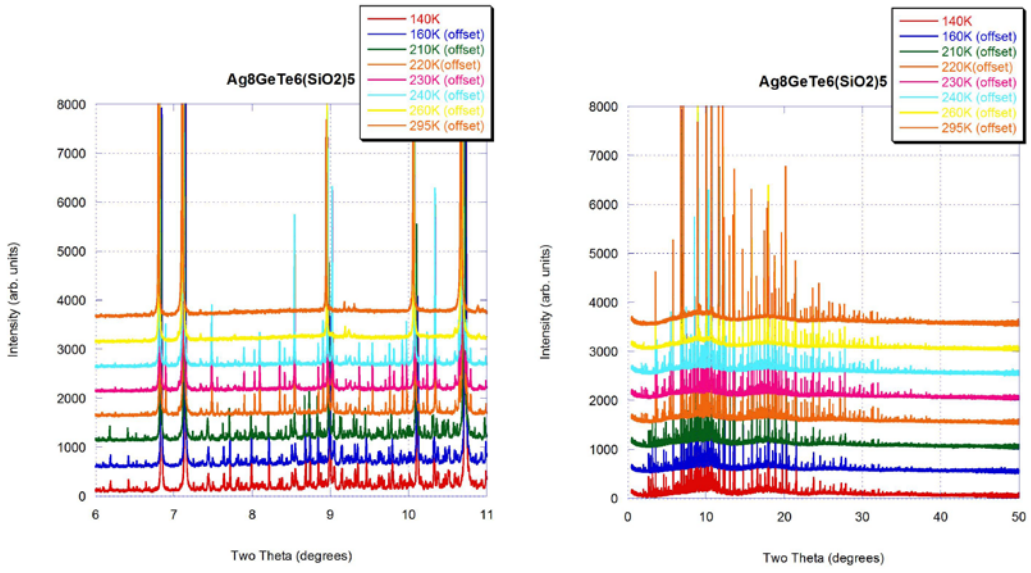

Figure 3.3: Temperature dependent x-ray diffraction pattern of Ag_8GeTe_6. Measured at the Advanced Photon Source (APS) at Argonne National Lab. The circles show the onset of peaks between 240K and 260K as well as between 210K and 220K.

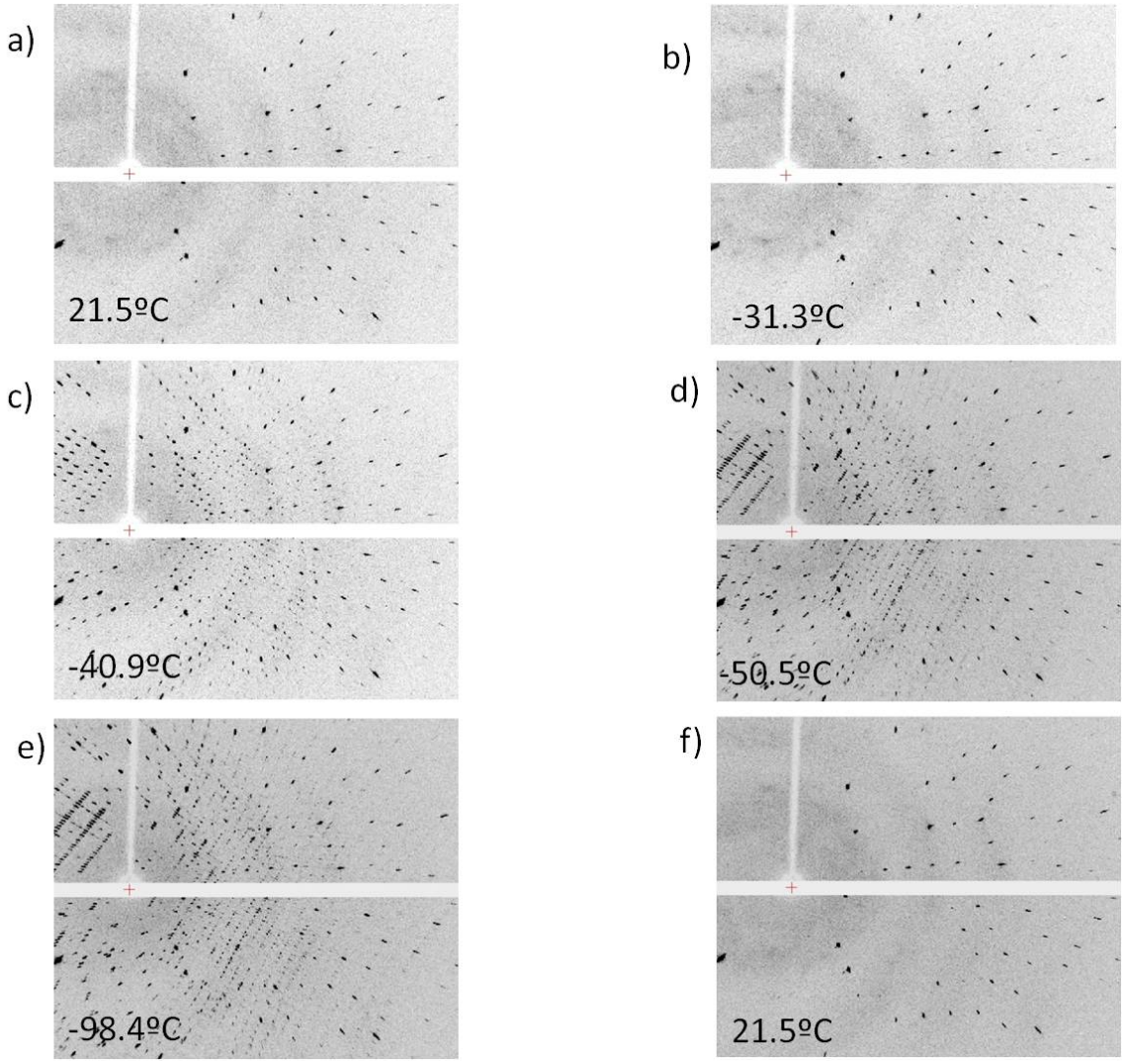

Figure 3.4: Temperature dependent single crystal x-ray diffraction pattern of Ag_8GeTe_6. Measured at Rigaku. The onset of diffraction spots between -30ºC and -40ºC as well as between -40ºC and -50ºC are attributed to structural transitions.

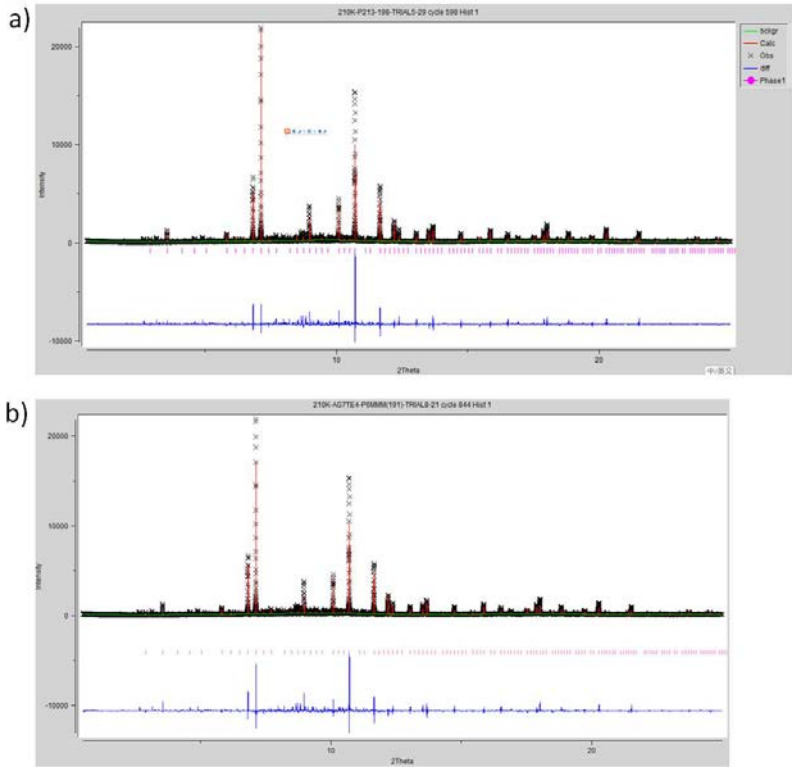

Figure 3.5: Refinement results for Ag_8GeTe_6 at 220 K a) using space group P2(1)3 and 3 distinct Ag sites and b) using space group P2(1)3 and 5 distinct Ag sites.

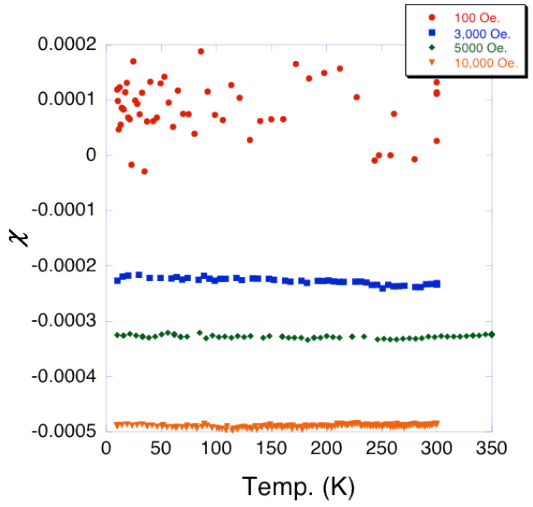

Figure 3.6: The magnetization of Ag_8GeTe_6 as a function of temperature measured using different applied fields.

UNITS FOR MAGNETIC PROPERTIES

Quantity	Symbol	Gaussian & cgs emu [a]	Conversion factor, C [b]	SI & rationalized mks [c]
Magnetic flux density, magnetic induction	B	gauss (G) [d]	10^{-4}	tesla (T), Wb/m^2
Magnetic flux	Φ	maxwell (Mx), $G \cdot cm^2$	10^{-8}	weber (Wb), volt second (V·s)
Magnetic potential difference, magnetomotive force	U, F	gilbert (Gb)	$10/4\pi$	ampere (A)
Magnetic field strength, magnetizing force	H	oersted (Oe),[e] Gb/cm	$10^3/4\pi$	A/m [f]
(Volume) magnetization [g]	M	emu/cm^3 [h]	10^3	A/m
(Volume) magnetization	$4\pi M$	G	$10^3/4\pi$	A/m
Magnetic polarization, intensity of magnetization	J, I	emu/cm^3	$4\pi \times 10^{-4}$	T, Wb/m^2 [i]
(Mass) magnetization	σ, M	emu/g	1 $4\pi \times 10^{-7}$	$A \cdot m^2/kg$ Wb·m/kg
Magnetic moment	m	emu, erg/G	10^{-3}	$A \cdot m^2$, joule per tesla (J/T)
Magnetic dipole moment	j	emu, erg/G	$4\pi \times 10^{-10}$	Wb·m [i]
(Volume) susceptibility	χ, κ	dimensionless, emu/cm^3	4π $(4\pi)^2 \times 10^{-7}$	dimensionless henry per meter (H/m), Wb/(A·m)
(Mass) susceptibility	χ_ρ, κ_ρ	cm^3/g, emu/g	$4\pi \times 10^{-3}$ $(4\pi)^2 \times 10^{-10}$	m^3/kg $H \cdot m^2/kg$
(Molar) susceptibility	χ_{mol}, κ_{mol}	cm^3/mol, emu/mol	$4\pi \times 10^{-6}$ $(4\pi)^2 \times 10^{-13}$	m^3/mol $H \cdot m^2/mol$
Permeability	μ	dimensionless	$4\pi \times 10^{-7}$	H/m, Wb/(A·m)
Relative permeability [j]	μ_r	not defined		dimensionless
(Volume) energy density, energy product [k]	W	erg/cm^3	10^{-1}	J/m^3
Demagnetization factor	D, N	dimensionless	$1/4\pi$	dimensionless

a. Gaussian units and cgs emu are the same for magnetic properties. The defining relation is $B = H + 4\pi M$.
b. Multiply a number in Gaussian units by C to convert it to SI (e.g., $1\ G \times 10^{-4}\ T/G = 10^{-4}\ T$).
c. SI (*Système International d'Unités*) has been adopted by the National Bureau of Standards. Where two conversion factors are given, the upper one is recognized under, or consistent with, SI and is based on the definition $B = \mu_0(H + M)$, where $\mu_0 = 4\pi \times 10^{-7}$ H/m. The lower one is not recognized under SI and is based on the definition $B = \mu_0 H + J$, where the symbol I is often used in place of J.
d. 1 gauss $= 10^5$ gamma (γ).
e. Both oersted and gauss are expressed as $cm^{-1/2} \cdot g^{1/2} \cdot s^{-1}$ in terms of base units.
f. A/m was often expressed as "ampere-turn per meter" when used for magnetic field strength.
g. Magnetic moment per unit volume.
h. The designation "emu" is not a unit.
i. Recognized under SI, even though based on the definition $B = \mu_0 H + J$. See footnote c.
j. $\mu_r = \mu/\mu_0 = 1 + \chi$, all in SI. μ_r is equal to Gaussian μ.
k. $B \cdot H$ and $\mu_0 M \cdot H$ have SI units J/m^3; $M \cdot H$ and $B \cdot H/4\pi$ have Gaussian units erg/cm^3.

R. B. Goldfarb and F. R. Fickett, U.S. Department of Commerce, National Bureau of Standards, Boulder, Colorado 80303, March 1985
NBS Special Publication 696 For sale by the Superintendent of Documents, U.S. Government Printing Office, Washington, DC 20402

Figure 3.7: This table is very useful when converting between different magnetic units. *Source Ref. [39]*

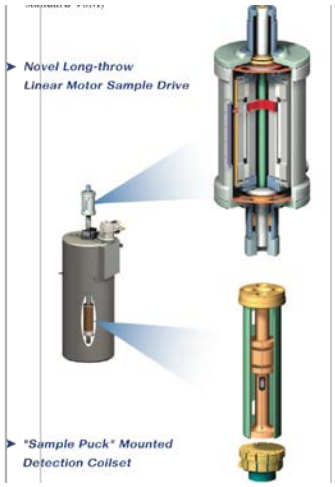

Figure 3.8: Diagram of the Vibrating Sample Magnetometer (VSM). *Source Ref. [41]*

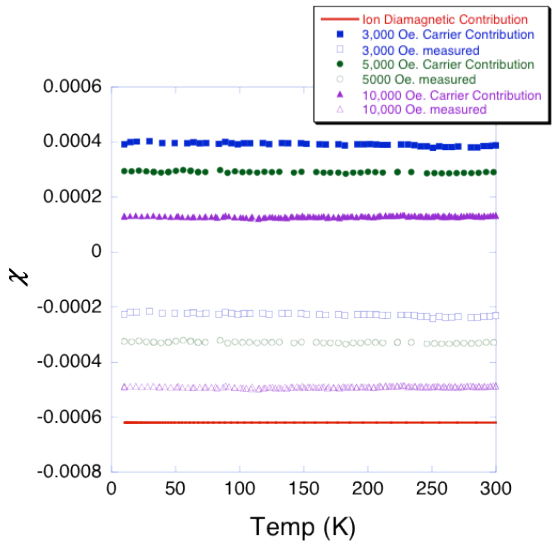

Figure 3.9: Measured magnetic susceptibility as well as the calculated ionic diamagnetic contribution and the carrier contribution to the susseceptibility of Ag_8GeTe_6 as a function of temperature.

CHAPTER FOUR

RESISTIVITY AND SEEBECK COEFFICIENT

As discussed in the previous chapter magnetic susceptibility data precludes the spin and orbital degrees of freedom as driving forces in the phase transitions observed by Kawaji and Atake.[37] With this in mind we attempted to probe the charge degree of freedom in Ag_8GeTe_6 with resistivity and Seebeck coefficient measurements. It is important to measure both Seebeck and resistivity because though they both offer information on the charge carriers and band structure of a material resistivity is a percolative (path dependent) phenomenon while Seebeck is not.

It should be noted that the majority of the following analysis considers the charge conduction in Ag_8GeTe_6 to be due to electrons or holes but *not ions*. This is clearly not completely true, nonetheless, at room temperature and below the fraction of the conductivity due to mobile ions is small and therefore ignored. A more complete analysis of the contribution of ions to the conductivity of Ag_8GeTe_6 can be found in the following section.

4.1 Measurements

4.1.1 Ionic Conductivity

The ionic conductivity of Ag_8GeTe_6, at room temperature, was estimated using two different methods. First the ionic contribution to the conductivity was directly

measured by measuring the conductivity of Ag_8GeTe_6 with an electron blocker in the circuit.[42] Next we attempted to estimate the ionic conductivity of Ag_8GeTe_6 using AC impedance spectroscopy.

Direct measurements of the ionic conductivity using an electron blocker were performed in Dr Steve Creager's lab in the chemistry department at Clemson University. The principle of this type of measurement is quite simple. To perform a measurement the sample is connected in a circuit as shown in **Figure 4.1** with electron blockers on the electrodes, and a traditional two-probe resistance measurement performed using a potentiostat due to the high resistance of the samples.

An electron blocker is a material that allows for the passage of mobile ions, but not electrons. For our measurement we used Ag substituted Nafion as our electron blocker.[43] The Nafion was silver substituted by soaking it in a heated silver nitrate solution for several hours. To promote the diffusion of Ag ions during the measurement the Nafion sheets were also soaked in deionized water directly before the measurement.

For our measurement voltage sweeps were performed using a potentiostat and the current through the sample monitored. The ionic conductivity was then calculated from the slope of the i-V curves. **Figure 4.2a** shows a sample dataset, while **Figure 4.2b** shows the conductivity (slope of the voltage sweeps) as a function of the sweep number. The small variation in the conductivity between sweeps suggests that the data is trustable. When converted to conductivity the measured value of ~1×10^{-5} S*m is quite small suggesting that the contribution of mobile Ag ions to the overall electrical conductivity at room temperature is negligible.

At this point it is important to note that under ambient conditions (room temperature and humidity) the ionic conductivity of Nafion is not very high which means our measurement should be considered to be *a lower limit* for the ionic conductivity of Ag_8GeTe_6.[42,43,44] **Figure 4.2b** shows the measured conductivity as a function of sweep for both dry Nafion and wet Nafion. The measurements conducted with wet Nafion show a much higher conductivity than those performed with dry Nafion because the resistance at the interface is much lower due to the increased ionic conductivity of the Nafion. This interfacial resistance can be considered analogous to contact resistance in a traditional two-probe resistance measurement. Ideally the sample stage would be placed inside a humid chamber at elevated temperatures (~50 °C) to perform the measurement because this increases the ionic conductivity of Nafion, the dimensions of our sample stage made this impossible. For this reason we cannot be certain that all of the measured resistance is due to the sample and not contact resistance which is why we say that the measured value of the ionic conductivity of Ag_8GeTe_6 should be considered a lower limit to the actual value.

We also attempted to measure the ionic contribution to the electrical conductivity using AC impedance measurements. AC impedance measurements were performed between 20°C and 100°C by Mr. Isaac Bredesson in Dr. David Mandrus's group in Department of Materials Science and Engineering Department at the University of Tennessee, Knoxville. Normally the ionic conductivity of a material can be calculated by measuring the AC impedance and modeling the sample to an equivalent circuit made up of resistors and capacitors in parallel. **Figure 4.3a** shows the data measured on

Ag_8GeTe_6. Unlike the usual case of an ionic conductor the data measured on Ag_8GeTe_6 cannot be fit (interpreted) using the model of combined resistance and capacitance (the frequency dependence of the imaginary part is clearly *inductive-like* as it is almost linearly dependent on frequency **Figure 4.3b**). In the case of Ag_8GeTe_6 the impedance can however be modeled using an equivalent circuit made up of a resistor (R_1) and inductor (I) in parallel which together are in series with another resistor (R_2), as shown in **Figure 4.3c**. Fitting the data to the equivalent circuit gives values of 9.5Ω for R_2 10^5Ω for R_1 and 10^{-5} H for I.

One possible explanation for this somewhat unexpected behavior involves the diffusion path of Ag ions through the lattice. **Figure 4.3d**, taken from [21] shows the ionic diffusion path in Ag_8GeTe_6 measured using single crystal x-ray diffraction. Clearly ions diffuse through the Ag_8GeTe_6 crystal structure following a path that has a very strong curvature that may explain the observed *inductive* component in the AC impedance.

4.1.2 Electronic Resistivity

Initial resistivity and Seebeck coefficient measurements of Ag_8GeTe_6 were performed using an in-house custom designed system between 15K and 300K.[45] The system is built around an Advanced Research Systems (ARS) closed circuit He cryostat, and uses differential and four probe techniques to measure Seebeck coefficient and resistivity respectively. In order to facilitate rapid throughput samples are mounted on removable pucks as shown in **Figure 4.4.**

The system is controlled by a Labview® program and operates using a slewing type temperature control in which the heating/cooling rate, but not the actual system temperature is maintained at a preset value controlled by the user. In this way a measurement is made while the system cools at a constant rate. When the cooling power from the cryostat is insufficient to maintain the desired cooling rate the system switches to warming mode and continues to run, while still taking data, until it reaches room temperature. Through the entire run the ΔT across the sample is maintained at a constant value set using a PID control. The system takes data at user-determined intervals in either time or temperature. The magnitude of the current passed through the sample during restively measurements is accurately determined by measuring the voltage drop across a known standard resistor placed electrically in series with the sample.

In order to take a data point the system goes through the following procedure: first a current is passed in the forward direction and the resulting resistive voltage measured, then the current is turned off and the temperature gradient and Seebeck voltage measured, and finally a current, of identical magnitude and opposite sign to the first current is passed through the sample and the resistive voltage measured again. At this point the Seebeck coefficient can be calculated as $\Delta V/\Delta T$ and the resistivity of the sample can be calculated using the equation

$$\rho = \frac{\left(v_{+} - v_{-}\right)}{i}\frac{a}{l} \tag{3.1}$$

where v_+ and v_- are the measured voltages in the forward and reverse directions, i is the current passed through the sample, a is the cross-sectional area of the sample, and l is the length between the voltage leads. As can be seen **Equation (4.1)** the contribution of the

Seebeck voltage is negated by switching the direction of the current between measurements.

It is important to remember that the *slewing type* temperature control is a compromise between accuracy and time, with an eye on the simultaneous measurement of resistivity and Seebeck. Our system has proved to work very well in characterizing a wide range of materials, even some materials that are far from what the system was designed for, i.e. materials with small Seebeck (<20μV/K). Still the compromise between speed and accuracy becomes apparent in several instances including when attempting to track phase transitions, especially when the transitions are close together as is the case in Ag_8GeTe_6. Another example of this limitation became apparent when we attempted to probe ionic conduction, as ionic migration has a much longer "time" scale than its electronic counterpart it is also difficult to track using our in-house system.

In addition to the measurements on our in-house system the resistivity was measured using the ACT option on a Quantum Design PPMS because the information the systems offer is slightly different. Both the PPMS and our in-house system make resistivity measurements in the four-probe configuration, which effectively negates contact resistance, but the PPMS uses an AC current while our in-house system uses a DC current. Moreover the PPMS takes data by stabilizing at each temperature point while the in-house system operates using a slewing method where the rate of change of the temperature (*dT/dt*) is controlled and not the actual system temperature. This is an important consideration since the time scales associated with the thermal relaxation of the sample, the migration of electrons/holes, and the migration of ions are very different,

therefore a slewing type measurement cannot possibly satisfy all three time scales. In the mean time, any dependence of the measured resistivity on the ramping rate, could be a sign of ionic migration assuming that thermal inhomogeneity can be ignored.

The use of an AC current in the PPMS measurements not only automatically removes contributions from any Seebeck voltage or any other stray voltage for that matter but also allows for the use of a much smaller excitation (current density). This is because the system digitally filters out any signals of different form or frequency than the excitation, which removes any DC offset as well as a large portion of the noise.[46] This can be attributed to the fact that the noise is by nature not purely resistive and therefore occur out of phase and at different frequencies than the excitation.

4.1.3 Steady State Seebeck

Since the time scales for ionic and electronic migration (under a temperature gradient) are very different (ps vs. minutes-hours), in a mixed conductor, it should be possible to separate their contributions to the Seebeck coefficient using a time dependent Seebeck measurement. This assumes however that the time scale of the measurement is greater than the longest time scale of the ionic and electronic migration. Indeed one of the main challenges of this project was related to dealing with phenomena in multiple-space and -time domains. A similar study was performed by Park and Yoo in which they claimed to separate the electronic and ionic contributions of the Seebeck of the mixed conductor $Ce_{1-x}Gd_xO_{2-x/2-\delta}$. The results of Park and Yoo's study are shown in **Figure 4.5** for comparison, and they did indeed see a time dependent signal that appears to be due to

the slow migration of ions. With this in mind we designed an experiment to measure the Seebeck as a function of time using a power sweep method.

For this measurement we modified a steady state thermal conductivity system in Dr. Terry Tritt's lab, described in [47] to allow for rapid measurements and fine control of the system temperature. The system shown in **Figure 4.6** is built around an ARS cryostat and controlled using a labview program. The temperature gradient is generated using a 39Ω resistive heater mounted on top of the sample using 5 min. epoxy and measured using a Au–Fe versus chromel differential thermocouple.

In order to take a measurement the base temperature of the system is set and stabilized. Next a user-controlled current is passed through the heater on top of the sample and the voltages (both across the sample and across the thermocouple) monitored in real time. The temperature gradient is then allowed to stabilize before the heater current is increased and another measurement taken.

A sample dataset taken on Ag_8GeTe_6 using our custom system is shown in **Figure 4.7**. Upon initial inspection it appears that we are seeing a contribution from ions similar to what was seen by Park and Yoo.[48] Further inspection of the data, however, suggests that the time dependence of the signal is not from the slow migration of ions but rather due to the low thermal conductivity of Ag_8GeTe_6. Because the thermal conductivity of Ag_8GeTe_6 is so low it takes a very long time for the sample to reach thermal equilibrium, which mimics the signal expected for ionic migration.

To test this scenario I measured the Seebeck of Bi_2Te_3, a common thermoelectric material that is *not* a mixed conductor, using the system. Suprisingly the Bi_2Te_3

measurements showed similar, but not as pronounced features as the measurements on Ag_8GeTe_6. This confirms that the deviations in the data can at least mostly be attributed to deviations from thermal equilibrium, furthermore the fact that the deviations are larger for Ag_8GeTe_6 suggest that it has a lower thermal conductivity than Bi_2Te_3, which will be discussed in detail in **Chapter 6**.

4.1.4 Measurement Considerations

Initial attempts to solder to Ag_8GeTe_6 samples proved very difficult, which incidentally has been observed in many ionic conductors. Therefore Dupont® Silver paste was used to make electrical contacts to the samples. Still contact resistance proved to be a large problem, with contact resistances on the order of kilo ohms observed. In an initial attempt to overcome this issue we mixed the silver paint with powdered Ag_8GeTe_6 a trick Ryoji Funahashi used in oxide thermoelectric studies, however this proved ineffective.[49] A more successful method for lowering the contact resistance involved sputtering gold contacts on the surface of the sample before applying Ag paste. This brought the contact resistance down several orders of magnitude from kilo ohms to ohms. The contacts were sputtered using a Denton Vacuum Desk® 2 sputtering system and scotch tape as a mask.

Due to the unusually low thermal conductivity of Ag_8GeTe_6 the warming and cooling rates in both systems (our in-house R&S system as well as the PPMS) had to be adjusted to ensure the samples were in thermal equilibrium, or at least as close as possible

(we used 0.25 and 0.4 K/min. respectively). This was particularly important when attempting to probe the nature of the phase transitions, which will be discussed in depth later in this chapter.

Furthermore though our desktop x-ray diffractometer showed the samples synthesized at Clemson University to be single phased our initial resistivity and Seebeck measurements showed wide variations from sample to sample. This proved to be a puzzle until high-resolution synchrotron X-ray diffraction at Argonne National Lab revealed that there was indeed at least a small amount of secondary phase present **(Chap. 3)**. To our knowledge this issue has never been addressed by previous investigators possibly leading to errors in both measurement and data analysis.

Figure 4.8 shows the variation of both the magnitude and temperature dependence of the resistivity and Seebeck coefficient of the as grown Ag_8GeTe_6 samples. Indeed the variation of the temperature dependence of the resistivity and Seebeck from essentially insulating to metallic is very surprising. As discussed in **Chapter 3** the presence of a small amount of secondary phase(s) ~1-3% was confirmed by synchrotron x-ray measurements. Previous work on Ag_8GeTe_6 suggests that it is a *low carrier system* hence small changes in the composition of samples can have drastic changes in the electrical properties.[19,20,25] Synchrotron x-ray data suggested that the secondary phase is Ag_5Te_3, and though little is known about the electrical properties of Ag_5Te_3 comparison with its sister compound Ag_2Te suggests it has a much higher carrier concentration than Ag_8GeTe_6. There are two scenarios that could explain how a small amount of high carrier concentration/mobility secondary phase can lead to the observation of such a wide range

of electrical properties from samples that appear to be identical when compared using a bench top x-ray. First the secondary phase may form an interconnected path on the grain boundaries of the Ag_8GeTe_6 samples. A second more likely explanation involves charge transfer from the carrier-rich phase to the low carrier matrix, by "modulation doping".[50] The fact that peaks in the XRD spectrum are quite sharp, suggests that if the secondary phase does in fact form of a layer on grain boundaries, it cannot be too thin which suggests that modulation doping is a more likely scenario. This problem alone took us ~ 1 year to solve by altering the synthesis process to minimize the impact of incongruent melting that occurs at 645° C.

With this in mind we have carefully chosen data that we believe reflects the intrinsic behavior of Ag_8GeTe_6 based on two criteria.

(i) One criterion for choosing samples that we believed to show "intrinsic" behavior was the low temperature (<50K) resistivity. In this way we assumed that samples that showed the highest low temperature resistivity contained less secondary phase because the increased resistivity is a sign of a decreased carrier concentration.

(ii) The second criterion for choosing samples that we believed to show "intrinsic" behavior was the signature of the four phase transitions below room temperature. The existence of these transitions is well documented therefore we assumed that they are real and that samples with a signature of the transitions in resistivity contain less secondary phase than those that don't.

4.2 Data Analysis

As can be seen in **Figure 4.9a** the DC resistivity of Ag_8GeTe_6 increases rapidly with decreasing temperature. At first glance, it is characteristic of a semiconductor and consistent with what has been reported above room temperature.[19,20,25] However, closer inspection of the data above 100K, **Figure 4.9b**, suggests that the resistivity behavior can be divided into three regions: a low temperature region (region I, below 140K) which displays a negative temperature coefficient of resistance (TCR), a second region (region II, between 140K and 250K), which contains all four of the phase transitions and on the whole displays a positive TCR, and a third region (region III, between 250K and 300 K) that again shows a negative TCR.

Unlike the resistivity the Seebeck coefficient of Ag_8GeTe_6 does not show drastic changes of slope as a result of the phase transitions (**Figure 4.9c**), but is nonetheless useful in understanding the nature of the electronic properties of Ag_8GeTe_6.With this in mind we have probed the nature of the electronic properties of Ag_8GeTe_6 using resistivity, Seebeck coefficient, and finally Hall coefficient.

As compared to resistivity Seebeck coefficient is a more robust reflection of the energy-dependent electronic states and insensitive to the microstructure, especially grain boundaries. Furthermore, comparison of resistivity and Seebeck with respect to various external control parameters such as temperature and composition is especially informative. Given the secondary phases, mostly likely at the grain boundaries, and their

impact on the electrical resistivity, Seebeck is well suited to provide us with extra insight into the charge and entropy flow in Ag_8GeTe_6.

Region	Temperature Dependence of Resistance (TCR)	Temperature Dependence of Seebeck
I	Negative	$T^{1/3}$
II	Positive	$T^{1/3}$ or linear
III	Negative	Linear transitioning to 1/T

Table 4.1: Temperature dependence of the resistivity and Seebeck coefficient of Ag_8GeTe_6 in different temperature regimes below room temperature.

4.2.1 Low Temperature Regime (below 140K)

In the low temperature regime, below the lowest phase transition at 145K, the conduction of Ag_8GeTe_6 is not band in nature, but rather governed by hopping mechanisms. In particular the conduction appears to be governed by Mott type variable range hopping (VRH).

The VRH model, used to describe systems in which the electrical conduction is governed by disordered induced localization of charge carriers, was developed by Mott in 1969. In these systems the low temperature conductivity is well described by localized electronic states between which carriers "hop" with varying probabilities proportional not only to the distance separating the states, but also the difference in energy between them.[51] According to the VRH model the expression for electrical resistivity can be written as

$$\rho(T) = \rho_0 \exp\left(\frac{T_0}{T}\right)^{1/d+1} \quad (3.2)$$

where *d* is the dimensionality of the material. In this case it is important to note that the dimensionality is not spatial but rather related to the number of degrees of freedom of the charge carriers. **Figure 4.10** shows a plot of *ln(ρ) vs. both* $T^{-1/3}$ *and* $T^{-1/4}$ for Ag_8GeTe_6 between 10K and 300K (2d and 3d VRH). Clearly the VRH model is not well suited to describe the conduction of Ag_8GeTe_6 in the entire temperature range (at high temperatures the plot is far from linear), but is most likely the dominant conduction mechanism between 10K and 140K (the plot shows good linearity). Surprisingly the plot of *ln(ρ) vs.* $T^{-1/3}$ (2d VRH)shows better linearity that the plot of *ln(ρ) vs.* $T^{-1/4}$ (3d VRH) suggesting that the charge carriers in Ag_8GeTe_6 only have two degrees of freedom though the crystal structure is clearly three dimensional. One possible explanation of this behavior is that the density of states is not constant in the temperature range of interest. In his model Mott assumed a constant density of states at the Fermi level which may not be the case in Ag_8GeTe_6. Efros and Shklovskii have proposed another model for 3d VRH in which the DOS vanishes quadratically at the Fermi level, which leads to a $T^{-1/2}$ law for resistivity. This does not appear to be the case for Ag_8GeTe_6 (the plot of *ln(ρ) vs.* $T^{-1/2}$, **Figure 4.10c**, does not appear linear)however it does show one possibility of how Mott's law can vary when the DOS is not constant.[52]

The presence of VRH conduction is supported by the Seebeck coefficient measurements. In the Mott picture the Seebeck coefficient should be described using the equation

$$\alpha \propto T^{\frac{d-1}{d+1}} \tag{3.3}$$

Figure 4.11 shows the Seebeck as a function of temperature as well a fit of the measured Seebeck to **Equation (4.3)** with *d=2* as suggested by the resistivity data. Unlike the resistivity the Seebeck coefficient can be fit fairly well through the entire temperature range using the VRH model. Again though the Seebeck can be well fit using a 2d VRH model it is also possible that the conduction is 3d and the DOS is not constant.

Another concern with using the VRH model to describe the low temperature electrical properties of Ag_8GeTe_6 is the temperature range between 15K and ~50K. In this range both the measured resistivity and Seebeck are larger that the values predicted by the VRH model. There are two possible explanations for this deviation: First it is possible that the samples are so resistive at low temperatures that it acts as a capacitor storing charge during the resistance measurement. This would cause the measured resistivity to increase by offering another path for the current to flow through, but it would also increase the measured Seebeck coefficient by adding to the change on the sample, which would contribute an anamolous voltage to the Seebeck measurement. This hypothesis is supported by the fact that both the magnitude and sharpness of the low temperature "hump" in Seebeck increase when a larger current is used for the resistivity measurement, **Figure 4.12b**.

The second possibility is that the "hump" in resistivity is due to phonon drag. Phonon drag refers to an electron-phonon coupling phenomenon in which the Seebeck coefficient is enhanced due to the coupling between the charge carriers and the heat flow in absence of phase transition and charge current. In most cases phonon drag is

understood in the context of long mean free path carriers coupled to phonons, and exhibits as a gentle hump centered at ~ 20% θ_D, where θ_D is Debye temperature. In this sense the feature does indeed bear a striking resemblance to the characteristic phonon drag peak. This is in direct violation, however, of the observation of VRH conduction which results in very short electron mean free paths.

Clearly long mean free path carriers coupled to phonons can generate a well-defined signature of phonon drag, however a closer look at the mechanisms governing this phenomenon offer another explanation. According to [53] and [54] the magnitude of S^p, the phonon drag contribution to the total Seebeck coefficient, is proportional to the ratio of phonon mean free path to charge carrier mean free path. In a VRH electron system in which the charge carriers have very short mean free path, one would expect to see a large S^p term, which could possibly be resolved on top of the relatively large intrinsic Seebeck of a VRH material. Furthermore though phonon drag should have a small or even negligible signature in the resistivity of a metal, in a hopping system, the resistivity should be more sensitive to the change of momentum transfer so it is at least plausible to see some change in resistivity. Shown in **Figure 4.12a** the resistivity, measured simultaneously with the Seebeck coefficient during the four runs discussed above, appears to display a feature around the same temperature as the onset of the phonon drag peak (the peak is most pronounced in the "run 4" data).

At this point it is impossible comment definitively on the nature of the “hump” in Seebeck coefficient. Further measurements are needed in order to determine whether it is the result of an experimental error or an intrinsic feature due to phonon drag. This is an

important observation, because it opens the possibility that Ag_8GeTe_6 exhibits strong electron-phonon coupling.

4.2.2 Phase Transitions and the Intermediate Temperature Range

Figure 4.9b shows the resistivity of Ag_8GeTe_6 in the intermediate range (140K-250K). Of particular interest in this temperature range are the signatures of the four phase transitions previously identified in C_p. All four transitions are accompanied by a discontinuity in the resistivity and three of the four also display a hysteresis loop. In general the presence of a hysteresis loop in resistivity is a strong indicator of a first order phase transition. This supports Kawaji and Ataki's assertion that all four of the phase transitions below room temperature are first order.[37] In particular the phase transition at 156K shows a beautiful hysteresis loop and a transition from a positive temperature dependence back to a negative temperature dependence reminiscent of a metal-insulator transition (MIT). Unlike the other three transitions the transition at 169K does not show a hysteresis loop, but does show both a discontinuity and a change in slope in resistivity. Like the low temperature phase transitions the upper two transitions are featured by discontinuities. Additionally the upper two transitions display large separations between the warming and cooling curves that do not converge. This separation can most likely be attributed to deviations from thermal equilibrium due to the onset of superionic. If this is the case a hysteresis without closed loop can be explained in the context of Ag^+ ion migration because the ionic kinetics have a much longer time constant than their electronic counterpart.

In the region between the phase transitions (160K-220K) the resistivity displays a positive TCR similar to a metal however the magnitude is much too large to be metallic. In this range the Seebeck also appears to be near linear (at least on the cooling curve), but again its magnitude is also much too large to be metallic. At this point further discussion of the nature of the electrical conduction in this regime would be little more than conjecture.

4.2.3 High Temperature Regime

In the high temperature regime the resistivity again displays a negative TCR, but doesn't appear to follow Arrenhius law, **Figure 4.13**. One possibility for the deviation is the onset of ionic conduction. Obviously any attempt to analyze the electrical properties of Ag_8GeTe_6 in this temperature range that does not take into account the effects of ionic conduction is too simplistic. On the other hand it is well known that fast ionic conduction is governed by a thermally activated hopping. Following the equation

$$\sigma = \sigma_0 \exp\left(-E/RT\right) \tag{3.4}$$

or possibly

$$\sigma = \frac{\sigma_0}{T} \exp\left(-E/RT\right) \tag{3.5}$$

where E is either the activation energy of the mobile ions or in some cases the energy needed for the creation of interstitial defects or vacancies necessary for ionic conduction.[55] In this way the contribution of ionic migration to the electrical properties of Ag_8GeTe_6 below room temperature can again considered to be small.

The Seebeck coefficient appears to level off in this range transitioning to a negative slope with increasing temperature as reported in [19] and [20]. This is in line with a transition from hopping conduction to band conduction, which is also supported by the negative slope of the resistivity.

4.2.4 Hall Coefficient

Hall coefficient measurements were performed on a Quantum Design PPMS, using the standard 5 probe configuration. In a four probe Hall measurement the largest source of error is misalignment of the voltage leads. For this reason in the PPMS the three voltage leads are used, as shown in **Figure 4.14**, and balanced electronically using a bridge to remove any resistive contributions to the measured voltage. For the measurement samples were mounted on a Quantum Design AC Transport puck, and thermally sunk using Apiezon N-grease to ensure thermal stability. The leads were attached using silver paste on top of gold sputtered contacts to ensure that the contacts were ohmic (the addition of gold sputtered contacts lowered the contact resistance from hundreds of Ohms to about 1 ohm). The Hall resistivity was measured between -1T and 1T from room temperature down to approximately 20K.

The Hall coefficient, R_H, was calculated as the slope of the Hall resistivity versus field plot. As can be seen in **Figure 4.15b** the data showed very good linearity. The Hall coefficient as a function of temperature is shown in **Figure 4.15c**. It should be noted that the plotted Hall data was taken on multiple samples with multiple runs to confirm that the measured values were indeed intrinsic to Ag_8GeTe_6. After calculating the Hall

coefficient it was possible to estimate the carrier concentration (**Figure 4.15a**) *n*, using the equation below

$$R_H = \frac{1}{ne} \tag{3.6}$$

where *n* is the carrier concentration and *e* is the charge of an electron (1.60217 x 10^{-19} C). This equation for carrier concentration comes from a single band parabolic model which is clearly not valid in this case. As discussed in the previous section at low temperatures the electrical conductivity of Ag_8GeTe_6 is governed by hopping mechanisms while at higher temperatures the contribution from mobile ions is not negligible, therefore should not be considered to be rigorous, but rather used as cross check of the order of magnitude and temperature dependence of the carrier concentration.

As can be seen in the plot the carrier concentration has a very small magnitude for a semiconductor (10^{17} cm^{-3}), and displays a slight positive temperature dependence. When considered in the context of the resistivity, poorly semiconducting, the small concentration and temperature dependence is expected. From here it is possible to calculate the carrier mobility, μ_H, using the formula below

$$\mu_H = \frac{R_H}{\rho} \tag{3.7}$$

where ρ is the electrical resistivity. The calculated carrier mobility, μ_H, is shown in **Figure 4.15d**. Again it must be noted that the carrier concentration and hence the mobility is calculated using the assumption of a single parabolic band which isn't necessarily correct in the case of Ag_8GeTe_6, and for this reason only the magnitude and temperature dependence of the mobility will be considered. Surprisingly the carrier

mobility displays a slight positive temperature dependence similar to the carrier concentration.

As discussed in the previous section, the electronic conduction of Ag_8GeTe_6 is governed by hopping mechanisms, specifically Mott VRH, at low temperatures. Grunewald et al. have a concise description of the Hall coefficient of a hopping conductor using percolation theory.[56] It is very important to remember that this theory is developed in the approximation of a constant DOS which may not the case in Ag_8GeTe_6, but nonetheless should still offer some physical insight. According to this description the Hall coefficient of a VRH conductor should be described the relation

$$\ln R_H \propto \left(\frac{T_0}{T}\right)^S \tag{3.8}$$

and the hall mobility should follow the relation

$$\ln \mu_H \propto -3/8\left(\frac{T_0}{T}\right)^S \tag{3.9}$$

where

$$S = \frac{1}{d+1} \tag{3.10}$$

where, as before, *d* is the dimensionality of the material. With this in mind **Figure 4.16** shows the log of the Hall coefficient (R_H) and Hall mobility (μ_H) of Ag_8GeTe_6 plotted versus $T^{-1/3}$ and $T^{-1/4}$. As was the case with resistivity and Seebeck both 2d and 3d VRH give a reasonably good fit, however the 2-d fit appears to be more linear.

4.2.5 Photoacoustic Spectroscopy (PAS)

In order to verify the band gap (or energetic barrier for hopping) of Ag_8GeTe_6 photoacoustic spectroscopy (PAS) measurements were performed by Dr. Narayanan

Kuthirummal at the College of Charleston. PAS is a nondestructive spectroscopy tool that is particularly useful for the characterization of optically opaque samples based on the photoacoustic effect discovered by Alexander Graham Bell in 1880 in which sound waves are generated by a solid sample which has absorbed light from a pulsed source. To perform a PAS measurement a sample is placed in an airtight chamber and illuminated with a monochromatic time varying (either pulsed or sinusoidal) light source. The response of the sample is then monitored with a microphone.[57] The physical mechanisms responsible for the PAS signal include 2 main phenomena. The signal should be due to the excitation of electrons or phonon modes in the crystal.

As can be seen in **Figure 4.17** there is a step-like feature in the PAS spectrum of Ag_8GeTe_6 with an onset at 3500 wavenumbers, which corresponds to an energy of 0.406eV. This transition can be attributed to the electronic mobility-gap. This value is in good agreement with the value of 0.47eV measured by Bendorius et al. using optical spectroscopy.[58]

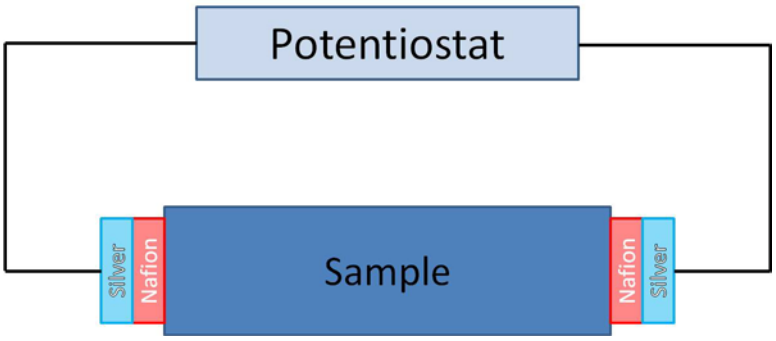

Figure 4.1: Diagram of the experimental setup used to perform an ionic conductivity measurement using the electron blocker approach in the two probe configuration.

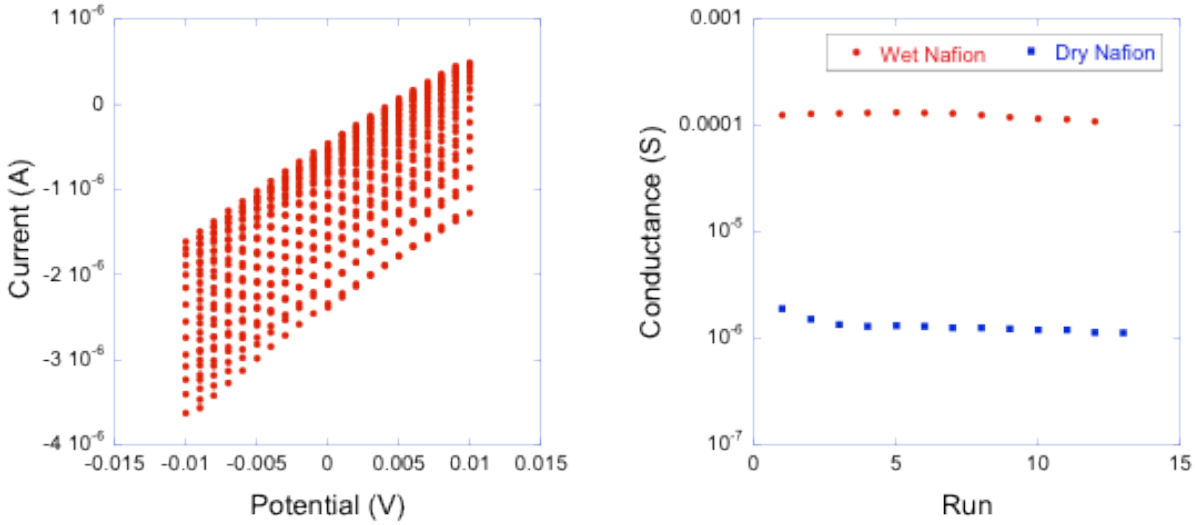

Figure 4.2: a) sample I-V curve b) conductivity versus sweep measured using *wet* Nafion v *dry* Nafion

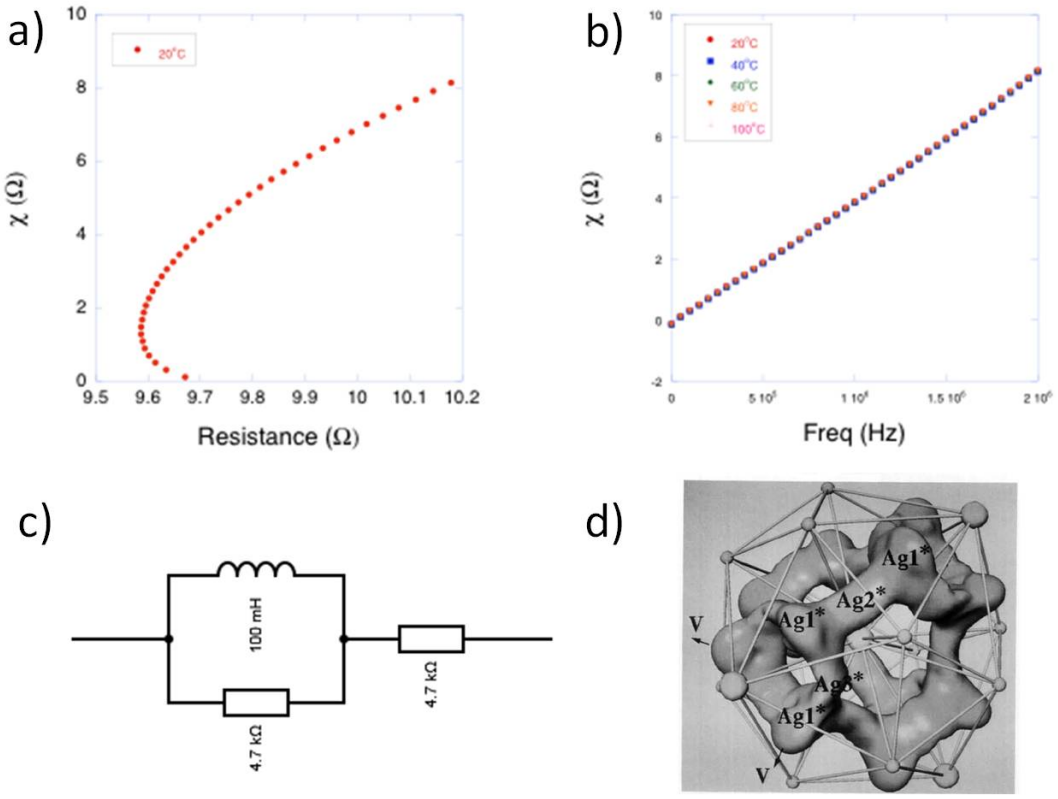

Figure 4.3: a,b) AC impedance of Ag_8GeTe_6 measured at room temperature c) equivalent circuit used to model the impediance data d) Ag^+ diffusion path through the Ag_8GeTe_6 lattice measured by Boucher et al. *Source Ref. [21]*

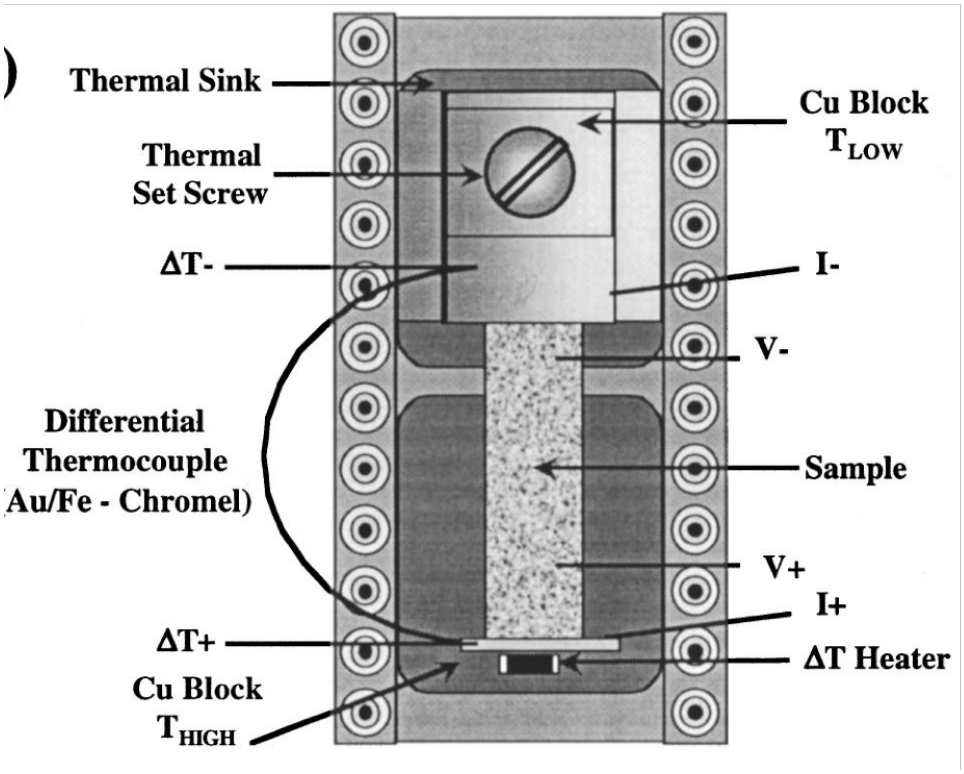

Figure 4.4: Removable sample puck for low temperature resistivity and Seebeck coefficient measurements. *Source Ref. [47]*

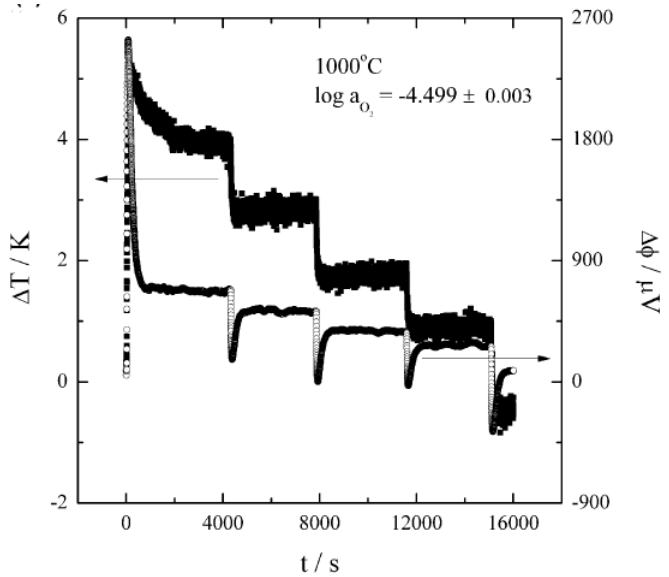

Figure 4.5: Temperature gradient and potential as a function of time measured on $Ce_{1-x}Gd_xO_{2-x/2-\delta}$ taken from [48]. The peaks that appear in potential immediately after changes in temperature are attributed to the slow migration of ions in the system.

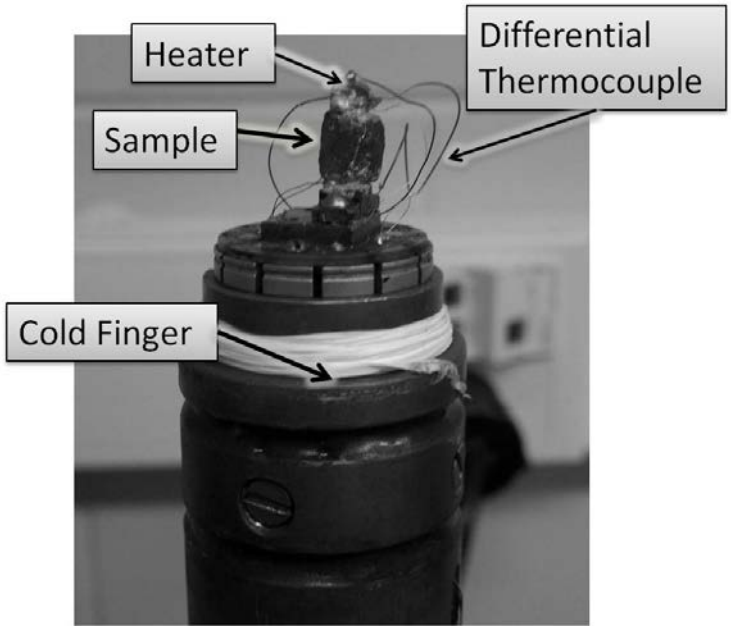

Figure 4.6: Sample mounted in the time dependent Seebeck system built at Clemson.

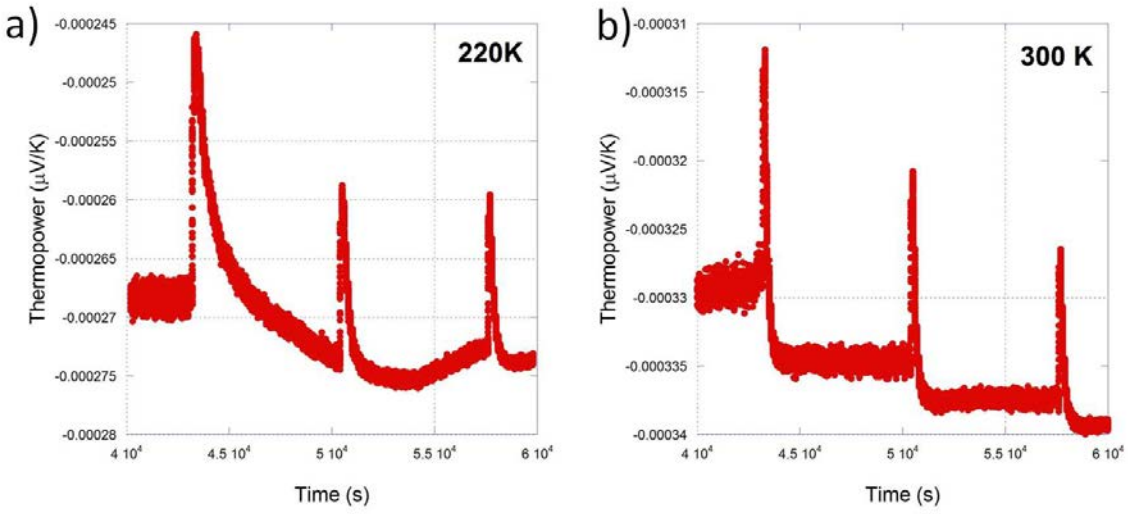

Figure 4.7: Sample dataset taken on Ag_8GeTe_6 taken on the time dependent Seebeck system.

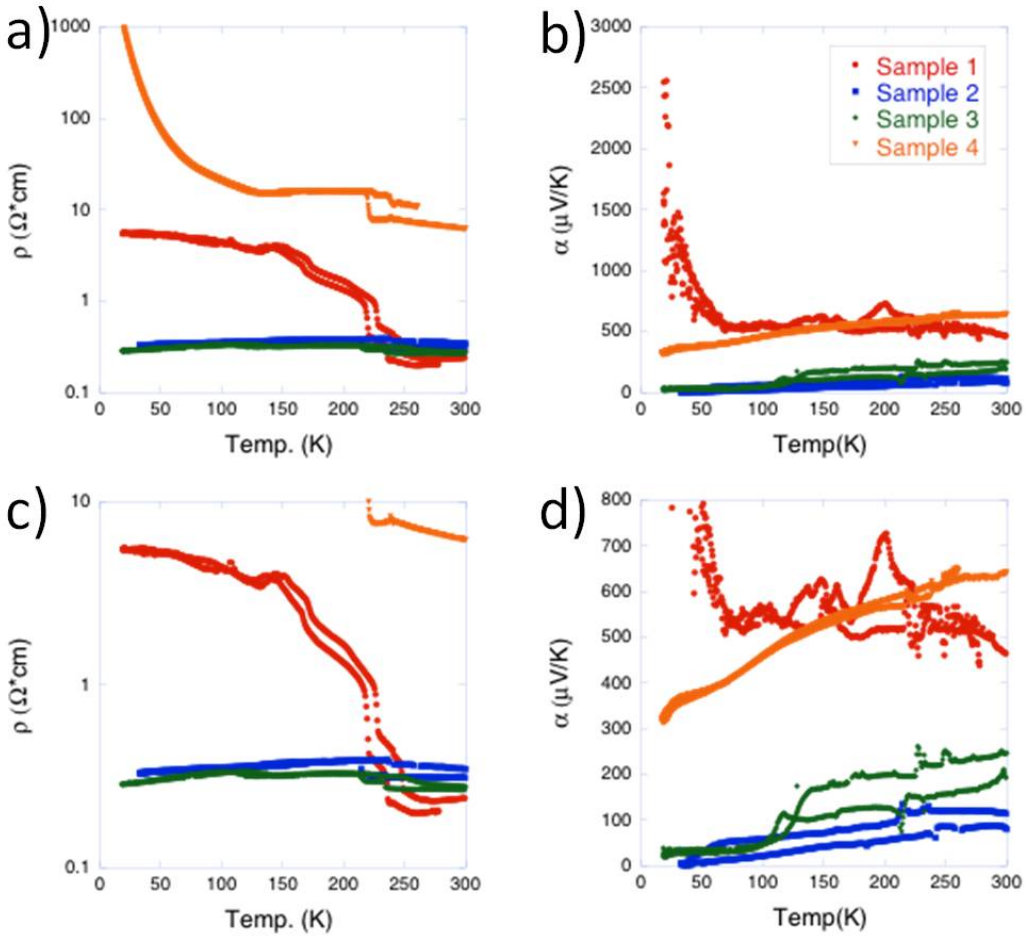

Figure 4.8: Variation of electrical properties between Ag_8GeTe_6 samples.

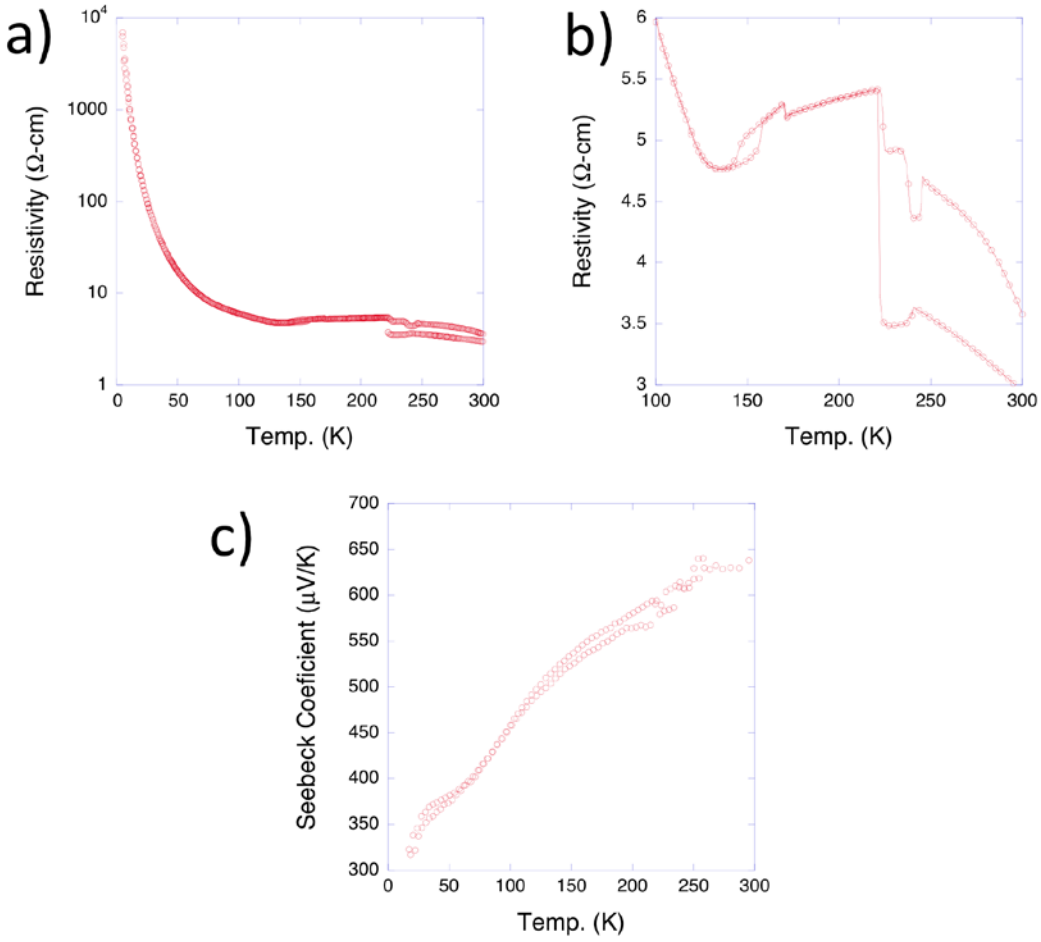

Figure 4.9: a,b) Resistivity and c) Seebeck coefficient of Ag_8GeTe_6 as a function of temperature.

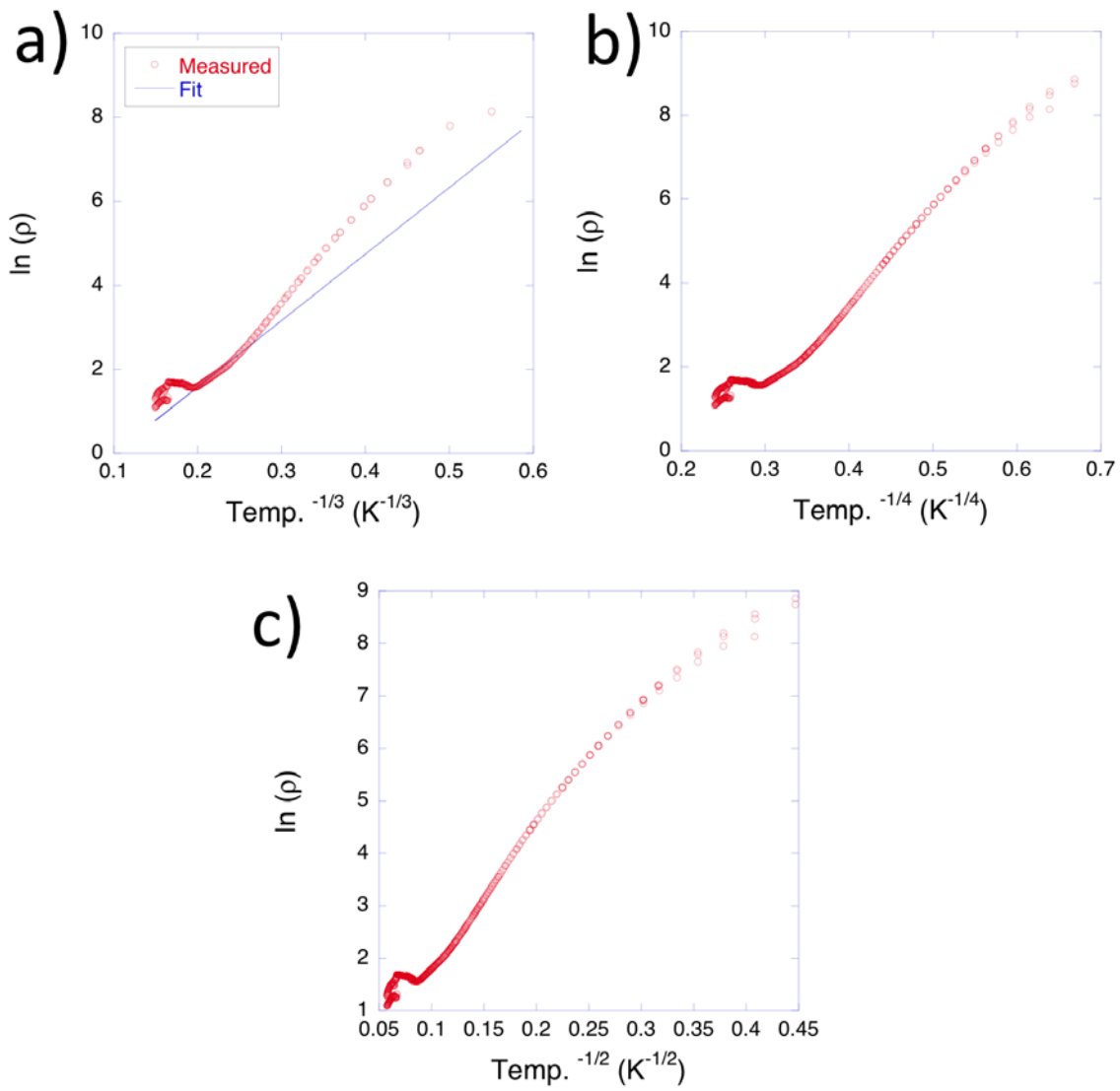

Figure 4.10: a)Clearly the VRH model is not well suited to describe the conduction of Ag_8GeTe_6 in the entire temperature range (at high temperatures the plot is far from linear), but is most likely the dominant conduction mechanism between 10K and 140K (the plot shows good linearity b) 3-d VRH c) tempertaure dependence of conductivity as predicted by Efros and Shklovskii

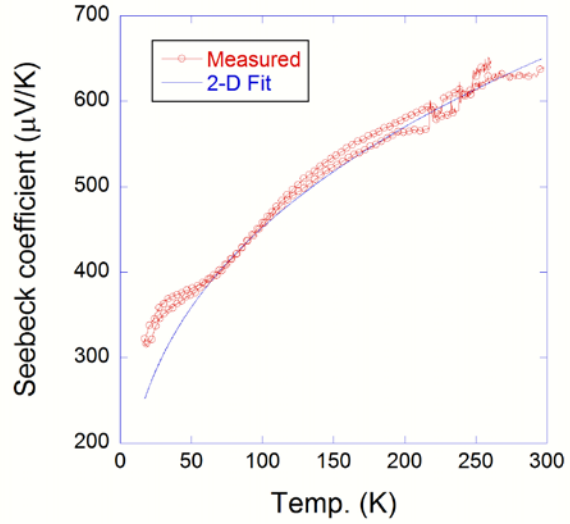

Figure 4.11: a)Seebeck coeifficient of Ag_8GeTe_6 fit to a 2-D VRH model

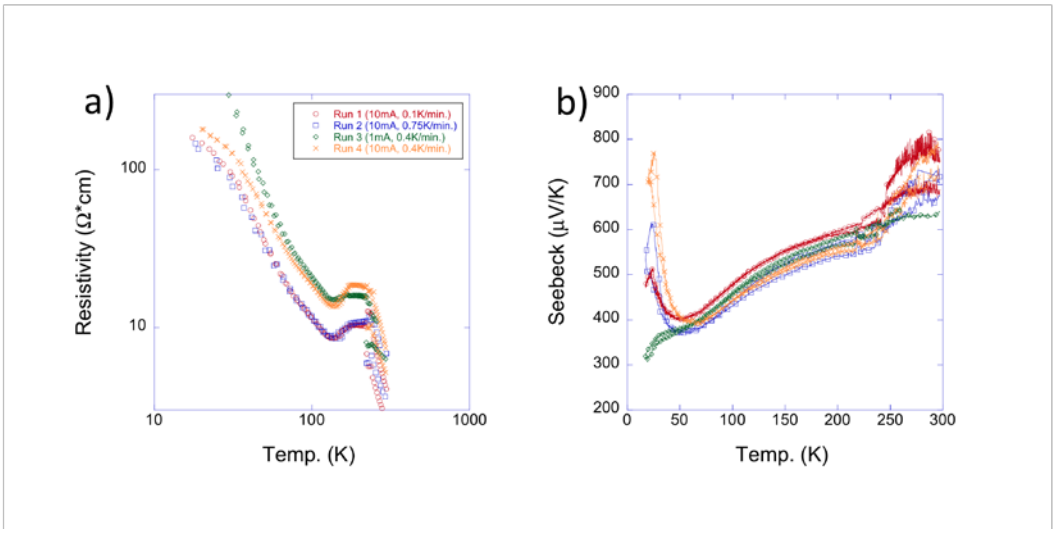

Figure 4.12: a)Resistivity and b) Seebeck coeifficient of Ag_8GeTe_6 measured using different excitations.

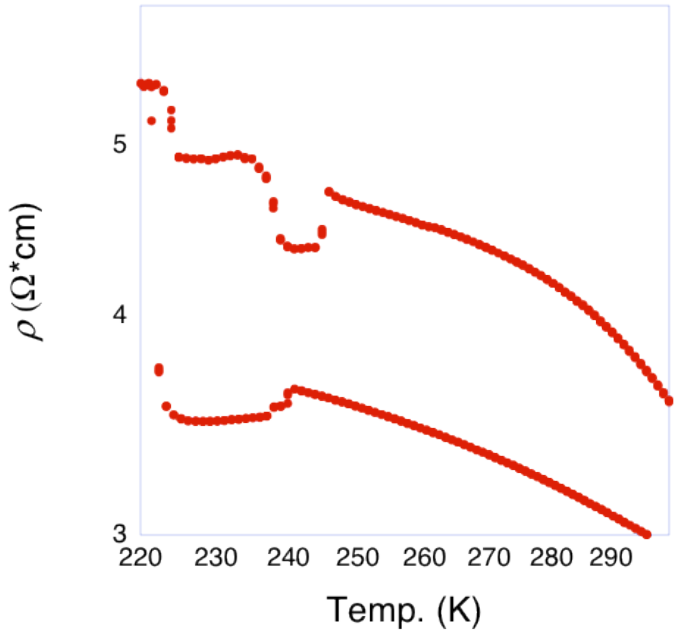

Figure 4.13: Arrenhius behavior of resistivity.

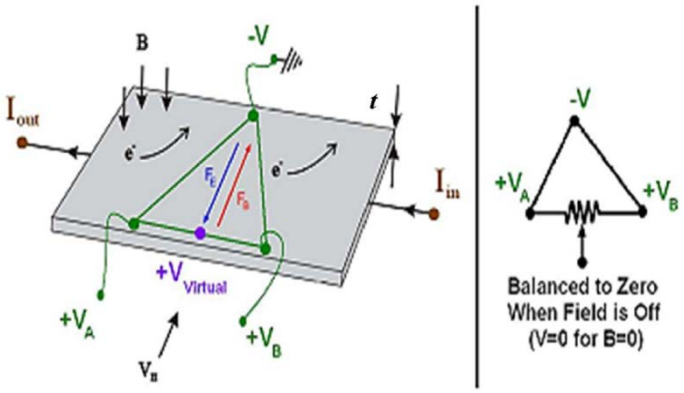

Figure 4.14: a) 5 wire Hall measurement configuration *Source Ref. [4]*.

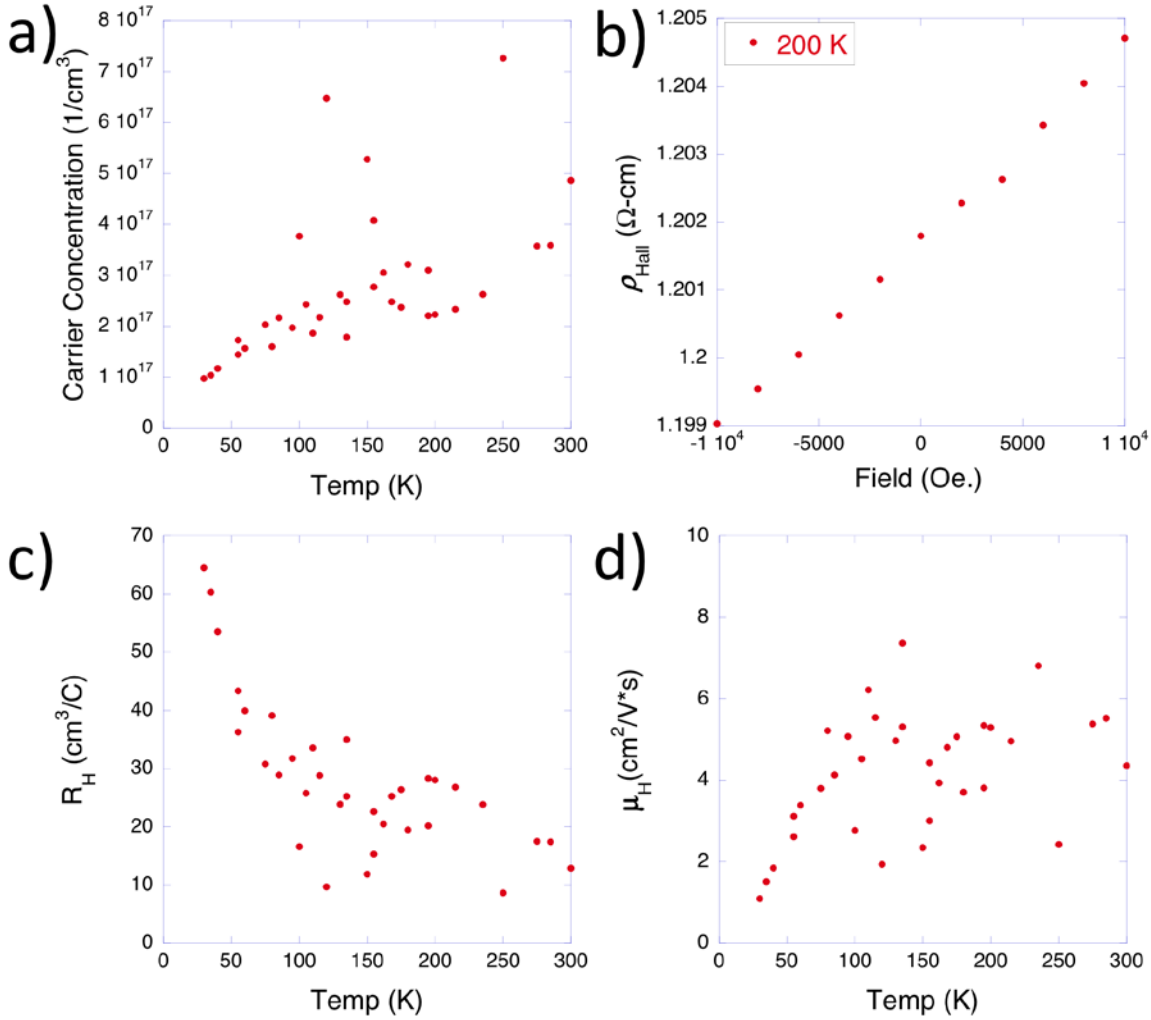

Figure 4.15: a) carrier concentration b) an example of a field sweep (performed at 200K) c) the Hall coefficient as a function of temperature d) the Hall mobility of Ag_8GeTe_6 as a function of temperature.

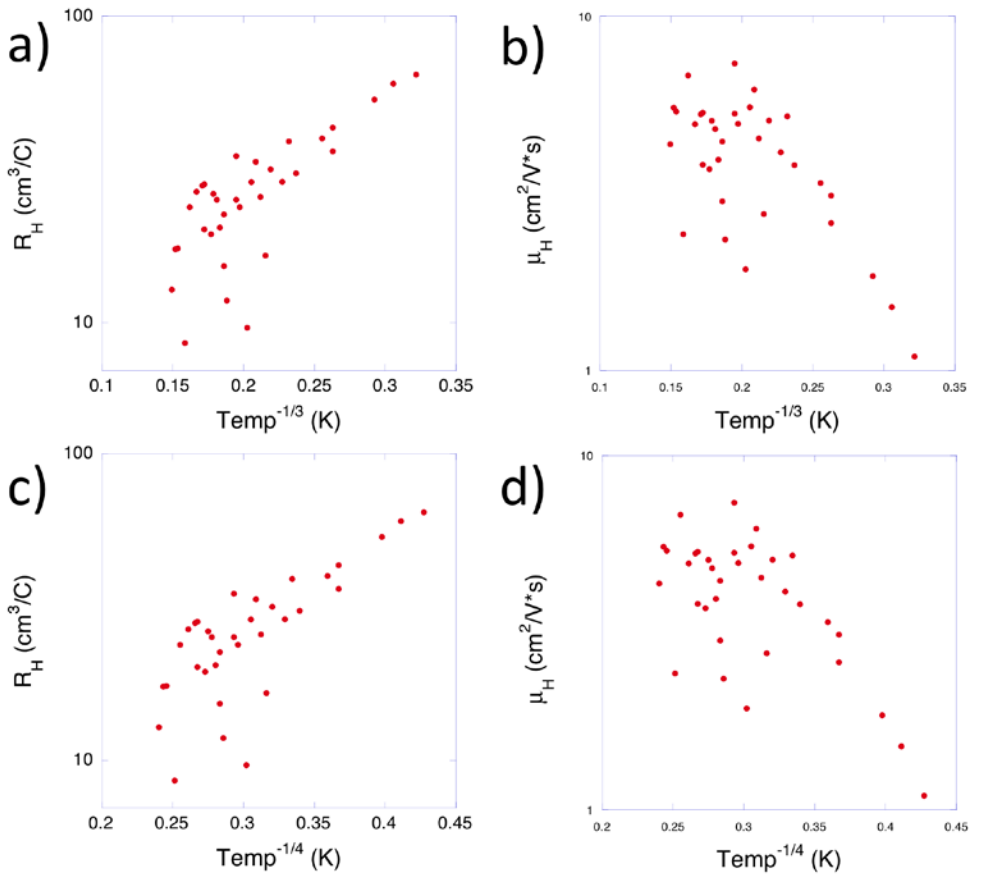

Figure 4.16: a,c) Hall coeifficient and b,d) Hall mobility of Ag_8GeTe_6 plotted versus $T^{-1/3}$ and $T^{-1/4}$

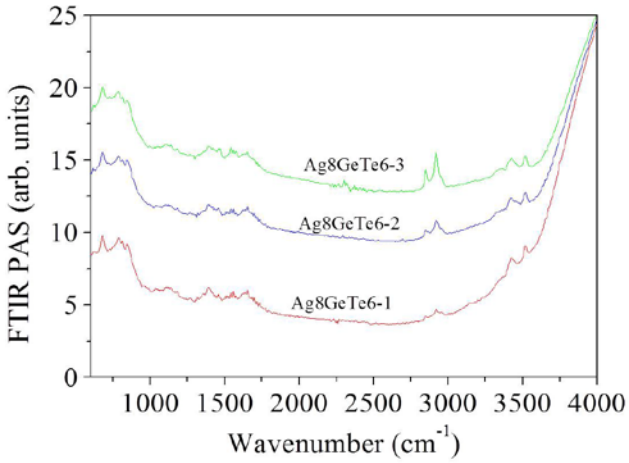

Figure 4.17: PAS spectrum of Ag_8GeTe_6.

CHAPTER FIVE

SPECIFIC HEAT

5.1 Preface

Though it is somewhat unusual to have a preface for an individual chapter, the central importance of this chapter warrants a preface. The preceding chapters addressing magnetic susceptibility, electrical resistivity, thermopower, photoacoustic spectroscopy, and X-ray diffraction allow for an unprecedented level of understanding on the physical nature of Ag_8GeTe_6. Specifically, these results have corroborated that (*i*) the ground state of Ag_8GeTe_6 is non-magnetic (i.e., no long range magnetic ordering down to 2 K) and electrically insulating; (*ii*) Ag_8GeTe_6 is a low carrier concentration yet low mobility electron system; (*iii*) the electrical conduction is basically electronic and it adopts a variable range hopping below the phase transition at 245 K, above which ionic conduction sets in and precludes fast ionic conduction at elevated temperatures; (*iv*) several of the four phase transitions between 150 K and 250 K appear to be first order, at least, the two transitions at 223 K and 245 K involve a crystal symmetry change; and (*v*) time-dependent thermopower measurements suggest a long thermal relaxation time and thus a very low thermal conductivity. Given the small magnitude of the total electrical resistivity in the temperature range studied, the total thermal conductivity is basically the lattice (phononic) thermal conductivity.

From the few thermoelectric studies of Ag_8GeTe_6 above room temperature, the exceptionally low thermal conductivity of Ag_8GeTe_6 is apparent.[19,20,25] This low thermal conductivity seems to be a common feature of the Agyrodite family of compounds.[59] Currently a basic understanding as to why Ag_8GeTe_6 and other Agyrodites possess such a low thermal conductivity, and more importantly, how Ag_8GeTe_6 thermodynamically evolves to allow for the rare co-existence of good thermoelectric performance and fast ionic conduction is conspicuously lacking. In this and the next chapter we will attempt to elucidate the nature of this unusually low thermal conductivity in light of the charge, spin, orbital and lattice degrees of freedom and their interplay. To this end, we performed specific heat (C_p) measurements between 1.8 K and 500 K and later thermal conductivity measurements (κ) between 10 K and 400 K on Ag_8GeTe_6.

At this point we must stress that the results of structural and thermal measurements we performed on Ag_8GeTe_6 are the most trustable among all datasets. As discussed in the earlier chapters on the structural and electrical properties of Ag_8GeTe_6, our samples contain a trace amount of secondary phase (~ 1 vol.% Ag_5Te_3 or $Ag_{10}Te_7$ as estimated from the Rietveld refinement of synchrotron X-ray power diffraction data). In crystal growth, a slow cooling rate (on the order of 1 K/hr) is found to be beneficial to obtain large solid ingots for electrical and thermal transport measurements, however, it also tends to promote the formation of the secondary phase. The secondary phase is hard to completely remove as it adheres to the *incongruent* melting of Ag-Ge-Te in crystal growth as discussed in **Chapter 2**. Moreover though the secondary phase is of trace amount, we must take extra caution since Ag_8GeTe_6 is a low carrier concentration system

whereas the secondary phase is comparably rich in charge carriers.[60] As such, the electrical transport properties of the as-grown samples are susceptible to the presence of the secondary phase. This explains the rather scattered electrical resistivity and thermopower data, presented in **Chapter 4**, although our lab-based X-ray diffraction measurements detected *no* secondary phase. In contrast, the results of heat capacity and thermal conductivity measurements, which will be presented in this chapter, have shown a satisfactory convergence within the instrumental uncertainty. The lack of practical lab-based technical tools has prevented us from timely and non-destructively investigating the amount, morphology, and topology of the secondary phase. For this reason up to this point the only strong evidence we have on the nature of the secondary phase is from high-resolution synchrotron X-ray powder diffraction which is expensive and has a very long turnaround time.

In order to manage these sample preparation issues while facilitating the much needed fundamental understanding of Ag_8GeTe_6 within the two year time span for my thesis, we have adopted two *rules of thumb*, in the case of inconsistent or contradictory data: (*i*) the structural and thermal data are more trustable than their electrical counterpart, and (*ii*) the data sets that are volumetric in nature are more trustable than those that are percolative in nature. These rules of thumb also reflect the fact that prior to our studies little was known about this material and some of the published data turned out to be incorrect. One of the most curious aspects of the previous thermoelectric studies on Ag_8GeTe_6 is the extreme dependence of the total thermal conductivity on the self doping ratio as described by Zhu *et al.* **Figure 5.1** shows the total thermal conductivity of self-

doped Ag_8GeTe_6 as a function of doping ratio. Surprisingly the authors report a nearly 40% change in thermal conductivity by varying the silver content by less than 0.5%. This change is too large to be physical when you consider that the carrier contribution to the thermal conductivity is negligible. As such, we deliberately use the colloquial wording "trustable" rather than "intrinsic" at this point. Toward the end of this thesis, we will have enough confidence to call several of our results "intrinsic".

5.2 Previous Work

In the one of the few early studies on the physical properties of Ag_8GeTe_6 below room temperature, Kawaji and Atake measured the specific heat of Ag_8GeTe_6 between 10K and 310K using a high precision *adiabatic* calorimeter, and showed that the lattice dynamics of Ag_8GeTe_6 are interesting in their own right.[37] As can be seen in **Figure 2** the specific heat of Ag_8GeTe_6 shows four anomalies between 150K and 250K, and near room temperature is nearly 30 J/mol*K above the classical Dulong-Petit limit. Additionally the specific heat displays a rare negative slope between 250K and 300K. With little in the way of supporting information the authors argued that all four phase transitions are first order and attributed the negative slope to an *unspecified* two-level system.

5.3 Experimental Details

In order to verify and further understand the rich thermodynamic features in Kwaji and Atake's report, low temperature specific heat was measured on a Quantum Design PPMS between 1.8K and 215K using the thermal relaxation method,[61,62] and between 130K and 260K by Dr. Joe Brill's group at the University of Kentucky using a high precision Differential Scanning Calorimeter (DSC). Throughout the temperature range the data sets are in good agreement, as shown in **Figure 5.2.** It should be mentioned that we attempted to push the PPMS measurement to higher temperatures, but due to poor thermal coupling between the sample and the stage the data proved to be unreliable, which hints that the thermal conductivity of this material is indeed low. Additionally as shown in **Figure 5.3** the specific heat was measured between 130K and 215K on both the DSC and PPMS. Other than in the regions of the phase transitions at 156K and 169K (discussed in the next section) the data is in very good agreement though the principle of measurement is subtly different: the DSC is a dynamic measurement[63] while the PPMS uses a steady state thermal relaxation type measurement. Ideally both a DSC and a PPMS measurement probe the same thermodynamics, however due to differences in the way data is obtained different systems are better for different purposes. First off as discussed in the next section the PPMS does very poorly when tracking multiple phase transitions within a narrow temperature range, which happens to be the case in Ag_8GeTe_6. Second, PPMS measurements are time consuming when compared to a DSC as it requires temperature stabilization at each data point. Third, thermal relaxation

measurements on a PPMS are prone to radiation losses at elevated temperatures, which is magnified in samples with low thermal conductivity and/or poor thermal coupling with the sample holder. On the other hand, DSC measurements excel in all three of the above aspects but are very difficult to conduct at low temperatures (< 10K).

Furthermore the specific heat of Ag_8GeTe_6 was measured between 50° C (323 K) and 600°C (873 K), using a Netzsch DSC 404 Pegasus in Dr. Tritt's lab at Clemson University. As can be seen in the **Figure 5.4** the data is in excellent agreement and even shows three more phase transitions above room temperature,[1] maintaining the overall negative temperature dependence, and 30 J/mol*K excess above the classical Dulong-Petit limit. The excellent agreement between the measurement results from three *separate* measurements enables a coherent understanding of the underlying thermodynamics in Ag_8GeTe_6 over such a wide temperature range for the first time.

5.4 Phase Transitions

As mentioned above Ag_8GeTe_6 undergoes *seven* phase transitions between 150K and 750K (156K, 170K, 223K, 245K, 527K, 629K, and 724K). This is an amazing number indicating that the material is thermodynamically *unstable*. Since we have previously ruled out any long range magnetic ordering in Ag_8GeTe_6 **(Chapter 3.)**, these thermodynamic anomalies must be associated with the charge (electrons and ions), lattice, and orbital degrees of freedom, as well as the interplay between them. The

[1] The reader should note that though these phase transitions are novel and have not been previously studied, they are beyond the scope of this thesis.

entropies and enthalpies of the phase transitions (calculated for both the new and old data) are shown in **Table 5.1**. Kawaji and Atake suggested that due to the shape of their DSC signatures all four of the phase transitions below room temperature are first order without further discussing their origin. As discussed in **Chapter 3** temperature dependent powder x-ray diffraction has confirmed that the transition at 223K and most likely the transition at 245 K both correspond to crystal symmetry changes confirming their first order nature. The low temperature transitions at 156 K and 170 K, however, have proven much more difficult to categorize. Indeed our PPMS measurements, preliminary DSC measurements, and even an early paper by Katty *et al.* missed the first transition at 156 K likely due to its small magnitude.[27] The small magnitude and lack of signature in x-ray data suggest that the transitions at 156K and 170K are not structural in nature or only involved with subtle structural changes (e.g., the onset of silver ordering). Additionally though the PPMS measurements were able to pick up the transition at 170 K the shape of the peak does not appear to be physical which can be attributed to systematic errors. J. C. Lashley *et al.* have published an excellent review of the thermal relaxation method (used in the PPMS) and argue that though it is possible to confirm the existence second order phase transitions it is impossible to accurately determine their shape or even confirm the existence of first order phase transitions using the PPMS.[64]

At this point it would seem obvious that other data sets could be used to confirm the nature of the transitions. The message from the DC resistivity regarding the transition at 170 K, however, is mixed: the lack of a well defined hysteresis loop accompanying the phase transition at 170K suggests it is a second order or continuous phase transition, on

the other hand, the abrupt jump near 170 K constitutes a discontinuity which is often seen in a first order phase transition. So far, no conclusion has been drawn on the 170 K phase transition. In this vein the appearance of an obvious hysteresis loop in the DC resistivity accompanying the phase transition at 156K along with the lack of signature in the PPMS C_p measurement are consistent with a first order phase transition. Ideally the signatures of the higher temperature transitions (223K and 245K) in the DC electrical resistivity could be used to clarify their order. Unfortunately the DC resistivity appears to show a hysteresis around these transitions, but the loop never closes making it difficult to describe. As discussed in **Chapter 4** the thermopower shows band noise above 245 K, the AC impedance detects a non-resistive signal above room temperature, and Ag_8GeTe_6 develops into a fast ionic conductor above room temperature. All these evidences suggest that the phase transition at 245 K corresponds to the onset of super-ionic conduction. If this is the case, Ag^+ ion migration is expected, and because the ionic kinetics have a much longer time constant than their electronic counterpart a hysteresis without closed loop can be explained. More discussion on the super-ionic phase transition at 245 K will be given when we address the peculiar line shape of the heat capacity anomaly at 245 K and the sustaining negative slope above 245 K.

Above room temperature the transition that appears to begin around 900K can be attributed to the onset of the peritectic decomposition of Ag_8GeTe_6.[28] Unfortunately the nature of the remaining transitions above room temperature (527K, 629K, and 724K) is less clear, due to a lack of supporting information. The presence of so many phase transitions in such a broad range of temperatures further supports both the observation

that Ag_8GeTe_6 is extremely unstable and the existence of a competition between many "nearly degenerate" states. In fact a large amount of current research in the field of thermoelectrics is focused on the study of improved thermoelectric performance near phase transitions, which as discussed in the introduction (**Chapter 1**), can lead to a destabilization of the charge degree of freedom due to the coupling between charge and lattice degrees of freedom and therefore enhance *ZT*.[65]

5.5 Basics of Specific Heat

Before beginning to quantitatively analyze the specific heat of Ag_8GeTe_6 it is instructive to review several of the basic concepts and models used to describe the way in which heat is "stored" in solid materials.

5.5.1 Dulong-Petit Limit

The Law of Dulong and Petit, also known as the Dulong-Petit limit, is a thermodynamic rule, published in 1819, that describes the molar heat capacity of a crystalline material.[66] Dulong and Petit were able to formulate their rule by noticing that if it was first multiplied by the atomic weight of the constituent atoms the mass specific heat of many materials approached a constant value at sufficiently high temperatures (now known to be $\sim\theta_D$ the Debye temperature, which will be discussed in the following section). They found that the molar specific heat was about 25J/K-mol. Knowledge of modern thermodynamics allows us to justify Dulong and Petit's expression in terms of

either the gas constant R and the molar mass of the material M or the number of atoms per mole N and the Boltzmann constant k_B.

$$C_v \simeq 3R/M = 3Nk_B \quad (4.1)$$

It should be noted that the Dulong-Petit limit is related to the constant volume specific heat C_v, *not* the constant pressure specific heat C_p. In general, C_v is more intuitive for theoretical considerations while C_p is experimentally accessible. The difference between C_v and C_p leads to an important discussion on anharmonicity and quasi-harmonicity in **Section 5.6**.

The introduction of Einstein's model of specific heat in 1907 offered a concrete microscopic explanation of the physical origins of the Dulong-Petit limit.[67] Using three simple observations Einstein was able to describe the physical origins of the Dulong-Petit limit: First he treated the atoms in a crystal as individual quantum harmonic oscillators, next he observed that according to the equi-partition theorem quadratic degrees of freedom can each store $1/2k_BT$ of energy, and finally he noted that each atom in a crystal has *6* degrees of freedom (one vibrational and one translational degree of freedom for each spatial dimension). Hence the energy stored in a crystal, at sufficiently high temperatures, should be equal to $C = (3+3)*N*1/2 k_BT = 3k_BT = 3R/M$.

The expression for specific heat of a crystal at low temperatures in the Einstein model is slightly more complicated and invokes quantum mechanics. As mentioned above in the Einstein model a solid material is described as a collection of quantum harmonic oscillators vibrating with the same frequency. Recalling the formula for the average energy of a quantum harmonic oscillator and remembering that there are N atoms

in the lattice which each have 3 degrees of freedom (3N total oscillators) allows us to express the average energy per mole of the Einstein lattice as

$$\langle U \rangle = 3N_A h\omega \left(\frac{1}{2} + \frac{1}{\exp(\beta\hbar\omega - 1} \right) \tag{4.2}$$

Next we recall the definition of heat capacity at constant volume

$$C_v = \left(\frac{\partial U}{\partial T} \right)_v = 3N \left(\frac{\partial U}{\partial \beta} \right)_v \frac{\partial \beta}{\partial T} = 3Nk_B \frac{x^2 e^x}{\left(e^x - 1 \right)^2} \tag{4.3}$$

where $x = \hbar\omega / k_B T$. Finally we define the Einstein temperature of the material as $\theta_E = \frac{\hbar\omega_E}{k_B}$ which allows us to write the expression for the specific heat of an Einstein lattice in its final form

$$C_{Einstein}(T) = 2N_A k_B \left(\frac{\theta_E}{T} \right)^2 \frac{e^{\theta_E / T}}{\left(e^{\theta_E / T} - 1 \right)^2} \tag{4.4}$$

5.5.2 Debye vs. Einstein Model

Discussed above was Einstein's model to describe the specific heat of a solid. A second, more realistic, model was developed by Peter Debye in 1912.[68] As we know, Einstein's model works well at high temperature where it approaches the classical Dulong-Petit limit; however at low temperatures it predicts an exponential temperature dependence, which contradicted experimental observations of a T^3 temperature dependence. To solve the problem of the low temperature dependence Debye developed a model in which the atomic vibrations of a material are modeled as phonons inside a box. In this way the specific heat of a given material can be calculated using the equation

$$C_{Debye}(T) = 9N_A k_B \left(\frac{T}{\theta_D} \right)^3 \int_0^{\theta_D / T} dx \frac{x^4 e^x}{(e^x - 1)^2} \tag{4.5}$$

where θ_D is the Debye temperature given by $\theta_D = \frac{h\omega_D}{k_B}$ and ω_D is the Debye frequency given by the equation $\omega_D = \left(\frac{3N}{4\pi V}\right)^{1/3} v_s$ where *N/V* is the number density of atoms and v_s is the speed of sound in the material. Like Einstein's model the Debye model recovers the Dulong-Petit limit at high temperatures ($T >> \theta_D$). At low temperatures ($T << \theta_D$) the Debye model follows the equation

$$C_V \sim \frac{12\pi^4 N k_B}{5}\left(\frac{T}{\theta_D}\right)^3 = \beta T^3 \qquad (4.6)$$

which unlike the Einstein model displays a T^3 temperature dependence in agreement with experiment. This is because the Debye model predicts the exact phonon dispersion at temperatures low enough that only long wavelength acoustic modes are activated. In between the high and low temperature regimes the Debye model is not as accurate due to limitations of the basic assumptions of used in its derivation, similar to the Einstein model.

5.5.3 Phonon Dispersion Relation

As mentioned earlier any excitation in a solid material can both store and transport heat. In many cases, however, (Ag_8GeTe_6 being one of them) the storage and conduction of heat is dominated by quantized lattice vibrations or phonons. With this in mind it is useful to consider the phonon dispersion relation when discussing any thermal phenomena in Ag_8GeTe_6.

The phonon dispersion relation of a crystalline material describes the frequency (ω) of the allowed phonon modes in the material as a function of their momentum (k). This problem can be simply solved with three simple assumptions: (*i*) first we must assume a harmonic periodic lattice, (*ii*) second only nearest neighbor interactions are considered, and (*iii*) finally Born-von Karman boundary conditions must be used.

A classic derivation of the phonon dispersion is given by Kittel. For simplicity the derivation is for an elastic wave propagating along a high symmetry direction ([100], [110], and [111]) of an infinite (*iii*) monatomic cubic crystal.[69] He begins by considering the displacement of planes of atoms rather than individual atoms, and then assumes that the forces between atoms can be described using Hooke's Law $\vec{F} = -k\vec{x}$ (*i*). From here the force on plane *s* displaced by *s*+*p* can be given by

$$\vec{F}_{sp} = -C_{sp}\left(u_s - u_p\right) \tag{4.7}$$

Next by considering only nearest neighbor interactions (*ii*) p is constrained to $p = \pm 1$ allowing the expression to be further simplified to

$$\vec{F}_s = C\left(u_{s+1} - u_s\right) + C\left(u_{s-1} - u_s\right) \tag{4.8}$$

At this point it is useful to consider C as the interatomic force constant rather than the interplane force constant in order to facilitate the description of a single atom in an atomic plane which can be given by the following equation:

$$M\frac{d^2u_n}{dt^2} = C\left[u_{n+1} - u_{n-1} - 2u_n\right] \tag{4.9}$$

where M is the mass of a single atom. Finally by assuming all displacements have the same time dependence (exp(-*iωt*)) **equation 5.9** becomes

$$-M\omega^2 u_n = C\left[u_{n+1} + u_{n-1} - 2u_n\right] \tag{4.10}$$

Solving the differential equation gives a traveling wave solution of the form

$$u_{s\pm1} = u\exp(\mathrm{isKa})\exp(\pm\mathrm{iKa}) \tag{4.11}$$

which can be simplified to obtain the phonon dispersion relation

$$\omega^2 = \left(4C/M\right)\sin^2 1/2\,Ka \tag{4.12}$$

Furthermore it is important to consider which values of will be physically significant. To this end basic solid state considerations tell us that all of the meaningful information in the phonon dispersion is contained in the first Brillouin zone hence *k* is restricted to $-\pi/a \le k \le \pi/a$. **Figure 5.5** shows the phonon dispersion of a monatomic crystal.

It is also informative to consider the slope of the phonon dispersion at the edge of the first Brillouin zone. To do this we must take the derivative equation. 5.12

$$d\omega^2/dk = \left(2Ca/M\right)\sin ka \tag{4.13}$$

clearly the derivative goes to zero at the zone boundary $k = \pm\dfrac{\pi}{a}$ hence it corresponds to a standing wave. Beyond the slope of the phonon dispersion it is also informative to consider the group velocity of waves described by the phonon dispersion relation. In this way the group velocity can be described by the following equation

$$v_g = \frac{d\omega}{dk} = grad_{\vec{k}}\left(\omega(\vec{\mathrm{k}})\right) \tag{4.14}$$

Substituting equation 5.12 into the above equation gives the group velocity

$$v_g = \left(\frac{Ca^2}{M}\right)^{1/2} \cos\left(\frac{ka}{2}\right) \tag{4.15}$$

which again corresponds to a standing wave at the zone boundary.

The preceding derivation is in most cases oversimplified. When a material contains two or more atoms per primitive cell the situation is more complex. In this case the phonon dispersion will still have three acoustic modes which correspond to in phase motion of entire unit cells as in a monatomic crystal, however there now be a number of optical modes, which correspond to the motion of atoms against each other inside the unit cell. The number modes of a given crystal structure is equal to *3N* where *N* is the number of atoms per unit cell, and these modes can be further broken down into 3 acoustic modes and (*3N-3*) optical modes. A complete derivation of the phonon dispersion relation of a material with more than one atom per unit cell is beyond the scope of this thesis however we will present the phonon dispersions for the optical and acoustic branches of a diatomic crystal. In the limit of small k the dispersions are given by the following equations

$$\omega^2 \simeq 2C\left(\frac{1}{M_1} + \frac{1}{M_2}\right) \tag{4.16}$$

$$\omega^2 \cong \frac{1/2\,C}{M_1 + M_2} k^2 a^2 \tag{4.17}$$

where M_1 and M_2 correspond to the atomic masses. Equation (5.16) corresponds to the optical branch and Equation (5.17) corresponds to the acoustic branch. At the other extreme in the limit of $ka = \pm\pi$ the dispersion can be given by

$$\omega^2 = 2C / M_1 \tag{4.18}$$

And

$$\omega^2 = 2C / M_2 \quad (4.19)$$

The phonon dispersion of a diatomic crystal is shown in **Figure 5.6**. The same equation for the group velocity of acoustic modes (**Equation 5.15**) applies to the optical modes in a crystal. As can be seen in **Figure 5.6**, however, the optical modes have a much smaller slope than the acoustic modes and therefore have a smaller group velocity. In this way it is possible to understand the adage that "all phonon modes store heat but not all modes carry heat." Due to their low group velocity optical phonon modes contribute very little to thermal conductivity (in most cases). In the case of materials with many atoms per unit cell there will obviously be many more optical modes than acoustic modes, and in some cases the optical modes have energy at or below the maximum energy of the acoustic branches.

The phonon dispersion relation in materials like Ag_8GeTe_6 that display strong anharmonicity is more complicated that the preceding discussion. Indeed one of the initial assumptions was that the potential is purely harmonic. In reality no material is purely harmonic therefore the lines in the dispersion relation would more accurately be replaced by "bands" whose width increased with increasing anharmonicity.

5.5.4 Charge carrier contribution to specific heat C_v

Until now the discussion of the storage of heat in a solid material (specific heat) has been focused solely on the crystal lattice. In real crystals however heat can also be stored by be stored other types of excitations including (but not only) free carriers and spin waves (spinons).[70] The contributions to specific heat by excitations beyond free

carrier and phonons are considered to be beyond the scope of this thesis. To calculate the contribution of free carriers to the specific heat we begin with the following expression for the internal energy of a Fermi sea of electrons (holes)

$$U = \int_0^\infty \varepsilon D(\varepsilon) f(\varepsilon) d\varepsilon = U_0 + \frac{\pi^2}{6}(k_B T)^2 D(\varepsilon_F) \tag{4.20}$$

where $D(\varepsilon)$ is the Density of States and $f(\varepsilon)$ is the Fermi-Dirac distribution. From here it is possible to calculate the carrier contribution to the specific heat in the low temperature limit using the equation:

$$C_v = \frac{\partial U}{\partial T} = \frac{\pi^2}{3} g\left(\varepsilon_F\right) k_B^2 T = \frac{\pi^2}{2} n k_B \left(\frac{k_B T}{\varepsilon_F}\right) = \gamma T \tag{4.21}$$

The contributions of different excitations to specific heat should be additive therefore the total specific heat of a solid material in the low temperature limit can be given by the equation

$$C_V = C_{V,carrier} + C_{V,Debye} = \gamma T + \beta T^3 \tag{4.22}$$

5.5.5 Schottky Anamoly

Undoubtedly the Einstein and Debye models are oversimplified when it comes to the specific heat of real materials. This oversimplification is particularly important to the discussion of Ag_8GeTe_6 because they ignore two important aspects of the specific aspects of many materials anomalies, such as Schottky anomalies and phase transitions, and anharmonicty.

A Schottky anomaly describes an anomalous contribution (peak) observed in the specific heat of a solid material due to the presence of discreet energy levels in the system. This is an example of a macroscopic signature of a microscopic quantum

phenomenon. In most cases Schottky anomalies appear at *low temperatures* ($T << \theta_D$) in systems with *two* (or more) discreet energy levels, which are generally due to the presence of dilute magnetic impurities in the system. In some rare cases Schottky type behavior can be observed at temperatures near room temperature.[71] In the most general case the energy of a multi level system can be describe by the equation:

$$E = \frac{N\sum \varepsilon_r g_r \exp\left(-\varepsilon_r / k_B T\right)}{\sum g_r \exp\left(-\varepsilon_r / k_B T\right)} \tag{4.23}$$

which leads to the following expression for the heat capacity of a two level system:

$$c_{Sch} = \frac{\partial E}{\partial T} = \frac{N\left(\varepsilon_1 - \varepsilon_0\right)^2}{k_B T^2}\frac{g_1}{g_0}\frac{\exp\left(-\varepsilon_1 / k_B T\right)\exp\left(-\varepsilon_0 / k_B T\right)}{\left[\frac{g_1}{g_0}\exp\left(-\varepsilon_1 / k_B T\right) + \exp\left(-\varepsilon_0 / k_B T\right)\right]^2} \tag{4.24}$$

in the usual case of a system with the lower level at the ground state ($\varepsilon_0=0$) at low temperature this simplifies to the well known equation for a Schottky system

$$c_{Sch} = \left(\frac{\Delta\varepsilon}{k_B T}\right)^2 e^{-\Delta\varepsilon/k_B T} \tag{4.25}$$

The most important point of the derivation is the presence of a negative slope in the specific heat as a function of temperature, which is very similar to the behavior of Ag_8GeTe_6 observed by Kawaji and Atake.

5.5.5 Anharmonicity

The above discussion of the specific heat of solid materials considers only harmonic interatomic potentials. This simplified approach works well in many instances,

however, isn't always sufficient when considering real condensed matter systems. In this case deviations from the simple harmonic crystal lattice are lumped into the category of anharmonicity. Indeed several basic physical processes can only be explained by anharmonicity including thermal expansion, the pressure/temperature dependence of elastic constants, and even phonon-phonon interactions.

5.6 Data Analysis

The following subsections will focus on the three most prominent anomalies in the specific heat, namely, (*i*) the excess C_p observed at low temperatures; (*ii*) the anharmonicity caused deviation from the Dulong-Petit limit; and (*iii*) the persistent negative slope starting from the right side of the specific heat peak at 245 K. The results will provide a clear picture on the lattice dynamics of Ag_8GeTe_6 and set up a stage to analyze the low thermal conductivity.

5.6.1 A Combined Debye-Einstein Model to Understand Feature (i)

As mentioned above the low temperature specific heat of a solid material can generally be fit using the Debye Model.

$$C_P = \gamma T + \beta T^3 \tag{4.26}$$

where γ is the Sommerfeld coefficient hence the γT term corresponds to the contribution to the specific heat from charge carriers, and the βT^3 term corresponds to the contribution from the crystal lattice described in **Section 5.2**. **Figure 5.7** shows the low temperature

specific heat of Ag_8GeTe_6 fit to the Debye model.[72] Though the fit initially looks good the values it gives for both γ and β are obviously questionable. First off the γ value is negative which is unphysical, while the β value of 0.029 J/mol*K^4 corresponds to a Debye temperature (θ_D) of nearly 1000K. The Debye temperature can be considered to be a rough estimate of the temperature at which all of the phonon modes in the system are populated, and hence the temperature where the specific heat saturates. A quick look at the C_p *v. T* plot tells us that the fit value for θ_D is obviously much too large. Recalling that the low temperature resistivity and magnetization of Ag_8GeTe_6 from the preceding chapters suggests the Sommerfeld Coefficient (γ) can be set to zero however, this still leads to unphysical values of β.

To understand the nature of the deviations from the Debye model it is useful remember the crystal structure of Ag_8GeTe_6. When considered in the context of two sublattices: one rigid GeTe sublattice and a second "liquid-like" Ag sublattice it suggests that one or more of the Ag^+ sites behave like Einstein oscillators rather than members of the collective Debye lattice. Following the procedure laid out in "Use of Atomic Displacement Parameters in Thermoelectric Materials Research" by Dr. Brian Sales *et al*. it is possible to model the crystal interactions using a combined Debye and Einstein lattice shown in the equation below, were f is the fraction of the atoms in the entire crystal lattice that act as part of the Debye lattice, C_{Debye} is the Debye specific heat, and $C_{Einstein}$ is the Einstein specific heat.[73]

$$C_V(T) = fC_{Debye}(T) + (1-f)C_{Einstein}(T) \tag{4.27}$$

In a physical sense this model treats the material as being made up of a traditional Debye lattice of tightly bonded atoms that is interspersed with loosely bound atoms whose motion is *not* coupled to the other atoms in the crystal, and therefore behave like harmonic oscillators. In some sense this model is still oversimplified, the Einstein oscillators are assumed to all vibrate with the same frequency, however it accurately describes the specific heat of many interesting materials. The most obvious example of this type of lattice is filled Skutterudites. The basic Skutterudite structure, shown in **Figure 5.8**, is featured by 2 voids, which can be filled to create *rattlers* or atoms that are only loosely bound to the crystal structure. These rattlers have proved to be very useful to thermoelectricians due to their ability to strongly and resonantly scatter phonons. The specific heat of these materials can be very accurately described using a combined Debye and Einstein lattice where the "rattlers" are treated as Einstein oscillators.[74,75]

Before beginning to model the lattice dynamics in Ag_8GeTe_6 using the procedure laid out in [73] it is important to point out that this procedure uses single crystal x-ray or powder neutron scattering data to completely model the specific heat of a material with <u>*no free parameters*</u> which is a very different procedure than the usual *fitting* used to obtain θ_D from C_p data. Additionally it should be noted that the crystallographic data that will be used in the model was taken at room temperature and above though the model is for low temperature C_p. This presents a problem because it is clear from both the experimental low temperature specific heat and low temperature x-ray data that the system undergoes at least one symmetry change between room temperature and the temperatures being modeled. For this reason it must be stressed that this model is not

presented to be rigorous but rather as one possible explanation of the low temperature lattice dynamics of Ag_8GeTe_6.

The first step in modeling the specific heat is to decide which site or sites to model as Einstein oscillators. To do this the atomic displacement parameters (ADPs) of the different crystallographic sites are compared. Clearly any atom which behaves like an Einstein oscillator will have a large atomic displacement parameter because of the fact that it is so loosely bound to the surrounding atoms, and according to [73] the rule of thumb is that any site that behaves like an Einstein oscillator should have an ADP that is three times larger than the other sites in the lattice. The APDs of the all of the sites in the Ag_8GeTe_6 lattice are given in **Table 5.2**.[21] It is clear that if there is a site in the Ag_8GeTe_6 lattice that behaves like an Einstein oscillator it is the Ag2 site. The next step is to calculate the Einstein and Debye temperatures using the equations below

$$Slope(U_{iso} vs. T) = 3h^2 / (mk_B \Theta_D 4\pi^2) \tag{4.28}$$

and

$$U_{iso} = k_B T / K = h^2 T / (4\pi^2 m k_B \Theta_E^2) \tag{4.29}$$

this gives values of 37K for θ_E and 176K for θ_D. In general it is best to use the slope of the ADP vs. Temperature plot to calculate θ_D and θ_E however, the magnitude of the ADP of the Ag2 site in Ag_8GeTe_6 decreases with increasing temperature due to changes in occupancy. This would lead to an imaginary value of θ_E, which isn't physical; therefore the room temperature ADP along with the assumption that the intercept of the ADP vs.

temperature plot is near zero has been used to calculate the slope of the low temperature *ADP vs. T* plot and hence θ_E. Once θ_D and θ_E have been calculated it is possible to calculate the Einstein and Debye contributions to the specific heat using **Equations 5.4 and 5.5**.

It is now possible to calculate the C_p of the material using **Equation 5.27** and the Einstein and Debye specific heats calculated above. We have also assumed that *f* the fraction of atoms that are part of the Debye lattice is 0.8 which should be equal to the total number of atoms per unit cell minus the number of atoms on the Ag2 site.

As can be seen in **Figure 5.9** the model is in very good agreement with the measured data at both low temperatures (below 10K) and also at high temperatures (above 150K). The deviation of the measured Cp from the model between 50K and 150K is expected because the basic assumptions of both the Debye and Einstein models are not valid in this intermediate temperature range, as discussed earlier in the chapter. Additionally as expected the model cannot explain the deviations from Dulong-Petit, which will be discussed in detail in **Section5.5.3**.

5.6.2 BOSON PEAK

Solids that contain Einstein modes in their phonon spectra generally display a peak in the plot of C_p/T_3 *v lnT*. This peak can be attributed to excess vibrational modes above the normal Debye contribution. In the most general sense this peak is called a Boson peak, and is a characteristic of amorphous solids. The physical origins of the Boson peak in amorphous materials are still currently a topic of much debate, though it is

generally accepted that they are the result anomalies in the phonon density of states usually described in terms of soft structures.[76] Interestingly some authors attribute the appearance of a Boson peak to disordered systems that are *nearly* unstable.[77] In most cases amorphous materials that display a Boson peak in C_p also have a peak in the low temperature thermal conductivity versus temperature plot. Moreover the existence of a Boson peak in glasslike materials has signatures in Neutron and Raman scattering experiments.[78,79] In cases similar to Ag_8GeTe_6 where the nature of the peak is confirmed it is usually referred to as an Einstein peak.

A plot of C_p/T^3 *v lnT* for Ag_8GeTe_6 along with the combined Debye and Einstein model is shown in **Figure 5.10a**. As expected the plot shows a peak centered around 5-6K, which supports the existence of Einstein modes in the lattice. The peak in the model, however, occurs at a slightly higher temperature, approximately 8K, and displays the wrong shape; its *FWHM* is about half as large as it should be. This suggests that the combined Debye+Einstein fit is too simple, and that the lattice would be better described by two Einstein oscillators/modes inside a Debye host.

Figure 5.10b shows a modified fit of the low temperature specific heat data. To obtain the displayed curve the Einstein peak (C_p/T^3 *v. lnT* below 20K) was fit to a combined Debye and Einstein lattice with 2 different Einstein modes using six free parameters: the Einstein and Debye temperatures (θ_{E1}, θ_{E2}, and θ_D) and the fractions of the atomic lattice contributing to each term in the fit (f_{E1}, f_{E2}, and f_D). Both in terms of peak position and peak width the fit containing two Einstein modes is much better than the initial model containing a single Einstein mode. Of particular interest are the values

of the Einstein and Debye (θ_{E1}, θ_{E2}, and θ_D) temperatures from the new fit. The new values for θ_{E1}, θ_{E2}, and θ_D are 16 K, 36 K, and 165 K respectively, which is surprisingly close to the values obtained from the previously described model, of 37K and 176K. When coupled to the Debye temperature of 175 K obtained from the speed of sound

$$v_s = \frac{\theta_D k_B}{\hbar}\left(\frac{6\pi^2 N}{V}\right)^{-1/3} \tag{4.30}$$

(1701 m/s) measured by Charoenphakdee et al.**Error! Bookmark not defined.** the similarity of the values of θ_E and θ_D obtained by such different methods strongly supports their validity.

Furthermore the fact that the Debye temperatures obtained by measurements above (velocity of sound) and below (low temperature specific heat) the four low temperature phase transitions are very similar suggests that the phase transitions involve very little vibrational entropy. In "Vibrational Thermodynamics of Materials" Fultz gives the following equation to estimate the vibrational entropy change involved with a particular phase transition: $\Delta S^{\alpha\to\beta} = 3k_B \ln\left(\theta_{D\alpha}/\theta_{D\beta}\right)$ where $\theta_{D\alpha}$ is the Debye Temperature of phase α, and $\theta_{D\beta}$ is the Debye temperature of phase β.[80] This observation strongly supports the observation that the low temperature phase transitions mainly involve ordering of the silver sublattice which is discussed in detail later in this chapter.

The existence of the Einstein peak in the low temperature confirms the existence of low energy optical modes in the crystal structure though the nature of these modes is less clear. Initially presented in the context of "rattlers" similar to those in Clathrates or Skutterudites, further structural considerations, however, suggest that there are no voids

or cages in the crystal structure to house this type of atom. This still leaves two possibilities for the nature of the Einstein peak first it is still possible that the Ag^+ ions act as “rattlers” in a tunnel-like structure formed by the ionic diffusion path (discussed in Chapter 3), or conversely the excess Cp could simply be attributed to low laying optical phonon modes. This second case can be understood in the context of the phonon density of states (**Section 5.5.3**). In this way optical phonon modes with low enough energy will be populated at low temperatures adding to the specific heat predicted by the Debye model, which assumes only long wavelength acoustic phonon modes at temperatures << θ_D. This is of a very valuable observation in to context of Ag_8GeTe_6 because the existence of low lying optical modes offers several paths to explain the unusually low thermal conductivity discussed in detail in the following chapter.

5.6.3 Anharmonicity and Gruneissen parameter

As discussed in **Section 5.5.1** the Debye and Einstein models cannot explain the observed deviations from the Dulong-Petit limit. At their core the Debye and Einstein models assume a harmonic potential for the atoms that make up the crystal lattice and therefore ignore any anharmonic interactions, which would cause an increase in specific heat because they offer another place to store themal energy in the material. This suggests that the excess C_p above the Dulong-Petit limit (**Figure 5.4**) may be at least partially attributed to anharmonicity.

In the case of Ag_8GeTe_6 the large anharmonicity leads to strong phonon-phonon interactions, and is therefore at least partially responsible for the unusually low lattice

thermal conductivity discussed in **Chapter 6.** For this reason it is crucial to address anharmonicity and furthermore to derive the important Gruneissen parameter in the context of general thermodynamics.

The Gruneissen Parameter of a given phonon mode (*i*) defined as:[81]

$$\gamma_i = -\frac{\partial \ln(\omega_i)}{\partial \ln(V)} \tag{4.31}$$

offers a way to quantify the "strength" of its anharmonicity, and can be calculated from pressure dependent neutron or x-ray scattering. Furthermore the mode averaged Gruneissen parameter describes the anharmonicity of the bulk of a material. With this in mind we calculated the room temperature mode averaged Gruneissin parameter of Ag_8GeTe_6 using the equation:[82]

$$\gamma_G = \frac{3\alpha_{vol.} B_T V_0}{C_P} \tag{4.32}$$

where α_{vol} is the volumetric thermal expansion coefficient, calculated from temperature dependent x-ray diffraction measurements and taken to be 1.2×10^{-4} K^{-1}, B_T is the bulk modulus calculated from the measured v_S of 1723 m/s and taken to be 2.14×10^{10} Kg/ms^2, V_0 is the molar volume taken to be 2.36×10^{-4} m^3/mol, and C_P is the specific heat (at 300K) measured using taken to be 442 J/mol*K. Substitution of these values into the equation gives a value of 3.8 for the Gruneissen parameter.

As a rule of thumb the Gruneissen parameter of most materials has a value between one and two. Materials with a Gruneissen parameter as high as three or four are quite rare and signify a class of "frustrated" materials in which the lattice is not complete stable. In some cases it is possible for the Gruneissen parameter is a specific phonon

mode to have a value as high as seven or so but this only occurs in very specific bands that normally correspond to highly disordered crystallographic directions. Indeed there are no materials with reported mode averaged Gruneissen parameters higher than 3.7.[81]81,[83,84] The effects of anharmonicity and the concomitant changes in interatomic spacing can be described by the following equation

$$6\gamma = -\frac{r}{k_s}\frac{\partial k_s}{\partial r} \tag{4.33}$$

where r is the interatomic distance and k_s is the interatomic force constant. From **Equation 5.33** it is clear that slight changes in interatomic distance (+1%) can lead to very large changes in interatomic forces(–12%). Even more suprising is that observation that a change in interatomic distance of +10% could cause the interatomic force to disappear entirely.[80]

5.6.4 Quasi-Harmonic Model

At least a portion of the deviation of the measured C_p from the combined Debye and Einstein model above 125K can be explained by the fact that the measured specific heat is at constant pressure (C_p) though the model is from specific heat at constant volume (C_v). For this reason there measured value should always be larger than the values given by the model because it involves not only heat stored in the lattice but also the energy needed cause the lattice to expand through thermal expansion. It is customary to assume that the difference between C_v, which plays a significant role in theoretical thermodynamics, and C_p, which is experimentally easy to assess, is only a few percent. In the case of Ag_8GeTe_6, however, the key to understanding why the thermal conductivity is

so low partially lies in this few percent difference. At least a portion of deviation can be well understood in the context of the Quasi Harmonic (QH) model, which offers a valuable tool for understanding aharmonicity, at least to the first order.

The QH model is very similar to the Debye or Einstein models in that it describes a solid material as a collection of harmonic oscillators. However in the QH model the spring constant of the oscillators is allowed to change with temperature. In this way the quasi-harmonic model is able to extend the harmonic Debye and Einstein models to include a very specific type of anharmonicity. By allowing the spring constants of the harmonic oscillators to change with increasing temperature the quasi-harmonic allows for the introduction of phonons with different frequency and leads to the inclusion of thermal expansion in the definition of the specific heat, which effectively changes the Debye and Einstein models of specific heat at constant volume (C_v) to specific heat at constant pressure (C_P). Moreover by modeling the specific heat of a material using the quasi-harmonic model it is possible to roughly estimate the amount of anharmonicity in the crystal *beyond* simple thermal expansion (anywhere the measured C_p is larger than the value of the "Harmonic+QH" model), which is particularly useful to thermoelectricians because this anharmonicity is usually effective at lowering thermal conductivity through a reduction of phonon lifetime.

Fig 5.11 shows the measured C_p along with two models. The first model discussed assumes only harmonic crystal interactions in the form of a Debye host lattice with Einstein oscillators while the second model has an additional contribution from a QH term. After the addition of the QH term the fit is quite good up to the phase transition

at 223K. This suggests that though the anharmonicity in Ag_8GeTe_6 is quite large it can be explained in the context of thermal expansion. Above the transition at 223 however the deviations from the Dulong-Petit limit are much larger and cannot be well explained in the context of the QH model.

5.6.5 Negative Slope of the Specific Heat

At this point we are ready to discuss third question posed by our data: "(iii) the persistent negative slope starting from the right side of the specific heat peak at 245 K". The key to understanding this peculiar feature lies in the shape of C_p anomaly at 245 K. As shown in Figure xx the anomaly at 245 K can be decomposed into a 1st order and a 2nd order phase transition.

Between 250K and 800K the overall trend in the C_p *v. T* plot is negative, which goes against the basic rule that with the exception of the backside of a phase transition C_p should always increase with increasing temperature. In their paper Kawaji and Atake have attributed the negative slope between 250K and 350 K to the existence of a two level system though they do not further address its nature. Indeed one our first reasons for studying Ag_8GeTe_6 was the existence of this negative slope, as it is possibly due to the charge Kondo effect, which we initially assumed to could be due to differing Ge charge states (Ge^{2+} and Ge^{4+}, which importantly both correspond to full shell states) as a result of Silver deficiency in the crystal structure.[85] Furthermore **Figure 5.12** shows the measured C_P plotted along with a curve: $C = C(Dulong - Petit) + const./T^2$, which is what one would expect from a Schottky anomaly, for k_BT>>splitting of a 2 level system.

The temperature dependence of the negative slope is similar to what would be expected for a traditional Schottky anomaly (as discussed in **Section 5.5** above) though the energy scale is much too large: the coefficient of the $1/T^2$ term would imply an energy splitting of ~ 80 meV (i.e. > k_BT), assuming there is only one excitation/formula unit. With that in mind if the negative slope is to be attributed to a Schottky anomaly there must be several excitations/formula unit. Beyond the magnitude of the *Cp* anomaly the shape is inconsistent with what would be expected for a Schottk anomaly. The low temperature side of a Schottky anomaly should show a Gaussian shape, but fitting the data show the low temperature side of the peak is far too steep to be Guassian. Additionally the width/height of the peak is inconsistent with what one would expect for a Schottky anomaly, in order to properly fit the width of the observed fit to a Schottky type peak the height of the peak is three to four orders of magnitude too large. Currently the existence of the charge Kondo effect cannot be conclusively ruled out, however, evidence for its existence is on shaky ground therefore further discussion can be found in **Chapter 7: Future Work**.

A more compelling explanation for the negative temperature dependence of Cp lies in the super ionic nature of Ag_8GeTe_6. Recent studies on the interplay between super ionic conduction and high performance thermoelectricity have attributed similar behavior of specific heat to a "premelting" phenomenon.[86] The onset of this phenomenon is clear upon closer inspection of the specific heat in the region of the phase transition at 245K (**Figure 5.13**). In this case the nature of the peak is revealed when it is broken into parts: first there is a contribution from a first order structural transition which accounts for the

large latent heat present after the transition the second contribution is a second order "Lambda" transition which causes the large peak in the C_p and can be explained by a partial "melting" of the Ag+ sublattice. Similar behavior has also been observed in nanoclusters of metal atoms.[87]

Furthermore in the case of super ionic conductors authors have recently argued that the onset premelting and the super ionic phase fundamentally changes the way in which heat is stored in the crystal. This change can be well described in the context of waves inside of a periodic lattice versus waves in a liquid. As discussed in (Dulong Petit Section) the specific heat of a periodic crystalline lattice is given by $C = (3+3)*N*\frac{1}{2}k_BT = 3k_BT = 3R/M$ where (*3+3*) term describes the three vibrational and three translational degree degrees *f* freedom of each atom. In a liquid however transverse acoustic modes cannot propagate therefore effectively eliminating any transverse vibrational modes in which case the specific is more accurately given by the equation $C = (3+1)*N*\frac{1}{2}k_BT = 2Nk_BT = 2R/M.$ After the onset of premelting only a portion of the atomic lattice of a super ionic conductor becomes "liquid" (the conducting species) therefore the specific heat of a superionic conductor should fall somewhere in between the value for a traditional solid and the value for a liquid $2Nk_B < C_V < 3Nk_B$

5.7 Conclusions

The lattice of Ag_8GeTe_6 is extremely unstable, which sets the stage for the unusually low thermal conductivity of Ag_8GeTe_6, discussed in detail in the following chapter. We have argued that the instability is a consequence of three factors and the interplay between them: First the strong anharmonicity as evidenced by the large Gruneissen parameter, second the existence of low lying optical phonon modes as evidenced by the Einstein peak in the C_p/T^3 *v. ln T* plot, and finally the onset of premelting alter the final low temperature phase transition at 245K.

Site	Ag1	Ag2	Ag3	Ge	Te1	Te2	Te3
ADP at 293K	.1128	.1470	.0545	.0142	.0224	.068	.062
ADP at 400K	.1103	.1014	.0761	.018	.0297	.069	.059

Table 5.1 Atomic displacement parameters of the different sites in the Ag_8GeTe_6 lattice. *Source Ref. [21]*

Transition Temperature (K)	Enthalpy ΔH (J/mol)	Entropy ΔS (J/K*mol)
156.1	90	0.58
169.9	194	1.14
222.9	2560	11.5
244.7	1910	7.83
557	879	1.59
629	2261	3.57
724	3931	5.40

Table 5.2: Temperatures, enthalpies and entropies of the phase transtions of Ag_8GeTe_6.

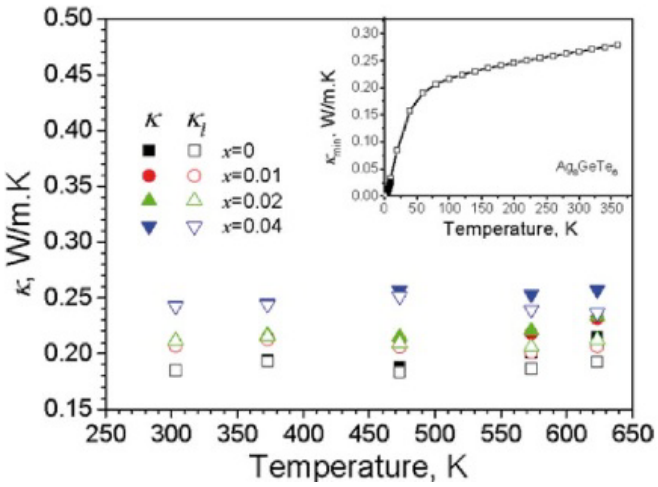

Figure 5.1:. Thermal conductivity of "self-doped" Ag_8GeTe_6 *Source Ref. [20]*

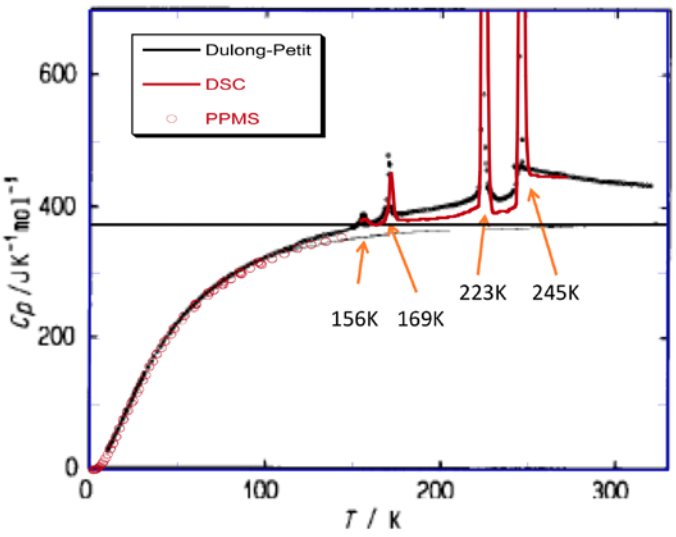

Figure 5.2: Heat capacity of Ag_8GeTe_6 measured using a precision DSC and a Quantum Design PPMS overlaid on data previously published by Kawaji and Atake (our data is in excelent agreement with the literature). *Source Ref. [37]*

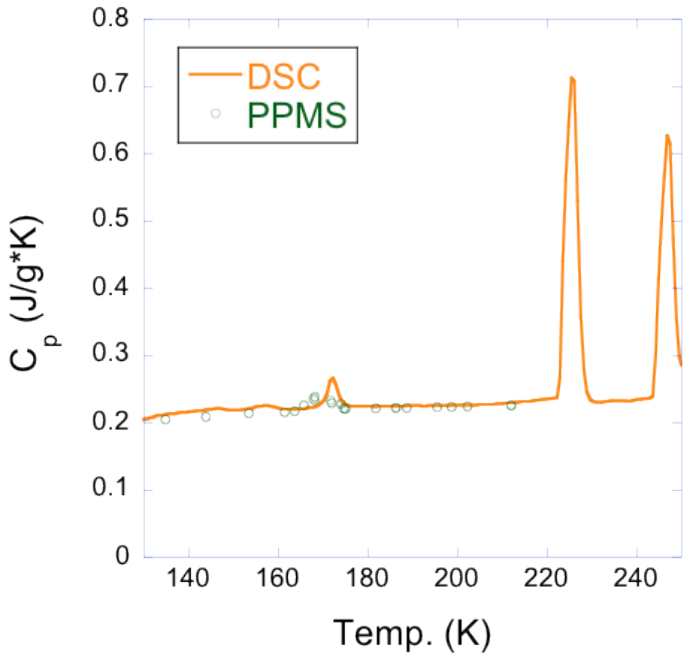

Figure 5.3: The measurements of the specific heat of Ag_8GeTe_6 using a precision DSC and the PPMS are in very good agreement.

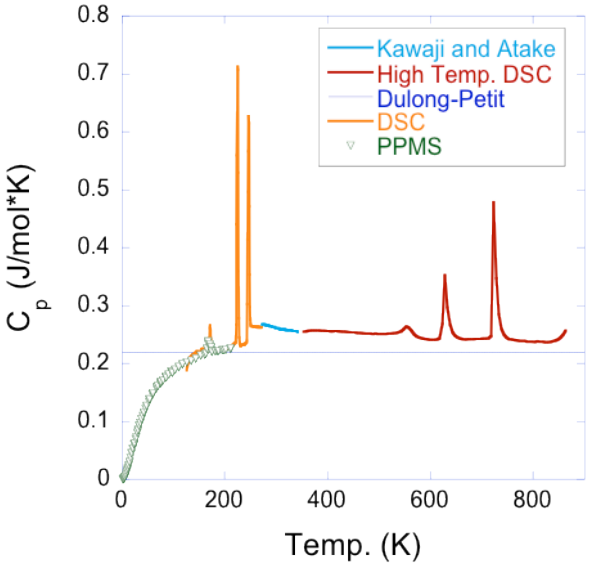

Figure 5.4: Specific heat of Ag_8GeTe_6 from 2K to 875K measured using four different systems (the data is in excellent agreement).

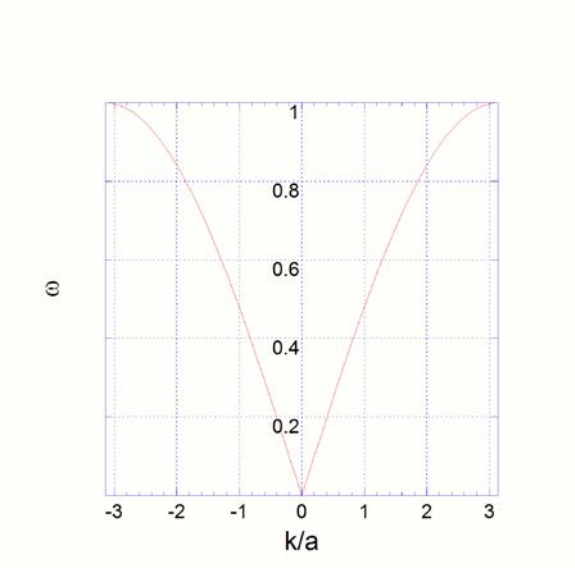

Figure 5.5: Phonon dispersion of a monatomic crystal.

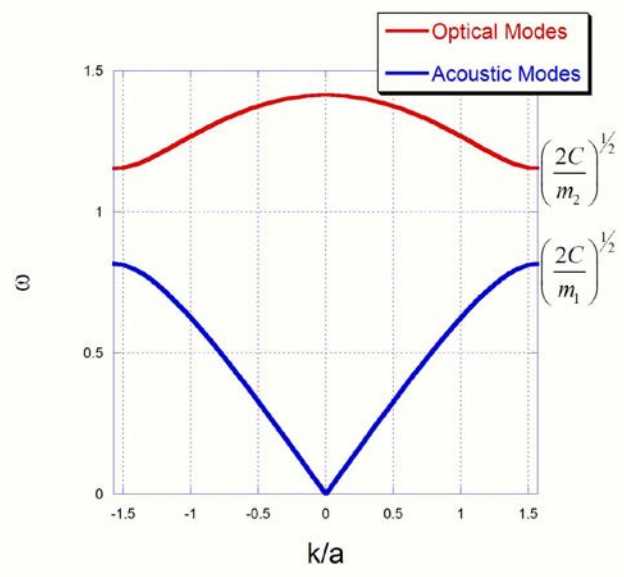

Figure 5.6: Phonon dispersion of a diatomic crystal.

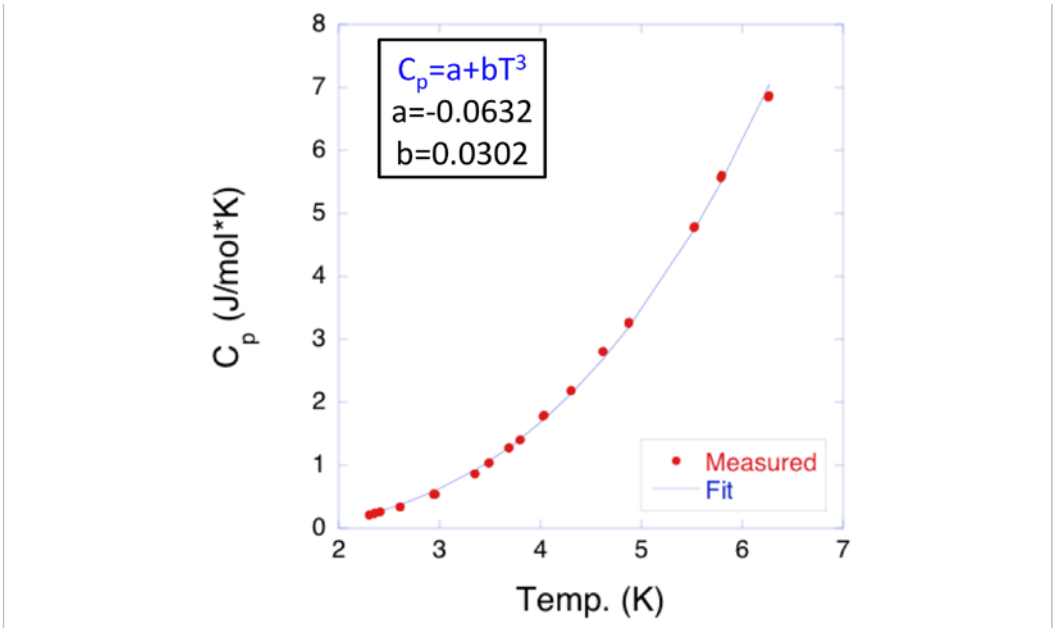

Figure 5.7: Low temperature specific heat of Ag_8GeTe_6 fit to the Debye model.

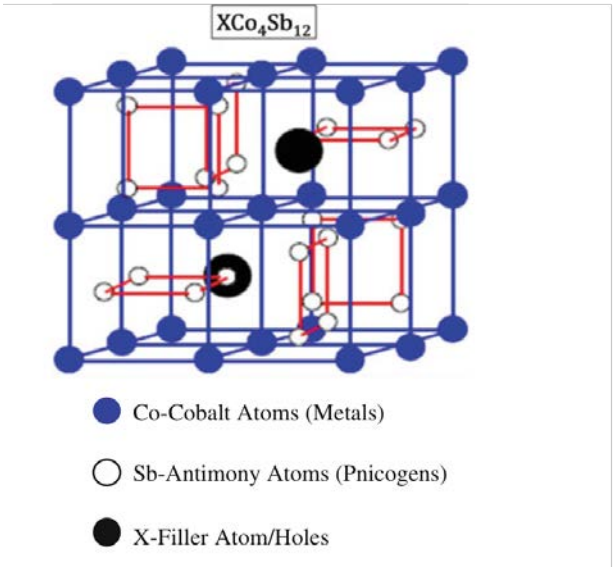

Figure 5.8: Skutterudite structure. *Source Ref. [72]*.

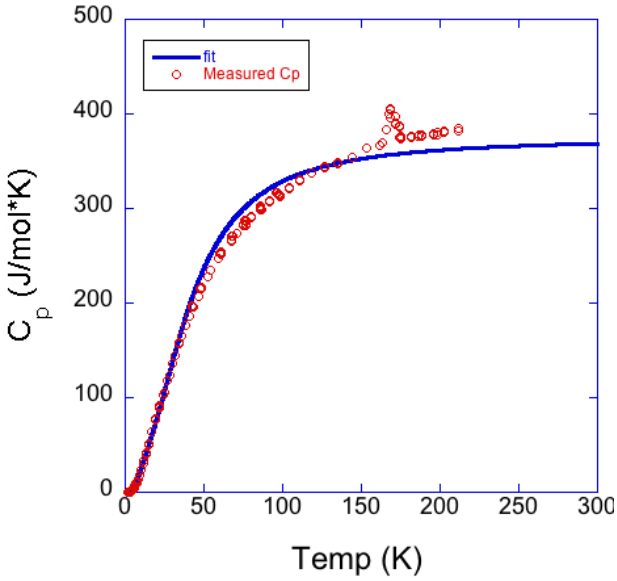

Figure 5.9: Measured Specific Heat (C_p) of Ag_8GeTe_6 plotted along with the combined Einstein and Debye model.

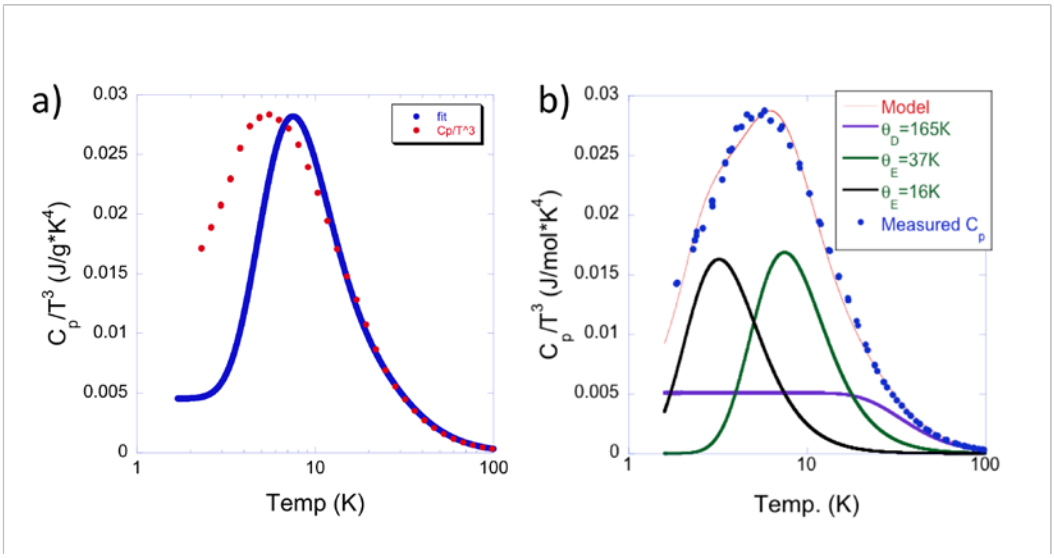

Figure 5.10: Low temperature specific heat (C_p) of Ag_8GeTe_6 divided by T^3 plotted versus *logT* to show the so called Boson peak along with a) a combined Einstein Debye model using a single Einstein mode and b) a fit using two separate Einstein modes.

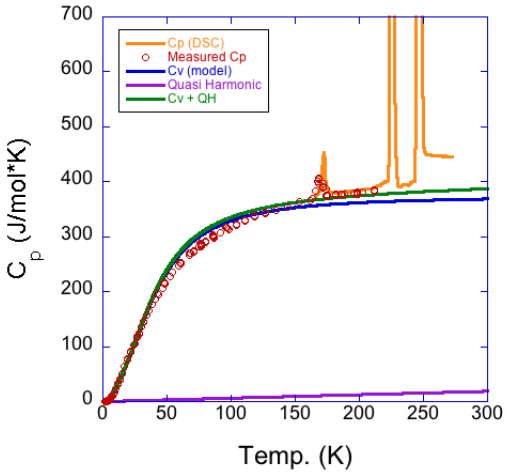

Figure 5.11: The measured Specific Heat (C_p) of Ag_8GeTe_6 plotted along with two models 1) a harmonic combined Debye and Einstein model with two Einstein modes as well as 2) a similar model that includes and additional Quasi-Harmonic contribution.

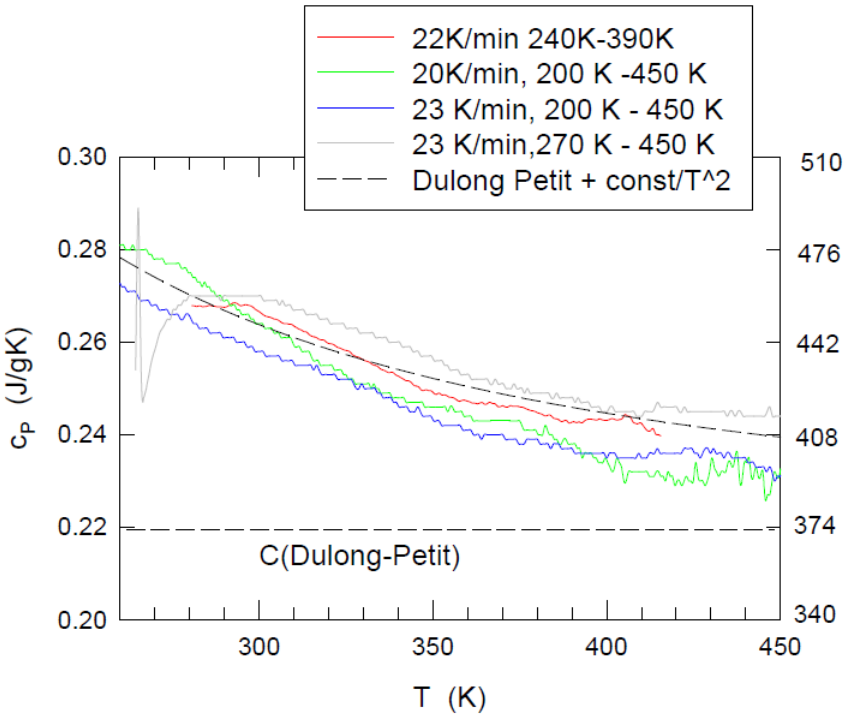

Figure 5.12: Specific Heat (C_p) of Ag_8GeTe_6 measured using several different heating rates plotted along with a fit to a model containing both a Debye lattice and a Schottky anomaly.

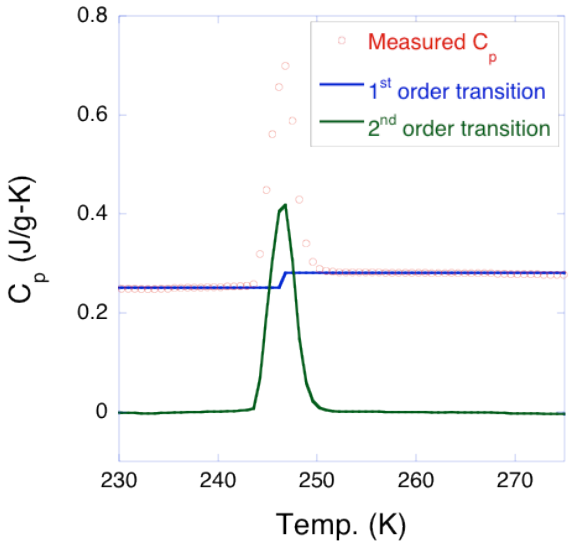

Figure 5.13: Specific Heat (C_p) of Ag_8GeTe_6 near the phase transition at 245K, can be broken into two parts-a first order transition and a second order transition.

CHAPTER SIX

THERMAL CONDUCTIVITY

6.1 Introduction

In the first few chapters, we probed the charge, spin and orbital degrees of freedom in Ag_8GeTe_6. These results have set the stage for understanding the behavior of the thermal conductivity of Ag_8GeTe_6. Moreover as discussed on the previous chapter when it comes to probing the dynamics of an insulating or highly resistive material thermal conductivity plays a similar role to the electrical conductivity in conductors. However even in non-correlated electron systems, the coupling between the lattice, charge, orbital and spin degrees of freedom can be crucial. As such, the thermal conductivity must be addressed in connection to our earlier measurements for a complete and coherent understanding of the material system. The magnetic susceptibility data showed Ag_8GeTe_6 is persistently diamagnetic without any long range ordering, consistent with an insulating material with low carrier concentration, which was confirmed by the analysis of low temperature heat capacity (i.e., the negligible Sommerfeld coefficient, discussed in **Chapter 5 Section 6.1**). Temperature independent magnetic susceptibility also suggests an inert role of the orbital degree of freedom (especially in the region of the phase transitions). As such, we will neglect the contribution of spin and orbital degrees of freedom in the following analysis. Instead, we will focus on the charge (*electronic* and *ionic*) and lattice (static and dynamic) degrees of freedom.

Electrically, Ag_8GeTe_6 shows variable range hopping behavior, as evidenced by the electrical resistivity, the Hall mobility, and the Seebeck coefficient (**Chapter 4**).

Bearing in mind the material becomes a mixed conductor above 245K we measured the Ag ionic conductivity near room temperature. The preliminary results suggest the ionic conductivity is at least 2 orders lower than the electronic counterpart, though we must stress that the W-F relationship has an ionic counterpart and the Lorenz number can be much larger for ions than electrons or, therefore it is premature to conclude that the carrier thermal conductivity is small from the small ionic conductivity.[88] Another factor discerned from the heat capacity measurements and analysis is the existence of strong anharmonicity, as evidenced by the large acoustic mode-averaged Gruneissen parameter (~ 3.8) at room temperature (**chapter 5 section 6.3**). Ag_8GeTe_6 undergoes four phase transitions between 150 K and 250 K., as well as multiple phase transitions above room temperature, indicating the material system is inherently unstable. With this in mind we measured the thermal conductivity of Ag_8GeTe_6.

Generally speaking, in solid materials heat can be *stored* and *transported* by any type of excitation. In most cases, however, the electronic and phononic contributions dominate. For this reason it is generally accepted that heat is mainly stored and transported by a combination of charge carriers and phonons or lattice. Furthermore in the presence of strong electron-phonon coupling it is not physically sound to visualize *bare* electrons or phonons as a result the quasi-particles picture must be used. This is most likely not the case in Ag_8GeTe_6 (as was discussed in **Chapter 4**) and will therefore be considered beyond the scope of this thesis.

The electronic contribution to the thermal conductivity is proportional to the electrical conductivity and can be described by the Wiedemann–Franz relation

($\kappa_{carrier} = \sigma L_0 T$), where σ is the electrical conductivity, L is the Lorenz number taken to be 2.44*10^{-8} WΩK^{-2} for degenerate semiconductors or 1.5 ×10^{-8} WΩK^{-2} for non-degenerate materials,[89] and T is the absolute temperature. The validity of this relationship must be questioned from the onset when studying any new material system as it is well known that the Lorenz number can vary quite a bit between materials and over temperature. The degenerate value of the Lorenz number (2.44 ×10^{-8} WΩK^{-2}) can be exactly calculated using Fermi Dirac statistics as was shown by Sommerfeld in 1927.[90]

$$L_0 = \frac{\pi^2}{3}\frac{k_B^2}{e^2} = 2.44 \times 10^{-8} W\Omega K^{-2} \quad (5.1)$$

This value only holds under very specific conditions (based on the assumptions of the model) the first being that the material is highly degenerate, and the second is the assumption that phonon and electron mean free paths are proportional. In cases where the difference in mean free path is small and the system is degenerate the proper value of the Lorenz number can be calculated using the equation

$$L = \frac{\kappa}{\sigma T} = L_0\left(\frac{l_t}{l_E}\right) \quad (5.2)$$

where κ is the carrier thermal conductivity, l_T is the electron mean free path for thermal conductivity, l_E is the electron mean free path for electrical conductivity.[91] Additionally from dimensional analysis point it is clear that the units of Seebeck coeifficient and the Lorenz number are very similar which suggests they are related. This is indeed that case as both can be considered to be a gauge of entropy flow with respect to a parent charge flow.

In the case of Ag_8GeTe_6 the electronic contribution to the thermal conductivity is negligible due to the low electrical conductivity discussed in **Chapter 4.** Furthermore, in

Ag_8GeTe_6 the ionic contribution to the thermal conductivity *cannot* be ignored due to the large ionic conductivity at elevated temperatures, and can be described in the same way as the electronic thermal conductivity by simply changing the Lorenz number to that of ions instead of electrons (holes).[88] Especially in the low temperature regime the ionic conductivity is negligible (essentially zero below the phase transition at 245K), hence below room temperature the thermal conductivity can be considered to be solely due to phonons. At room temperature and above the nonzero ionic conductivity suggests that the ionic contribution to the thermal conductivity could be substantial especially in light of the fact that the Lorenz number for ionic charge carriers can be two to three orders of magnitude as large as that for electrons (holes).[88] Finally as discussed at the end of the last chapter on specific heat the Ag sublattice of Ag_8GeTe_6 undergoes a premelting transition above 245K, which not only allows for more "dynamic" scatterers in the lattice, but also fundamentally changes the way heat is stored and transported in the material by eliminating transverse phonon modes in a part of the lattice!

The goal of this chapter is to answer three main questions:

(1) how do the 4 consecutive phase transitions affect the thermal conductivity of Ag_8GeTe_6?

(2) how does anharmonicity impact the thermal conductivity?

(3) how much and in what way does the ionic conductivity and premelting of the Ag sublattice contribute to the heat conduction?

6.2 Basics of Thermal Conduction in Solids

Thermal conductivity is the product of how much heat is stored in a material (i.e., specific heat) and how easily it moves under a temperature gradient (i.e., phonon mobility). Using simple kinetic theory the lattice thermal conductivity of solid materials can be well described by the equation

$$\kappa_{lattice} = \frac{1}{3} C_v v l \tag{5.3}$$

where C_v is the specific heat at constant volume, v is the velocity of sound in the material, and l is the phonon mean free path.[92] Unlike the specific heat and the mean free path the velocity of sound is a material dependent parameter that varies very little with changes in temperature, morphology, or doping. Hence the behavior of the lattice thermal conductivity largely reflects the variations of specific heat and phonon mean free path. As described in the previous chapter the specific heat (C_v) of a solid material can be well described using the Debye model, varying as T^3 at low temperatures before saturating at the Dulong-Petit limit of $3R/M$, where R is the gas constant (taken to be 8.314 (J/mol*K)) and M is the molar mass. It should also be noted that in this case C_v is used rather than C_p. In most cases C_v and C_p are used interchangeably, which can be justified by the fact that in many materials the difference between C_p and C_v is at most a few percent. In this case physically the distinction between C_p and C_v is important. Because C_v is a measure of the heat stored by the lattice at constant volume it contains only contributions from excitations in the lattice, generally in the form of phonons, C_p on the other hand includes contributions not only from the excitations but also a contribution from thermal

expansion. Importantly energy input in the lattice that goes into thermal expansion will not contribute to the thermal conductivity, *therefore C_v is more relevant, as compared to C_p, when considering thermal conductivity*. The phonon mean free path of a solid material is strongly dependent on the detailed scattering mechanism. The scattering mechanism of phonons should be described by an equation similar to Matthiessen's rule for electrons $\tau_C^{-1} = \sum_i \tau_i^{-1}$ where τ_C is the total phonon scattering relaxation time.

In a purely harmonic lattice phonons cannot interact, however in 1929, Peierls demonstrated that elastic waves can be scattered by each other, as a result of anharmonicity of the interatomic potential.[93] This can be understood in the quantum picture where scattering processes can be described through the destruction and creation of some quanta of elastic energy. Though certainly not the only quantum scattering process the most likely phonon scattering process is three-quantum scattering in which two quanta "scatter" and are destroyed while a third is created or vice versa. In his description of the problem Peierls showed that two conservation laws had to be obeyed:

$$\hbar\omega_1 + \hbar\omega_2 = \hbar\omega_3 \tag{5.4}$$

and

$$\hbar\mathbf{k}_1 + \hbar\mathbf{k}_2 = \hbar\mathbf{k}_3 + j\hbar\mathbf{G} \tag{5.5}$$

where *w* is the (angular) frequency of the quanta and |E is Planck's constant divided by 2p**,** $k_i = 2\pi / \lambda_i$ is the wavevector, ***G*** is the reciprocal lattice vector, and *j* can be either 0 or ± 1. The first equation expresses the conservation of energy, while the second equation is analogous to the conservation of momentum for the process. At this

point it is informative to break these scattering processes into two groups: a first group where $j=0$ is called Normal processes (n-process). In an n-process k_3 is less than $2p/a$ and therefore remains inside the first Brullion zone. In this way the momenta of the initial waves simply add to form a new wavevector traveling in the same direction and the *total* wavevector will be conserved. For this reason there will be no influence on the flow of energy and therefore no thermal resistance associated with this type of process. Though n-processes do not directly contribute to thermal resistance their effect on thermal conductivity is not negligible as will be discussed in **Section 2.2**. The second group of scattering processes, where $j=\pm 1$, are called UmKlapp Processes (U-Process). A simple diagram of the initial and final wavevectors in reciprocal space illustrates the difference between n and U processes and can be seen in **Figure 6.1**. In a U-process k_3 is larger than $2p/a$ and is therefore ends up outside the first Brillouin zone. This however, isn't physical as it corresponds to a wave with wavelength shorter than $2a$, or twice the lattice spacing. Nevertheless the situation can, be described in the context of a wave traveling in the opposite direction whose wave vector can be described be the equation: $\boldsymbol{k}_3^* = \boldsymbol{k}_3 - \boldsymbol{G}$. Because this type of process involves phonons moving *against* the initial phonons it involves a thermal resistance.[94]

For highly crystalline materials at low temperatures the phonon mean free path is on the order of the sample dimension therefore the thermal conductivity varies as T^3. At higher temperatures, however, the specific heat saturates and the onset of phonon-phonon scattering (UmKlapp scattering) causes the thermal conductivity to vary as $1/T$. This is due to the fact phonon mean free path follows a temperature dependence of $1/T$ when

UmKlapp scattering dominates and at temperatures comparable to the θ_D and above both C_v and the v_s are weakly temperature dependent, as discussed in the previous chapter. This behavior leads to the so-called crystalline peak in thermal conductivity (at ~ 1/10-1/20 θ_D) shown in **Figure 6.2**.[95] Indeed one of the most intriguing aspects of the thermal conductivity of Ag_8GeTe_6 is the deviation from this temperature dependence typical of a crystalline material, which will be discussed later in the chapter.

Furthermore when considering the lattice thermal conductivity of a crystalline material it is informative to consider the phonon dispersion relation, which describes the connection between frequency and momentum for the allowed phonon modes in the material. In a monatomic material there are only three phonon modes (two transverse modes and one longitudinal mode) which (in the long wavelength limit) correspond to atoms in the unit cell moving in phase with each other. The phonon dispersion relations of materials with more than one atom per unit cell are more complex. In that case there are still three acoustic modes, but in addition the acoustic modes there are also *3n-3* optical modes, where *n* is the number of atoms per unit cell. Unlike acoustic modes in the long wavelength limit optical modes correspond to the movement of atoms in the unit cell out of phase with each other. In general optical phonon modes carry less heat than acoustic modes because their group velocity, given by *dw/dq*, is small. For this reason optical phonon modes can *store* heat in a material, but do not *carry* much heat, though they can still have an effect on heat conduction by interacting with (scattering) heat carrying acoustic modes. Hence when we use question (1) to estimate the phonon mean

free path, the value is more likely the lower limit of the phonon mean free path rather than the actual mean free path.

6.2.1 Phonons in Amorphous Materials

Though we know from our x-ray studies (**Chapter 3**) that our Ag_8GeTe_6 samples are crystalline many of the their properties appear to mimic an amorphous material. For this reason it is important to consider the difference between phonons in crystalline materials, where a periodic lattice I well defined and hence *k* is a good quantum number, and amorphous materials where the atomic periodicity is not as well defined. A very good review paper [96] was published by S. Hunklinger in 1982 discussing the difference between crystalline and amorphous materials where in his words “the enormous simplification engendered by the periodicity of the crystalline structure is lacking”. For this reason the normal modes of the material are no longer plane waves which leads to damping of the phonons as in anharmonic crystals. These effects are particularly important in the short wavelength limit because the average atomic distribution normalizes as the length scale increases. Like crystalline materials in the limit of long wavelength amorphous materials behave as elastic continua. In the context of a phonon dispersion relation an amorphous material should look identical to its crystalline counterpart near the zonecenter, however, with increasing wavevector the dispersion will be more and more smeared out until it reaches the boundary of the first Bruillion where it is no longer distinguishable, due to the lack of short range atomic order. In this sense in the long wavelength limit the phonons in amorphous materials are indistinguishable from

their crystalline counterparts, but as the wavelength decreases the classical definition of phonons begins to breakdown.

6.2.2 Thermal Relaxation Approximation and the Callaway model

As mentioned above the thermal conductivity of a solid material is strongly dependent on the dominant scattering mechanism. In this way the thermal conductivity of a solid material in the momentum relaxation regime can be well understood in the context of the relaxation time approximation and, going a step further, the Callaway model. The total relaxation time of a material at a given temperature should follow the equation:

$$\tau_C^{-1} = \sum_i \tau_i^{-1} \tag{5.6}$$

Assuming that the distribution of phonons is restored to equilibrium at a rate proportional to its departure we end up with the *Relaxation Time Approximation*. Furthermore by assuming a linear dispersion relation the thermal conductivity can be expressed as:

$$\kappa_L = \frac{k_B}{2\pi^2 v}\left(\frac{k_B T}{\hbar}\right)^3 \int_0^{\theta_D/T} \frac{x^4 e^x}{\tau_C^{-1}\left(e^x - 1\right)^2} \tag{5.7}$$

In this model only scattering that directly leads to thermal resistance is included in the thermal conductivity. Hence normal processes are ignored, though assumption may be too simplistic.[97]

In 1958 Callaway presented a model to describe the low temperature thermal conductivity of crystalline solids that included a contribution to the thermal conductivity due to normal processes. Specifically Callaway considered the possibility that normal processes redistribute the momentum and energy of phonons to states that are less likely

to experience resistive scattering processes. Hence the thermal conductivity can be broken into two parts: a normal part and a resistive part.

As in the thermal relaxation model Callaway assumed that phonon scattering processes can be represented by their frequency dependent relaxation times (τ), and that the vibrational spectrum of the material is dispersion-less. Additionally Callaway assumed that the material of interest is elastically isotropic. [98] From here Callaway assumed that the phonon scattering in a given material can be completely described using four terms: (1) Boundary scattering, which has a constant relaxation time, (2) Normal three phonon processes, whose relaxation time should follow $(\omega^2 T^3)^{-1}$, (3) Impurity scattering which has a constant relaxation time in temperature but should be proportional to ω^{-4}, and (4) Umklapp process whose relaxation time should be proportional to $(e^{-\theta/aT}\omega^2 T^3)^{-1}$ where θ is the Debye temperature and a is a constant which depends on the vibrational spectrum of the material. At this point is possible to calculate two relaxation times for the material using the equations:

$$\tau_R^{-1} = A\omega^4 + B_1 T^3 \omega^2 + C \tag{5.8}$$

And

$$\tau_n^{-1} = B_2 T^3 \omega^2 \tag{5.9}$$

where B_1 describes the contribution of Umklapp processes and is equal to $e^{-\theta/aT}$ and B_2 is a constant which describes the contribution of normal processes thus τ_R can be considered the total resistive process relaxation time and τ_n is the relaxation time for normal processes. From the lattice thermal conductivity can be estimated by the equation:

$$\kappa_L = \kappa_1 + \kappa_2 = \frac{1}{3}CT^3 \int_0^{\theta/T} \frac{\tau_C(x)x^4e^x}{\left(e^x-1\right)^2}dx + \frac{1}{3}CT^3 \frac{\left[\int_0^{\theta/T} \frac{\tau_C(x)x^4e^x}{\tau_n(x)\left(e^x-1\right)^2}dx\right]^2}{\int_0^{\theta/T} \frac{\tau_C(x)x^4e^x}{\tau_n(x)\tau_R(x)\left(e^x-1\right)^2}dx} \quad (5.10)$$

Where the first term κ_1 is identical to the Thermal Relaxation Approximation and the second term κ_2 describes the added contribution due to the consideration of normal processes.

6.2.3 Cahill Model

Clearly the conduction of heat in amorphous solids must follow different rules than crystalline materials due to the lack of long-range periodicity. In fact even before 1950, Kittel described the conduction of heat in amorphous materials as fundamentally different than their crystalline counterparts.[99] Whereas the thermal conductivity of crystalline materials is dominated by waves, long wavelength acoustic phonons to be exact, in amorphous materials this is not possible. Due to the large number of scattering centers the mean free path of phonons in an amorphous solid is on the order of the interatomic spacing. In many ways the thermal conductivity of amorphous materials cannot be considered in the context of bands at all. This can be considered to be somewhat analogous to the difference between band conduction and hopping conduction by electrons or holes (**Chapter 3**), though hopping conduction (electrons) and diffusive conduction (phonons) are fundamentally different.

In 1989 Cahill and Pohl proposed a model as an extension of the Debye model of specific heat that describes "a random walk of energy between localized oscillators of varying sizes and frequencies."[100] The Cahill model can be described by the equation

$$\kappa_{\min} = \left(\frac{\pi}{6}\right)^{1/3} k_B n_a^{2/3} \sum_i v_i \left(\frac{T}{\theta_i}\right)^2 \int_0^{\theta_i/T} \frac{x^3 e^x}{\left(e^x - 1\right)^2} dx \qquad (5.11)$$

where the sum is taken over the three sound modes (one longitudinal v_l and two transverse v_t) and q_i is the cutoff frequency of the different modes. q_i is given by the equation

$$\theta_i = v_i \left(\hbar / k_B\right)\left(6\pi^2 n\right)^{1/3} \qquad (5.12)$$

From a glance it is clear that this cutoff is similar to the Debye temperature. Indeed q_i is analogous to the Debye temperature of a material, however each q_i corresponds to a specific direction while the Debye temperature of a material is a bulk property . Though initially developed to describe amorphous materials the Cahill model has more recently been used to describe the minimum lattice thermal conductivity of crystalline materials. The idea being that as the phonon mean free path of a crystalline material decreases it becomes more and more amorphous until the phonon mean free path is on the order of the interatomic spacing in which case the thermal conductivity of the "crystalline" material should be equal to its amorphous counterpart. This value has become particularly useful for thermoelectricians because it offers a simple way (the only parameter you need is the Debye temperature) to estimate the ideal thermal properties of a new thermoelectric material.

6.2.4 Anharmonicity

The above models are based on momentum relaxation processes, so any variation in thermal conductivity is governed by the phonon mean free path in the spatial domain. In this regard, anharmonicity is concerned with the phonon life time in the temporal domain. Generally speaking, anharmonicity limits the maximum thermal conductivity, but to beat the minimum thermal conductivity, according to the Cahill model, solely by anharmonicity, the phonon life time must be shorted beyond the minimum phonon mean free path divided by the velocity of sound.

The effects of anharmonicity on the thermal conductivity of solid materials are not well understood. On the one had the complete absence of anharmonicity, i.e. a perfectly harmonic lattice, would lead to the complete absence of phonon-phonon interactions which dominate the behavior of the thermal properties of most materials at high temperatures. Indeed without phonon-phonon interactions an infinite periodic lattice would display and infinite thermal conductivity. In the other extreme in the presence of strong anharmonicity the effects on thermal conductivity are much harder to quantify. Experimental observations have led people to believe that strong anharmonicity leads to low thermal conductivity. As early as the 1970s Slack suggested that thermal conductivity is lowered by anharmonic crystal interactions, and offered the following equation to quantify its effects[101,102]

$$\kappa_{latt.} = A\frac{\overline{M}\theta_a^3\delta n^{1/3}}{\gamma^2 T} \tag{5.13}$$

where $\overline{M}$ is the average atomic mass in the crystal, *A* is a collection of physical constants, θ_a is the Debye temperature of the acoustic modes of the crystal, *d* is the volume per atom n is the number of atoms in the primitive cell γ is the Gruneissen parameter, and *T* is the absolute temperature. As discussed in the previous chapter the Gruneissen parameter is a rough gauge of the anharmonicity of a material therefore one can expect the thermal conductivity to vary as the square of the inverse of the strength of the anharmonicity. Though this equation has been used many times over the years its understanding is still phenomenological in nature and a complete understanding of *how* anharmonicity effects thermal conductivity is lacking.

Perhaps the best example of anharmonicity induced amorphous-like thermal is the I-II-IV_2 class of semiconductors. Recent work has shown that though they crystallize in the high-symmetry rocksalt structure I-II-IV_2 semiconductors display unusually low thermal conductivity near the amorphous limit. Furthermore this low thermal conductivity is very reproducible in both experimental and theoretical studies, which suggests that it is not the result of defect structures or a similar phenomenon, but rather due to an intrinsic and inherently reproducible process.[103,104,105] In this case the low thermal conductivity has been attributed to lone pair induced anharmonicity in the lattice. **Figure 6.3** taken from [104] shows the effects of lone pair electrons in reducing the thermal conductivity of Cu-Sb-Se ternary compounds. The Cu-Sb-Se system offers a perfect platform to study the effect of LEPs on thermal conductivity in that there are three compounds (Cu_3SbSe_4, $CuSbSe_2$, and Cu_3SbSe_3) made of similar atoms, which crystallize in the same structure (orthorhombic, *Pmna*), and therefore would be expected

to display similar values of thermal conductivity. Importantly the main difference between the compounds studied is the local environment of the Sb atoms. The difference in the thermal conductivity of Cu_3SbSe_4, $CuSbSe_2$, and Cu_3SbSe_3 can be well understood in the context of valence shell electron repulsion (VSEPR) theory. In the case of Cu_3SbSe_4 the Sb atoms in the middle of the tetrahedral are completely bonded and therefore display ideal tetrahedral bonds of 109.5° and a "harmonic" potential environment. In the case of $CuSbSe_2$ and Cu_3SbSe_3 however some of the 5*s* electrons of the Sb atom remain localized around the nucleus and therefore repel the Se atoms according to VSEPR theory and distort the Se-Sb bond angles. For these materials the difference in the Se-Sb-Se bond angle can be attributed to differences in the effective valence state of Sb, and can be calculated using the equation

$$^{eff}V_{Sb^{3+}}(\bar{\alpha}) = 3[1+0.0128(\bar{\alpha}-90)] \quad (5.14)$$

where $(\bar{\alpha})$ is the Se-Sb-Se bond angle.[106] Using Equation xx and the effective Sb valance states of 3.2 in $CuSbSe_2$ and 3.36 in Cu_3SbSe_3 it is possible to directly calculate the bond angles to obtain 95.25° and 99.42° respectively. At first glance this would suggest that $CuSbSe_2$ will display stronger anharmonicity and thus a lower thermal conductivity than Cu_3SbSe_3. However the bonding in $CuSbSe_2$ is nearing the ideal Se-Sb-Se bond angle of 90° in the case of Sb^{3+} ions. This suggests that of the three compounds Cu_3SbSe_3 should display the strongest anharmonicity and thus lowest thermal conductivity followed by $CuSbSe_2$ and finally Cu_3SbSe_4, which is confirmed by the measured thermal conductivity data shown in **Figure 6.3a.** A further crosscheck of the strength of the anharmonicity in the Cu-Sb-Se series of compounds is their Gruneissen

parameter. In a more recent paper Zhang et al. calculated the Gruneissen parameter of Cu_3SbSe_3 and Cu_3SbSe_4 and found that the average square value is significantly larger in Cu_3SbSe_3 than Cu_3SbSe_4 suggesting that it has a stronger lattice anharmonicity. They again attribute this difference to repulsion between lone *s2* pair electrons and the surrounding lattice. An important observation noted in [105] is the connection between marginally stable compounds, like Ag_8GeTe_6, and highly anharmonic acoustic phonons.

6.3 Measurements

6.3.1 Steady State Measurement

The low temperature thermal conductivity of Ag_8GeTe_6 was measured with an in-house custom designed system between 20K and 300K using a steady-state technique.[107] The measurement system was designed by Dr. Amy Pope as part of her Ph.D. thesis, and is built around an Advanced Research Systems (ARS) closed cycle He cryostat. As with any steady state measurement precise temperature control is critical. Therefore coupled to the cryostat is a Lake Shore model 340 temperature controller, which allows the system temperature to be maintained within 0.025K during the measurement. The sample is mounted on a modified Quantum Design PPMS puck. A diagram of the mount is shown in **Figure 6.4**. As can be seen in the picture there is a 220Ω strain gauge mounted on top of the sample, which acts as a heater. Additionally a 0.001”Cn–chromel differential thermocouple is soldered to two #34 copper wires, which have been attached to the

surface of the sample using Stycast®. These copper wires ensure that the thermocouple is both well thermally sunk and mounted on an equi-temperature plane across the sample.

The first step in taking a measurement is to stabilize the system temperature (base temperature) within 0.025K for three minutes. Then a current is passed through the heater on top of the sample, and the temperature gradient monitored using the thermocouple. Once the temperature gradient is stable within 0.025K the current (heater power) and ΔT are recorded. The heater power is then increased and another data point taken. This process is repeated at least five times. At this point the thermal conductance is calculated as the slope of the power versus ΔT plot, and finally thermal conductivity is calculated by scaling the thermal conductance by the sample dimensions.

6.3.2 Laser Flash

To obtain the thermal conductivity above room temperature the thermal diffusivity was measured using a Netzsch 457 Microflash Laser Flash Apparatus (LFA). In the most general sense the thermal diffusivity of a material is a measure of its ability to transport heat relative to its ability to store heat. In order to perform a LFA measurement a quanta of heat in the form of a laser pulse ($\leq$1 msec) is imparted on one side of the sample, at the same time the temperature of the other side of the sample is continuously monitored using a Liquid Nitrogen cooled IR detector. From here is possible to calculate the thermal diffusivity using a predetermined model. The simplest model for laser flash analysis was developed by Parker et al. in 1961[108] allows the diffusivity to be calculated using the equation

$$D = 0.1388\frac{d^2}{t_{1/2}} \tag{5.15}$$

where d is the thickness of the sample and $t_{1/2}$ is the time it takes the signal to reach half of its maximum value. In this model it is assumed that both the material and the energy input are homogeneous, the laser pulse is infinitely short (a Dirac-delta function), the system is adiabatic (there are no heat losses), and the faces of the sample are both perfectly flat and parallel. In 1963 Cowan presented a more sophisticated model that allows for energy losses at the surface of the sample in the form of both convection and radiation.[109] These corrections are particularly important in two cases: first for measurements at high temperatures and second for samples with low diffusivity values which allow the sample to reach near equilibrium conditions during the measurement. As expected Cowan's model generalizes to the Parker model when surface losses become negligible. Due to its low thermal conductivity and hence diffusivity Ag_8GeTe_6 fits the second class described above therefore the Cowan model was used for all analysis of LFA data.

During the initial diffusivity measurements it became apparent that Ag_8GeTe_6 is at least partially transparent to IR radiation. To correct for this gold was sputtered on both surfaces of the sample before coating graphite to keep the laser from passing through. Once suitable diffusivity data had been obtained the thermal conductivity was calculated using the equation:

$$\kappa = dDC_v \tag{5.16}$$

where d is the density and C_v is the specific heat.

6.3.3 Measurement Considerations

It should be noted that due to its unusually small magnitude, ~0.3 W/m*K at room temperature, the thermal conductivity of Ag_8GeTe_6 is near the detection limit of both the steady state and laser flash systems which makes it very difficult to resolve and obtain accurate values. As can be seen in **Figure 6.5** there is an upturn in the thermal conductivity versus temperature plot, which can be at least *partially* attributed to the onset of a radiation contribution to the measured thermal conductivity.

The nature of this contribution is clearly evident if we consider the way thermal conductivity is calculated in a steady state measurement. In a steady state thermal conductivity measurement a thermal flux is driven through the sample using a heater at a set power, which can be calculated as I^2R, next the temperature gradient across the sample is monitored. Once a stable temperature gradient has been achieved the thermal conductance can be calculated as the input power divided by the induced temperature gradient, and thermal conductivity obtained by scaling by the samples dimensions. As seen in **Equation 1.2** however this method breaks down when all of the heat does not flow directly through the sample, with any heat losses leading to measured thermal conductivity that is higher than the true value.

$$\kappa = \frac{P}{\Delta T}\frac{L}{A} = \frac{P_{total} - P_{loss}}{\Delta T}\frac{L}{A} \tag{5.17}$$

As is evident from equation the lower the thermal conductivity of the sample the more important it is to try to minimize heat losses when performing a steady state thermal conductivity measurement. For this reason care has been taken while designing the

apparatus to try and minimize any conductive heat losses leaving radiative losses as the main source of error in the thermal conductivity measurements.

6.3.4 Heat Losses

Central to any steady state thermal conductivity measurement is the ability to minimize heat losses. Indeed care was taken during the design of the system to minimize these losses. These measures included: 1) the use of multiple radiation shields to minimize radiative losses, 2) the use of a turbo molecular vacuum pump to achieve high vacuum (10^{-8} Torr) to minimize convective heat losses, and 3) the use of small diameter thermocouples and phospor bronze heater leads to minimize conductive heat losses. Indeed for most semiconducting samples these measures are enough to yield accurate data. For samples with low thermal conductivity, however, they are not enough, and losses become important to the measurement. Generally these losses can be attributed to radiation, and make up less than 30% of the entire signal. In the usual case the radiative losses appear as an upturn in the thermal conductivity versus temperature plot above about 150 K. In that case it is safe to subtract the radiation term using the following procedure: First the electronic contribution to the thermal conductivity is subtracted using the Wiedemann–Franz relation, discussed above, and then the remaining thermal conductivity is fit using the equation:

$$\kappa_l = \alpha \frac{1}{T} + \beta T^3 \tag{5.18}$$

where the first term $\alpha(1/T)$ corresponds to the intrinsic thermal conductivity dominated by U-processes and the second term βT^3 corresponds to the radiation contribution. The formula for radiative heat loss is given by the equation:

$$Q = \varepsilon \sigma_{SB} A\left(T_{Sample}^4 - T_{Surroundings}^4\right) \quad (5.19)$$

where ε is the emissivity of the sample, σ_{SB} is the Stephan-Boltzmann constant ($5.7*10^{-8}$ W/m^2*K^4), and A is the surface area of the sample. The T^3 dependence of the radiation term is evident after a Taylor expansion of the $\left(T_{Sample}^4 - T_{Surroundings}^4\right)$ term in which the lead term has a T^3 temperature dependence. Once the data has been fit the radiation contribution can be subtracted to obtain the intrinsic value of the thermal conductivity. While this type of correction is valid for many materials it is difficult to defend for Ag_8GeTe_6 for two reasons: first fitting the intrinsic thermal conductivity of Ag_8GeTe_6 to *1/T* is problematic because unlike most crystalline materials U-processes are not necessarily the dominate type of phonon scattering, and second the radiation contribution in Ag_8GeTe_6 is very large ~50% of the magnitude of the signal.

In order to obtain a proper radiation correction for Ag_8GeTe_6 we tried several different methods. First we measured the thermal conductivity of a sample with well-known dimensions then cut the sample so that its new length was 30-50% of the original length and measured it again. In this sense the radiation contribution should have been decreased as the surface area decreased according to **Equation 6.2**. Two samples were measured this way, and as expected the magnitude of the measured thermal conductivity decreased after they were shortened, however, due to brittle nature of the samples parts of them crumbled between the measurements making impossible to maintain their cross section. This meant that though the existence of a radiative contribution to the measured thermal conductivity was confirmed it was impossible to accurately subtract it. For our second attempt to correct for radiative losses we measured the thermal conductivity of a

sample, then coated the surface of the sample with graphite, and finally re-measured the thermal conductivity of the sample. In this way we hoped to change the emissivity (ε) of the sample and hence the radiation contribution to the signal according to **Equation 6.19**. **Figure 6.6** shows the thermal conductivity of the sample with and without the graphite coating. From the figure it is clear that the graphite coating did little to alter the emissivity of the sample, which could be verified by simply looking at the surface of the sample. Pristine Ag_8GeTe_6 has a diffuse dark grey color on its own so the addition of the graphite coating did very little to alter the surface of the sample. The final way we tried to correct for radiation was to measure the thermal conductivity of Ag_8GeTe_6 at room temperature using a laser flash technique; because the laser flash is a transient type measurement there should be no heat loss due to radiation. Once the thermal conductivity was measured using the laser flash it was compared to the room temperature values obtained using the steady state technique. To perform the correction we assumed that the entire difference between the room temperature values of thermal conductivity measured by the steady state technique and by the laser flash was due to radiation. Furthermore we assumed that this radiative contribution followed a T^3 temperature dependence as is normally the case. In this way we fit the measured thermal conductivity to the equation:

$$\kappa_{measured} = \kappa_{intrinsic} + \beta T^3 \tag{5.20}$$

At this point it was possible to calculate the intrinsic thermal conductivity by subtracting the radiative contribution from the measured thermal conductivity. The results of this correction are shown in **Figure 6.7.** At this point the validity of this correction must be considered. Indeed a quick look at **Figure 6.7** suggests that the room

temperature value of the thermal conductivity is “over constrained”, however with no clear justification for altering the room temperature thermal conductivity values for different runs any further modification of the data would be on poorly justified.

6.4 Phase transitions

Perhaps the most surprising property of Ag_8GeTe_6 is the large number phase transitions occurring in such a narrow temperature range (Discussed in **Chapter 5**). Indeed there are barely discernible features in the thermal conductivity curve corresponding to at least two of the low temperature phase transitions.

It is possible that these signatures are the result of actual changes in the thermal conductivity of Ag8GeTe6 as it goes through the transitions, however, it is also possible that they are an artifact of the measurement. As discussed in **section 3.1** when a steady state thermal conductivity measurement is made the first step is to establish a stable base temperature followed by the establishment of a stable ΔT. It is possible that if the base temperature is near a phase transition it will be impossible for the system to stabilize because small fluctuations in the temperature have drastic effects on the specific heat of the material, and therefore cause huge swings in the amount of heat needed to obtain a stable base temperature. If the system is unable to obtain a stable base temperature it is programmed to “skip” that temperature and move on to a higher temperature creating a gap in the data. In our case however, we don’t see this gap suggesting that the changes in thermal conductivity are intrinsic.

Furthermore we should also note that we have purposefully avoided the discussion of the effect of the phase transitions above room temperature because the measurement breaks down in the region phase transitions due to inaccuracies in **Equation 6.16**. This is because in the region of a phase transition the definition of specific is subtly different.

6.5 Data Analysis

As confirmed by x-ray diffraction (see **Chapter 3**) Ag_8GeTe_6 is clearly a crystalline material. Its thermal conductivity, however, more closely resembles an amorphous material. Indeed x-ray diffraction measurements have verified that our samples are indeed crystalline and crystallize in cubic space group (F-43m) with a very large unit cell (a=11.56Å and containing 60 atoms). At first glance one may (naively) guess that the thermal conductivity of Ag_8GeTe_6 is quite large due to its similarities, high density and cubic crystal structure, to materials like iron. Further investigation however, reveals several factors that suggest the thermal conductivity of Ag_8GeTe_6 will in fact be low. First due to the low electrical conductivity the electronic contribution to the thermal conductivity can be considered negligible. Also due to its large unit cell Ag_8GeTe_6 has a very small Brillouin zone and therefore a high probability for U-processes. Furthermore the large number of atoms per unit cell leads to a large number of optical phonon modes (as mentioned above there should be *3N-3* optical modes where *N* is the number of atoms in the unit cell). This huge number of optical modes suggests that some of them may be "low lying" modes and likely increases the possibility of band hybridization, which will

further suppress (disrupt) the heat conduction of heat by acoustic bands. Finally strong anharmonicity as evidenced by the large Gruneissen parameter and thermal expansion coefficient offers another route to strong phonon scattering.

6.5.1 Phonon mean free path

In the preceding sections we have argued that though the thermal conductivity of Ag_8GeTe_6 appears to be amorphous like though the material is in fact crystalline. To further understand the microscopic nature of the thermal conductivity we have calculated the phonon mean free path (l_{ph}). Using the simple kinetic equation for thermal conductivity discussed in **Section 2** ($\kappa_{lattice} = \frac{1}{3} C_V v l$) along with our measured values for specific heat (**Chapter 5**) and the velocity of sound measured in [19] it is possible to estimate l_{ph}. We have also assumed that the velocity of sound is constant with temperature, which should be valid due to the fact that the Debye temperature is nearly temperature independent as discussed in **Chp 5**. **Figure 6.8** shows the estimated phonon mean free path for Ag_8GeTe_6. At least up to the range of the phase transitions l_{ph} follows an approximate *1/T* temperature dependence, as expected for a crystalline material. In the range of the phase transitions the assumptions of the estimation clearly break down as the kinetic equation for thermal conductivity can no longer be used. In the simplest sense this can be explained by the fact that during the phase transition heat input into the system goes into changing the lattice (or possibly other degrees of freedom) rather than being "stored" in the lattice in the form of phonons.

Furthermore if one of the Ag sites in the Ag_8GeTe_6 lattice behaves like an Einstein oscillator, as discussed in **Chapter 5**, one would expect the phonon mean free path l_{ph} to be similar in magnitude to the spacing between Einstein oscillators. This can be attributed to the fact that, as mentioned above, Einstein oscillators are inherently strong scatterers of phonons. The estimated phonon mean free path of ~3 Å at room temperature is slightly smaller than the Ag2-Ag2 spacing of 4Å, but is reasonable when you consider that all phonon modes contribute to specific heat but only certain modes contribute to κ. One step further the average interatomic spacing in the crystal structure can be calculated by calculating the volume of the unit cell then dividing by the number of atoms per unit cell and finally taking a cube root to convert from volume to length. This gives an average interatomic spacing of ~3 Å exactly the same value as the mean free path, suggesting that the thermal conductivity of Ag_8GeTe_6 is at the amorphous limit at room temperature.

6.5.2 Minimum Thermal Conductivity

As discussed in **Section 2.3** it is possible to calculate the so-called amorphous limit of the thermal conductivity of a solid material as described by Cahill et al.[100] According to **Equation 6.11** it is possible to calculate the "minimum thermal conductivity" of a material using only the number density of atoms in the material (n_A) and the Debye Temperature (θ_D). **Figure 6.9** shows the calculated minimum thermal conductivity of Ag_8GeTe_6 as well as the measured thermal conductivity as a function of

temperature. It is clear that the thermal conductivity of Ag_8GeTe_6 is significantly lower than the minimum value according to the Cahill limit. This is particularly evident when the difference between the measured thermal conductivity and the calculated minimum is plotted as a function of temperature as shown in **Fig 6.10**. Indeed the shape of this plot is somewhat surprising and reminiscent of phonon resonant scattering though the presence of resonant scattering in Ag_8GeTe_6 is not well supported.

It is plausible that the Einstein modes observed in the low temperature specific heat could lead to a phonon resonance; however a simple estimation of the maximum energy of the acoustic phonon modes in the material suggests that they will be completely populated before the observed resonant type behavior. In order to estimate the upper limit of the maximum energy of acoustic modes in the system we assume that slope of the acoustic modes in the phonon dispersion relation is not only constant until the 1st Brillouin zone boundary but also equal to its value at low *k*. Clearly this is an overestimate because at mid or short wavelengths the slope levels off in most cases. Next we must remember that the velocity of sound is determined by the slope of phonon dispersion relation for acoustic phonons at long wavelength limit, i.e. small *k*. Therefore we can estimate the maximum frequency of acoustic phonons using the equation

$$\omega_{\max} = v_s \times k_{\min} \tag{5.21}$$

where $k_{\min} = 2\pi / 2a = \pi / a$ and *a* is the lattice constant. In this case we use *a* the size of the unit cell rather than the interatomic spacing because acoustic phonons correspond to motion of the entire unit cell. Substituting the measured velocity of sound of ~1700 m/sec (it should be noted that this is more of a semi-quantitative estimate, but should good

enough for our estimate) and the lattice constant a of 11.56 Å into **equation 6.21** gives a maximum phonon frequency of 1.4×10^{12} Hz which corresponds to an energy of ~3.1 meV. This means that at 36 K, the acoustic modes should be thermally populated. In other words, above 36 K most of the thermal energy added to the system goes into populating optical modes. At least, we can safely assume so above 100 K and in the temperature range where those phase transitions occur.

Another method for estimating the maximum energy of the acoustic modes in a material was put forth by Anderson.[110] In his paper Anderson offers the empirical relationship

$$\theta_a = \theta n^{-1/3} \tag{5.22}$$

where θ is the "traditional" definition of the Debye temperature (θ_D) and n is the number of atoms per unit cell. The validity of this expression has been tested by comparing it to experimental data in several cases, and has proven to be a good estimation.[102,111] Substituting the appropriate values for Ag_8GeTe_6 (θ_D=176 K and n=60) into **Equation 6.22** give a value of 45K for θ_a. If we draw a parallel between θ_a and θ_D we can say that 45K is roughly the temperature where all of the acoustic modes are populated.

It is plausible to explain the resonant scattering regime by assuming that there are some dispersion-less optical branches in Ag_8GeTe_6, which can store but not carry heat. We can possibly even go a step further and assume that because of the strong anharmonicty, there may be coupling between the bands and thus avoided band crossing in this energy/temperature range. It should be noted that even if there is no avoided band crossing, the dispersion-less optical bands by themselves can explain the "resonance". In

this case there would have to be many levels in the given energy range as the resonance regime is fairly wide, between 50 K and 200 K. This scenario could be elucidated by inelastic neutron scattering measurements however our beam line proposal is declined. Furthermore the two or more Einstein modes as described in the chapter discussing specific heat (**chapter 5**) cannot explain the resonance as their characteristic temperatures, 15 K and 36 K, are too low to explain the "resonance".

Thermal conductivity values below the amorphous limit have been reported in materials at relatively high temperatures (~$T > 3\ \theta_D$), and can normally be understood in the context of the onset of higher energy excitations which can further interact with heat carrying phonons. The observation of a thermal conductivity values below the amorphous limit in Ag_8GeTe_6 is unusual however due to its onset at low temperatures ($T \sim \theta_D/3$). In this case one would generally assume that the temperature is too low to have a significant population of higher energy excitations as seen in other materials with such low thermal conductivity.

Thermal conductivity lower than the amorphous limit near or below the Debye Temperature of certain materials has been observed in a few cases. Normally only in very anisotropic (usually layered) materials and has been attributed to phonon localization due to a combination of disorder and anisotropy.[112] This scenario is unlikely in bulk Ag_8GeTe_6 because it has a cubic crystal structure and should therefore not be strongly anisotropic.

In order to explain the deviation of our measured thermal conductivity from the amorphous limit we must return to the basic assumptions of the Cahill model. Cahill's

model is based on a harmonic periodic crystal in which $\vec{k}$ is a good quantum number. This leads to elastic thermal relaxations (momentum relaxation) hence the minimum phonon mean free life can be given by the inter atomic spacing divided by the velocity of sound, $lifetime = \left(a^3 \middle/ n_a \right) \middle/ v_s$. In the case of strongly anharmonic crystals similar to Ag_8GeTe_6 however $\vec{k}$ is no longer a good quantum number due to the *dynamic* disorder introduced by the anharmonic potential at each lattice site. Clearly thermal vibrations will cause the atoms in a harmonic crystal at finite temperature to deviate from their equilibrium positions (lattice points), which has lead some people to loosely consider phonons as dynamic imperfections; however, in the case of harmonic potentials the atomic positions will be exactly their equilibrium values when averaged over time. In this sense it is difficult to justify the classification of harmonic phonons as dynamic imperfections. This is not the case if the potentials of each site are anharmonic. In this case when averaged over time the atomic positions of the atoms will not perfectly coincide with their lattice points. Therefore k is not a good quantum number. This fact that *k* is not a good quantum number is also present in amorphous materials, but for subtly different reasons. In an amorphous material the disorder that leads to the breakdown of the infinitely periodic lattice is *static*, but in the case of crystalline materials with strong anharmonicity this disorder is *dynamic* in nature, which invokes the time domain adding a degree of freedom to the system. This suggests that by introducing strong anharmonicity to a crystalline material it is possible to mimic the thermal properties of an amorphous material. Furthermore in the case of strong anharmonicity the

phonon relaxation must be considered in the context of energy, and in this way the phonon mean free lifetime can be shorter than the value assumed by the Cahill model.

Interestingly similar behavior has been observed in phase change materials with similar atomic compositions to Ag_8GeTe_6. A very informative study by Matsunaga et al. directly probes the differences in lattice dynamics between the crystalline and amorphous phases of $GeSb_2Te_4$ materials.[113] This study is very usefully when considering the thermal properties of Ag_8GeTe_6 because it offers a direct comparison between amorphous and crystalline phases of the same material. Indeed Matsunaga et al. argue that the unlike the amorphous phase which shows harmonic atomic potentials the unusual vibrational and therefore thermal properties of the crystalline phase can be largely understood by strong anharmonicity.

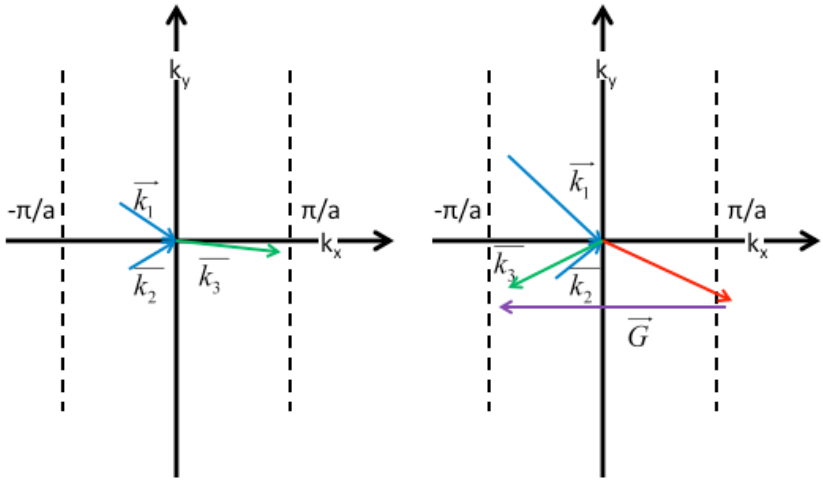

Figure 6.1: Diagram of the difference between a) normal processes and b) Umklapp processes in *2-d*.

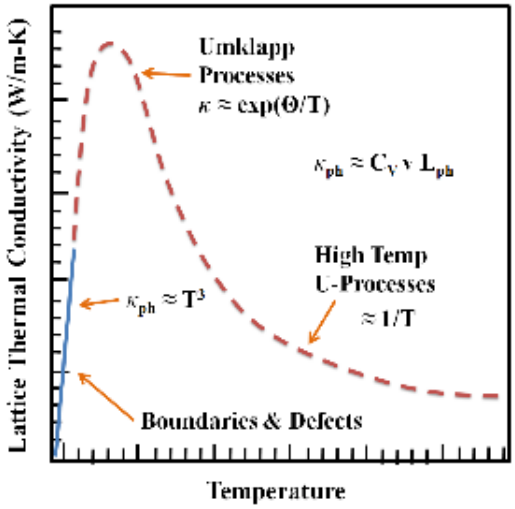

Figure 6.2: Example of a thermal conductivity versus temperature for a typical crystaline material where different scattering mechanisms dominate in different temperature regions. *Source Ref. [95]*

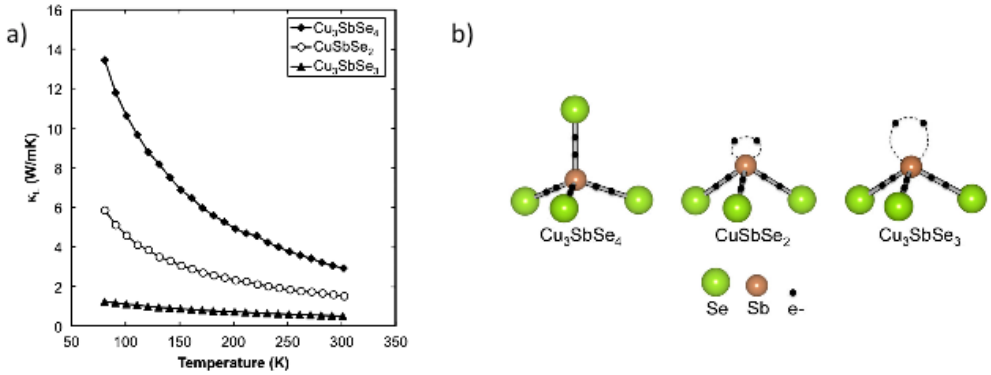

Figure 6.3: a) Lattice thermal conductivity of Cu_3SbSe_4, $CuSbSe_2$, and Cu_3SbSe_3 as a function of temperature b) the differences in thermal conductivity have been attributed to lone pair induced anharmoniciy *Source Ref. [104]*

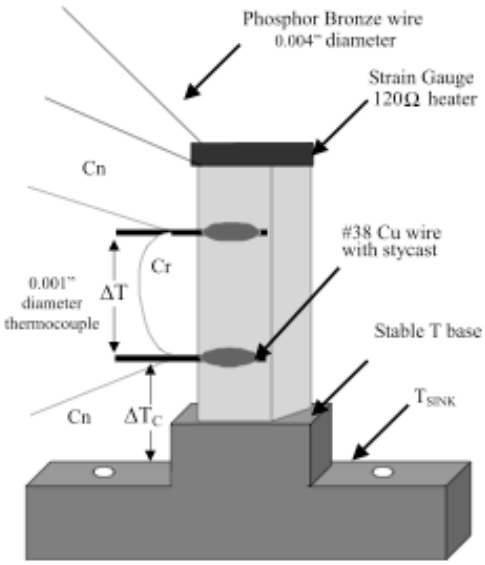

Figure 6.4: Diagram of the sample mount for thermal conductivity measurements. *Source Ref. [107]*

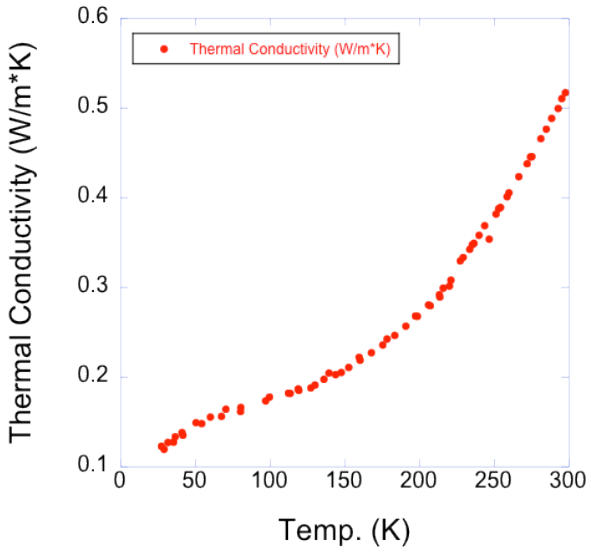

Figure 6.5: Measured thermal conductivity of Ag_8GeTe_6. The upturn in the thermal conductivity versus temperature plot can be at least *partially* attributed to the onset of a radiation contribution.

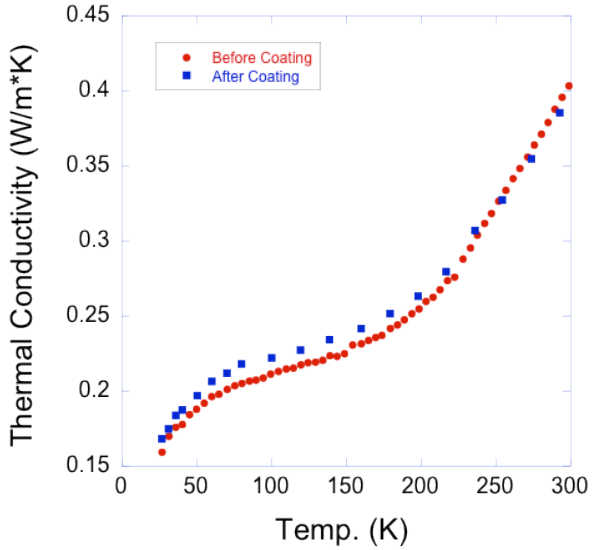

Figure 6.6: Measured thermal conductivity of Ag_8GeTe_6 before and after the application of a graphite coating to the surface of the sample.

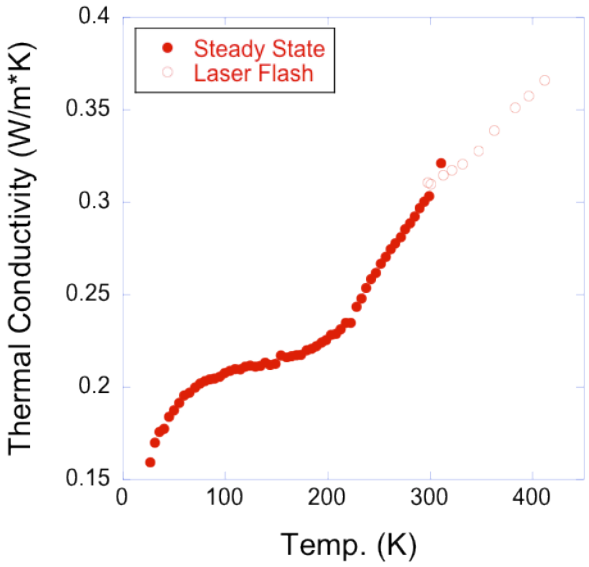

Figure 6.7: Thermal conductivity of Ag_8GeTe_6 after the radiation correction.

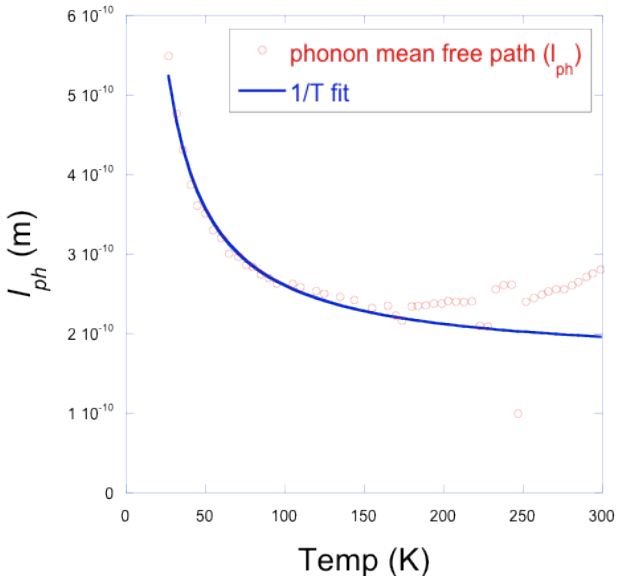

Figure 6.8: Estimated phonon mean free path for Ag_8GeTe_6. as well as fit to a T^{-1} power law as expected for a crystalline material .

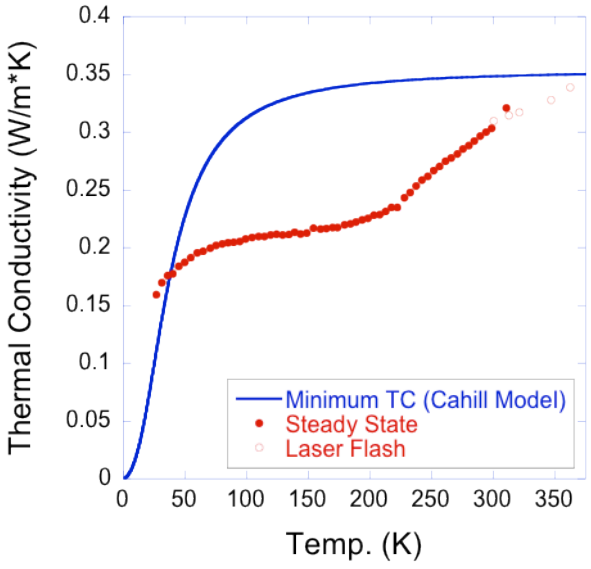

Figure 6.9: The calculated minimum thermal conductivity of Ag_8GeTe_6 plotted along with the measured thermal conductivity as a function of temperature.

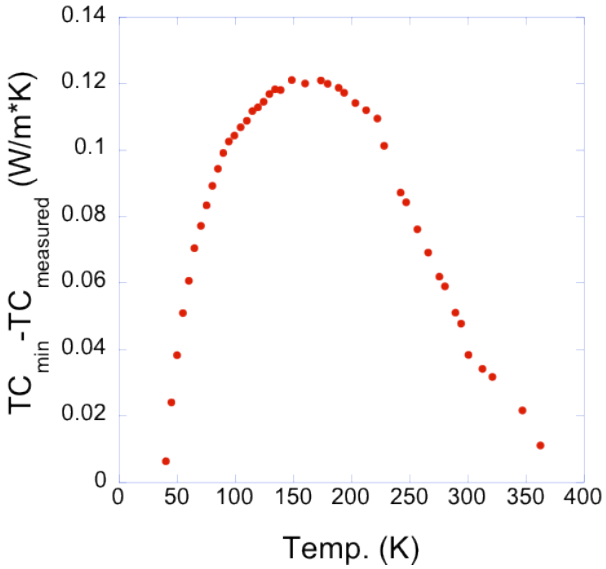

Figure 6.10: The measured thermal conductivity of Ag_8GeTe_6 subtracted from calculated minimum as a function of temperature.

CHAPTER SEVEN

CONCLUSIONS AND FUTURE WORK

The initial goal of this project was to study the enhancement in the power factor in mixed conductor thermoelectric materials due to the increased entropy carried by mobile ions when compared to electrons or holes. In the case of Ag_8GeTe_6 we were not able to realize this goal, however, our studies suggested that mixed conductors may be promising candidates for thermoelectric applications due to their thermal properties.

In the case of Ag_8GeTe_6, we have attributed the unusually low thermal conductivity to two factors: 1) low lying optical or Einstein modes in the phonon dispersion and 2) strong anharmonicity. The presence of low lying optical modes is evidenced by the so called Boson peak in the low temperature specific heat, while the strong anharmonicity is evidenced by the deviation of the specific heat from the Dulong-Petit limit as well as the inherently unstable nature of the crystal structure (the large number of phase transitions between 150 K and 250 K).

Furthermore, the main observation of this thesis is the fact that anharmonicity plays a similar role in the time domain to amorphicity in the spatial domain. In this vein, we have shown that strong anharmonicity offers a route to achieving thermal conductivity values lower than the so-called amorphous limit, a feat that is usually considered impossible.

Clearly the best evidence of this behavior would be in the form of the phonon density of states and dispersion of Ag_8GeTe_6, however, at this point that information is still lacking. In collaboration with Xing Gao we attempted to calculate the phonon

dispersion of Ag_8GeTe_6, but due to computing restraints were unsuccessful (the crystal structure of Ag_8GeTe_6 is so complicated that first principles calculations are incredibly time consuming). We were however successful in calculating the phonon dispersion and density of states of $Ag_{12}GeTe_6$, a theoretical compound with the same crystal structure as Ag_8GeTe_6 but with a higher silver occupancy, shown in **Figure 7.1**. The calculated spectrum shows three interesting features. First, the PDOS shows a low energy "hump" which likely corresponds to the "Boson peak" we observed in low temperature specific heat measurements. Second, the small "humps" at frequency=0, appear to be phonon "instabilities", which are usually a signature of "anharmonicity" though at this point it is difficult to say whether they are real or an artifact of the calculation. Finally, the large band gap from 210 cm^{-1} to 250cm^{-1} (~ 26 meV to 31 meV), and the "flat" bands near the gap suggests another factor that may contribute to the low thermal conductivity of Ag_8GeTe_6 especially in the region of the observed "plateau". To confirm the accuracy of the calculated spectrum we have submitted a beamline proposal for inelastic neutron scattering, but at this point it has not been accepted.

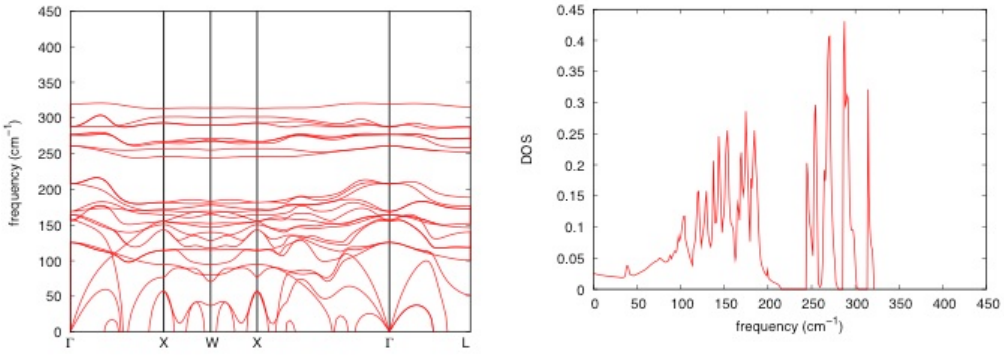

Figure 7.1: Phonon dispersion and Phonon Density of States (DOS) calculated using Quantum Espresso of $Ag_{12}GeTe_6$ a theoretical compound that is isostructural with Ag_8GeTe_6, but has a higher silver occupancy.

References

[1] T.M. Tritt NanoTX'07 Conference, Oct. 2-4, 2007, Dallas.
[2] A.F. Ioffe, L.S. Stil'bans, E.K. Iordanishvili, T.S. Stavitskaya, and A. Gelbtuch, Semiconductor Thermoelements and Thermoelectric Cooling (Infosearch, London, 1957).
[3] T.C. Holgate, Thermoelectric Properties of Nickel and Titanium Co-Intercalated Titanium Diselenide. PhD thesis, Clemson University, (2011).
[4] D. Thompson, Thermoelectric Properties of Silicon Germanium: An In-depth Study to the Reduction of Lattice Thermal Conductivity. PhD thesis, Clemson University, (2012).
[5] W. Thompson, Collected Papers I (University Press, Cambridge, 1882), 232-291.
[6] L. Onsager, "Reciprocal Relations in Irreversible Process" *Phys. Rev.* **37** (1931) 405-426.
[7] H.B. Callen, "The Application of Onsager's Reciprocal Relations to Thermoelectric, Thermomagnetic, and Galvomagnetic Effects" *Phys. Rev.* **73** (1948) 1349-1358.
[8] T. J. Seebeck (1826) "Ueber die Magnetische Polarisation der Metalle und Erze durch Temperatur-Differenz," (On the magnetic polarization of metals and minerals by temperature differences), Annalen der Physik und Chemie, 6 : 1-20, 133-160, 253-286.
[9] D. Griffiths. Introduction to Electrodynamics, Chapter 7 (Prentice Hall, New Jersey, 1999).
[10] P. M. Chaikin "An Introduction to Thermopower for Those Who Might Want to Use It to Study Organic Conductors and Superconductors", 101-115, Organic Superconductivity, edited by V.Z. Kresin and W.A. Little (Springer, New York, 1990)
[11] D.R. Brown, T. Day, K.A. Borup, S. Christensen, B.B. Iversen, and G.J. Snyder "Phase transition enhanced thermoelectric figure-of-merit in copper chalcogenides" *APL Mater.* **1** (2013) 052107.
[12] M. Cutler, N.F. Mott, "Observation of Anderson Localization in an Electron Gas" *Phys. Rev.* **181** (1969) 1336-1340.
[13] V.Y. Irkhin and Y.P. Irkhin, "Electronic Structure, Correlated Effects and Physical Properties of d- and f-transition metals and their compounds, Cambrdige Int. Science Publishing, 2007.
[14] C.B. Vining, "The thermoelectric process", 3-13, Materials Research Society Symposium Proceedings:Thermoelectric Materials - New Directions and Approaches, edited by T.M. Tritt, M. Kanatzidis, H.B. Lyon, and G. Mahan (Materials Research Society, Warrendale, PA, 1997)
[15] A. Shakouri, "Recent Developments in Semiconductor Thermoelectric Physics and Materials" *Annu. Rev. Mater. Res.* **41** (2011) 399-431.
[16] P. Jacquod, R.S. Whitney, J. Meair, and M. Büttiker, "Onsager relations in coupled electric, thermoelectric, and spin transport: The tenfold way" *Phys. Rev. B* **86** (2012) 155118.
[17] M. S. Whittingham, "Mixed Conductors: Synthesis, Properties, Applications" *Mater. Res. Bull.* **14** (1989) 31-38, and the references therein.

[18] H. Liu, X. Shi, F. Xu, L. Zhang, W. Zhang, L. Chen, Q. Li, C. Uher, T. Day, and G.J. Snyder, "Copper ion liquid-like thermoelectrics" *Nat. Matter.* **11** 422-425 (2012).
[19] A. Charoenphakdee, K. Kurosaki, H. Muta, M. Uno, and S. Yamanaka, "Reinvestigation of the thermoelectric properties of Ag_8GeTe_6" *Phys. Status Solidi RRL* **2** (2008) 65–67.
[20] T.J. Zhu, S.N. Zhang, S.H. Yang, and X.B. Zhao, "Improved thermoelectric figure of merit of self-doped $Ag_{8-x}GeTe_6$ compounds with glass-like thermal conductivity" *Phys. Status Solidi RRL* **4** (2010) 317–319.
[21] F. Boucher, M. Evain, and R. Brec, "Distribution and Ionic Diffusion Path of Silver in γ-Ag_8GeTe_6: A Temperature Dependent Anharmonic Single Crystal Structure Study" *J. Solid State Chem.* **107** (1993) 332-346.
[22] V.K. Zaitsev and M.I. Fedorov, "Thermal Conductivity of Semiconductors with Complex Crystal Structures" Chapter 6 of Thermoelectrics Handbook: Macro to Nano, edited by DM Rowe. (CRC Press, Boca Raton, FL, 2006).
[23] private communications with Prof. T. J. Zhu
[24] J. Jin Preparation and Optimization of Low Thermal Conductivity Thermoelectric Tellurides, MS Thesis, Zhejiang University (2012).
[25] M. Fujikane, K. Kurosaki, H. Muta, S. Yamanaka, "Thermoelectric properties of Ag_8GeTe_6" *J. Alloys and Compd*. **396** (2005) 280–282.
[26] S. Geller, "The crystal structure of γ Ag_8GeTe_6, a potential mixed electronic-ionic conductor" *Zeitschrift für Kristallographie* **149** (1979) 31-47.
[27] A. Katty et al. "Etude Radiocristallographique et calorimetrique des transitions de phase de Ag_8GeTe_6" *J. Solid State Chem*. **38** (1981) 259-263.
[28] A. Ferhat, R. Ollitrault-Fichet, and J. Rivet, "Description du systeme ternaire Ag-Ge-Te" *J. Alloys and Compd* **177** (1991) 337-355.
[29] D. Thompson, D. Hitchcock, A. Lahwal, T.M. Tritt, "Single-element spark plasma sintering of silicon germanium". *Emerging Materials Research* **1** (2012) 299-305.
[30] private communications with Dr. Fivos Drymiotis
[31] S. Geller, "Halogenide solid electrolytes" In: Topics in Applied Physics, Vol.21, Solid electrolytes Herausgeb. S. Geller. (Springer-Verlag, Berlin-Heidelberg-New York 1977)
[32] N. Rysanek, P. Laruelle, and A. Katty, "Structure cristalline de Ag_8GeTe_6 (γ)" *Acta Crystallogr* **B32** (1976) 692-696.
[33] J. von Unterrichter and K.J. Range, "Ag_8GeTe_6, a Representative of the Argyrodite Family" *Z. Naturforsch* **38b** (1978) 866-872.
[34] E. Gaudin, F. Boucher, V. Petricek, F. Taulellec, and M. Evain "Structures and phase transitions of the A_7PSe_6 (A = Ag, Cu) argyrodite-type ionic conductors. I. Ag_7PSe_6" *Acta Cryst*. **B54** (1998) 376-383.
[35] E. Gaudin, F. Boucher, V. Petricek, F. Taulellec, and M. Evain, "Structures and phase transitions of the A_7PSe_6 (A = Ag, Cu) argyrodite-type ionic conductors. II. β- and γ-Cu_7PSe_6" *Acta Cryst*. **B56** (2000) 402-408.

[36] E. Gaudin, F. Boucher, V. Petricek, F. Taulellec, and M. Evain, "Structures and phase transitions of the A_7PSe_6 (A = Ag, Cu) argyrodite-type ionic conductors. III. α-Cu_7PSe_6" *Acta Cryst.* **B56** (2000) 972-979.
[37] H. Kawaji and T. Atake, "Heat capacity measurement and thermodynamic study of Ag_8GeTe_6" *Sol. State Ionics* **70/71** (1994) 518-521.
[38] O. Gorochov, "The Compounds Ag_8MX_6 (M = Si, Ge, Sn; X = S, Se, Te)" (in French) *Bull. Soc. Chim. Fr.* (1968) 2263-2275.
[39] Units for Magnetic Properties R.B. Goldfarb and F.R. Picket National bureau of Standards Boulder CO March 1985
[40] "Selected diamagnetic ionic susceptibilities, Pascal constants, and one-electron spin-orbit coupling constants" E Koinig and G. Konig Magnetic Properties of Coordination and Organometallic Transition Metal Compounds Landolt-Börnstein - Group II Molecules and Radicals Volume 11, 1981, pp 27-29
[41] Quantum Design Physical Property Measurement System (PPMS) Vibrating Sample Magnetometer Application Note
[42] I. Riess, "Measurements of electronic and ionic partial conductivities in mixed conductors, without the use of blocking electrodes" *Solid State Ionics* **44**(1991) 207–214.
[43] A. Lehmani, P. Turq, M. Périé, J. Périé, J.P. Simonin, "Ion transport in Nafion® 117 membrane" *J. Eleetroanal. Chem.* **428** (1997) 81-89.
[44] Y. Sone, P. Ekdunge, and Daniel Simonsson, "Proton Conductivity of Nafion 117 as Measured by a Four-Electrode AC Impedance Method" *J. Electrochem. Soc.* **143** (1996) 1254-1259.
[45] A.L. Pope, T.R. Littleton, and T.M. Tritt, "Apparatus for the rapid measurement of electrical transport properties for both "needle-like" and bulk materials" *Rev. Sci. Instrum.* **72** (2001) 3129-3131.
[46] PPMS AC Transport Option User's Manual, Rev. D-1 page 1-1 section 1.2 October 15, 2003
[47] A.L. Pope, B. Zawilski, T.M. Tritt, "Description of removable sample mount apparatus for rapid thermal conductivity measurements" *Cryogenics* **41** (2001) 725–731.
[48] S-H Park and H Yoo, "Thermoelectric behavior of a mixed ionic electronic conductor, $Ce_{1-x}Gd_xO_{2-x/2-\delta}$" *Phys. Chem. Chem. Phys.* **11** (2009) 391–401.
[49] K. Koumoto, I. Terasaki, and R. Funahashi, "Complex Oxide Materials for Potential Thermoelectric Applications" *Mater. Res. Bull.* **31**(2006) 206-210.
[50] B. Yu, Bo, M. Zebarjadi, K. Lukas, H. Wang, H. Wang, C. Opeil, M.S. Dresselhaus, G. Chen, and Z.F. Ren, "Enhancement of thermoelectric properties by modulation-doping in silicon germanium alloy nanocomposites" *Nano Lett.* **12** (2012) 2077-2082.
[51] N.F. Mott, "Conduction in non-crystalline materials" *Phil. Mag.* **19** (1969). 835-852.
[52] B.I. Shklovskii, A.L. Efros Electronic properties of doped semiconductors (Springer, Berlin, Heidelberg, New York, 1984)
[53] E. Velmre and A. Udal, "Modeling of charge carrier non-isothermal transport in silicon and silicon carbide" *Proc. Estonian Acad. Sci. Eng.* **6** (2000) 144-154.
[54] H.P.R. Frederikse, "Modeling the thermoelectric power of germanium below room temperature" *Phys. Rev.* **92** 248-252.

[55] W. van Gool, "Fast Ion Conduction" *Annu. Rev. Mater. Sci.* **4** (1974) 311-335.
[56] M. Grünewald, M. Müller, P. Thomas, D. Würtz, "The hopping hall mobility — A percolation approach" *Solid State Commun.* **38** (1981) 1011-1014.
[57] A.G. Bell, "On the production and reproduction of sound by ligh" *Am. J. Sci.* **20** (1880) 305–324.
[58] R. Bendorius, A. Irzikevicius, A. Kindurys, and E. V. Tsvetkova, "The absorption spectra of $Ag_8M^{IV}Se_6$ and $Ag_8GeX_6^{VI}$ compounds" *Physica Stat. Sol. A* **28** (1975) K125-K127.
[59] K. S. Weldert, W.G. Zeier, T.W. Day, M. Panthöfer, G. J. Snyder, and W. Tremel, "Thermoelectric Transport in Cu_7PSe_6 with High Copper Ionic Mobility" *J. Am. Chem. Soc.* **136** (2014) 12035−12040.
[60] H. Wu, W. Foo, S. Chen, and G. J. Snyder, "Ternary eutectic growth of nanostructured thermoelectric Ag-Pb-Te Materials" *Appl. Phys. Lett.* **101** (2012) 023107.
[61] Quantum Design Physical Property Measurement System User's manual (2000)
[62] J. S. Hwang, K. J. Lin, and C. Tien, "Measurement of heat capacity by fitting the whole temperature response of a heat-pulse calorimeter" *Rev. Sci. Instrum.* **68** (1997) 94-101.
[63] G. Höhne, W. Hemminger, and H.-J. Flammersheim, Differential Scanning Calorimetry (Springer-Verlag, Berlin/Heidelberg/New York, 2001)
[64] J.C. Lashley, M.F. Hundley, A. Migliori, J.L. Sarrao, P.G. Pagliuso, T.W. Darling, M. Jaime, J.C. Cooley, W.L. Hults, L. Morales, D.J. Thoma, J.L. Smith, J. Boerio-Goates, B.F. Woodfield, G.R. Stewart, R.A. Fisher, and N.E. Phillips, "Critical examination of heat capacity measurements made on a Quantum Design physical property measurement system" *Cryogenics* **43** (2003) 369-387.
[65] D. R. Brown, T. Day, K. A. Borup, S. Christensen, B. B. Iversen, and G. J. Snyder, "Phase transition enhanced thermoelectric figure-of-merit in copper chalcogenides" *APL Mater.* **1** (2013) 052107.
[66] A. Petit and P. Dulong, "Recherches sur quelques points importants de la Théorie de la Chaleur" *Ann. Chim. Phys.* **10** (1819) 395-413. English translation: *Ann. of Phil.* **14** (1819) 189-198.
[67] A. Einstein, "Die Plancksche Theorie der Strahlung und die Theorie der spezifischen Wärme" *Annalen der Physik* **22** (1907) 180–190.
[68] P. Debye, "Zur Theorie der spezifischen Waerme" *Ann. Phys. (Leipzig)* **39** (1912) 789.
[69] C. Kittel, Introduction to Solid State Physics, 8th Ed. (John Wiley and Sons, New York, 2005).
[70] A. V. Sologubenko, E. Felder, K. Giannò, H. R. Ott, A. Vietkine, and A. Revcolevschi, "Thermal conductivity and specific heat of the linear chain cuprate Sr_2CuO_3: Evidence for thermal transport via spinons" *Phys. Rev. B* **62** (2000) R6108-R6111.
[71] H.M. Rosenberg Low Temperature Solid State Physics Chap. 2 (Oxford University Press, London, 1963).

[72] J. Graff, S. Zhu, T. Holgate, J. Peng, J. He, and T.M. Tritt, "High-Temperature Thermoelectric Properties of Co_4Sb_{12}-Based Skutterudites with Multiple Filler Atoms: $Ce_{0.1}In_xYb_yCo_4Sb_{12}$" *J. Electron. Mater.* **40** (2011) 696-701.
[73] B. C. Sales, D. Mandrus, and B. C. Chakoumakos, Chap. 1, pp. 1–34 of Recent Trends in Thermoelectric Materials Research II, Semiconductors and Semimetals **70**, edited by T. M. Tritt (Academic, San Diego, 2001).
[74] B.C. Sales, B. C. Chakoumakos, and D. Mandrus, "Thermoelectric Properties of Thallium-Filled Skutterudites" *Phys. Rev. B* **61** (2000) 2475-2481.
[75] B. C.Sales, D. Mandrus, B.C. Chakoumakos, V. Keppens, and J.R. Thompson, "Filled Skutterudite Antimonides: Electron Crystals and Phonon Glasses", *Phys. Rev. B* **56** (1997) 15081.
[76] H. Shintani and H. Tanaka, "Universal link between the boson peak and transverse phonons in glass" *Nature Materials* **7** (2008) 870–877.
[77] W. Schirmacher, G. Diezemann, and C. Ganter, "Harmonic Vibrational Excitations in Disordered Solids and the "Boson Peak" *Phys. Rev. Lett.* **81** (1998) 136-139.
[78] U. Buchenau, N. Nuucker, and A.J. Dianoux, "Neutron Scattering Study of the Low-Frequency Vibrations in Vitreous Silica" *Phys. Rev. Lett.* **53** (1984) 2316-2319.
[79] A. P. Sokolov, A. Kisliuk, M. Soltwisch, and D. Quitmann," Medium-range order in glasses: Comparison of Raman and diffraction measurements" *Phys. Rev. Lett.* **69** (1992) 1540-1543.
[80] B. Fultz, "Vibrational Thermodynamics of Materials" *Prog. Mater. Sci.*, **55** (2010) 247-352.
[81] M. D. Nielsen, V. Ozolins, and J.P. Heremans, "Lone pair electrons minimize lattice thermal conductivity" *Energ. Environ. Sci.* **6** (2013) 570–578.
[82] S. Ganesan, "Temperature variation of the grüneisen parameter in magnesium oxide" *Philos. Mag.* **7** (1962) 197-205.
[83] D.T. Morelli, V. Jovovic, and J.P. Heremans, "Intrinsically minimal thermal conductivity in cubic I-V-VI2 semiconductors" *Phys. Rev. Lett.* **101** (2008) 035901.
[84] L.D. Zhao, S.H. Lo, Y. Zhang, H. Sun, G. Tan, C. Uher, C. Wolverton, V. P. Dravid, and M. G. Kanatzidis, "Ultralow thermal conductivity and high thermoelectric figure of merit in SnSe crystals" *Nature* **508** (2014) 373–377.
[85] Y. Matsushita, H. Bluhm, T. H. Geballe, and I. R. Fisher, "Evidence for Charge Kondo Effect in Superconducting Tl-Doped PbTe" *Phys. Rev. Lett.* **94** (2005) 157002.
[86] Y. He, T. Day , T. Zhang , H. Liu , X. Shi, L. Chen, and G. J. Snyder, "High Thermoelectric Performance in Non-Toxic Earth-Abundant Copper Sulfide" *Adv. Mater.* **26** (2014) 3974–3978.
[87] G.A. Breaux, C.M. Neal, B. Cao, and M.F. Jarrold, "Melting, Premelting, and Structural Transitions in Size--Selected Aluminum Clusters with around 55 Atoms" *Phys. Rev. Lett.* **94** (2005) 173401.
[88] J. F. Scott, H. G. Bohn, and W. Schenk, "Ionic Wiedemann–Franz law" *Appl. Phys. Lett.* **77** (2000) 2599-2600.

[89] A. F. May and G.J. Snyder, Thermoelectrics Handbook:Thermoelectrics and its Energy Harvesting Chap. 11 edited by D.M. Rowe (CRC Press, Boca Raton, 2012).
[90] A. Sommerfeld, "Zur Elektronentheorie der Metalle" *Naturwissenschaften* **15** (1927) 825.
[91] G. S. Kumar, G. Prasad, and R. O. Pohl, "Experimental determinations of the Lorenz number" *J Mater Sci* **28** (1993) 4261-4272.
[92] C. Kittel, Introduction to Solid State Physics, 8th Ed. (John Wiley and Sons, New York, 2005).
[93] R.E. Peierls, "Zur kinetischen Theorie der Warmeleitung in Kristallen" *Ann. Phys.* **3** (1929) 1055-1101.
[94] David G. Cahill and R. O. Pohl "Lattice Vibrations and Heat Transport in Crystals and Glasses" *Ann. Rev. Phys. Chem.* **39** (1988) 93-121.
[95] T.M. Tritt. Thermal Conductivity: theory, properties, and applications (Kluwer Academic/Plenum Publishers, New York, 2004).
[96] S. Hunklinger, "phonons of amorphous materials" *Journal de Physique Colloques* **43**(C9) (1982) 461-474.
[97] D.T. Morelli and G.A. Slack, "High Lattice Thermal Conductivity Solids," pp. 37-64 in High Thermal Conductivity edited by S. Shinde and J. Goela (Springer, New York, 2005).
[98] J. Callaway, "Model for Lattice Thermal Conductivity at Low Temperatures" *Phys. Rev.* **113** (1959) 1046-1051.
[99] C. Kittel, "Interpretation of the Thermal Conductivity of Glasses" *Phys. Rev.* **75** (1949) 972-974.
[100] D.G. Cahill and R.O. Pohl, "Heat Flow and Lattice Vibrations in Glasses" *Solid State Commun.* **70** (1989) 927-930.
[101] G. A. Slack, "Nonmetallic Crystals with High Thermal Conductivity" *J. Phys. Chem. Solids* **34** (1973) 321-335.
[102] G. A. Slack, "The Thermal Conductivity of Nonmetallic Crystals" *Solid State Phys.* **34** (1979) 1-71.
[103] D.T. Morelli, V. Jovovic, and J.P. Heremans, "Intrinsically Minimal Thermal Conductivity in Cubic I-V-VI2 Semiconductors" *Phys. Rev. Lett.* **101** (2008) 035901.
[104] E.J. Skoug and D.T. Morelli "Role of lone-pair electrons in producing minimum thermal conductivity in nitrogen-group chalcogenide compounds." Phys Rev Lett. **107** (2011) 235901.
[105] M. D. Nielsen, V. Ozolins, and J.P. Heremans, "Lone Pair Electrons Minimize Lattice Thermal Conductivity" *Energ. Environ. Sci.* **6** (2013) 570–578.
[106] X. Wang and F. Liebau, "Studies on bond and atomic valences. I. correlation between bond valence and bond angles in SbIII chalcogen compounds: the influence of lone-electron pairs" *Acta Crystallogr.* **B52** (1996) 7-15.

[107] A. L. Pope, R. T. Littleton, and Terry M. Tritt, “Apparatus for the rapid measurement of electrical transport properties for both “needle-like” and bulk materials” *Rev. Sci. Instrum.* **72** (2001) 3129-3131.
[108] W.J. Parker, R.J. Jenkins, C.P. Butler, and G.L. Abbott, "Method of Determining Thermal Diffusivity, Heat Capacity and Thermal Conductivity" *J. Appl. Phys.* **32** (1961) 1679-1684.
[109] R.D. Cowan, "Pulse Method of Measuring Thermal Diffusivity at High Temperatures" *J. Appl. Phys.* **34** (1963) 926-927.
[110] O.L. Anderson, “The Debye Temperature of Vitreous Silica” *J. Phys. Chem. Solids* **12** (1959) 41-52.
[111] D.T. Morelli and J. P. Heremans, “Thermal conductivity of germanium, silicon, and carbon nitrides” *Appl. Phys. Lett.* **81** (2002) 5126-5128.
[112] C. Chiritescu, D.G. Cahill, N. Nguyen, D. Johnson, A. Bodapati, P. Keblinski, P. Zschack, “Ultralow Thermal Conductivity in Disordered, Layered WSe_2 Crystals” *Science* **19** (2007) 351-353.
[113] T. Matsunaga , N. Yamada, R. Kojima, S. Shamoto, M. Sato, H. Tanida, T. Uruga, S. Kohara, M. Takata, P. Zalden, G. Bruns, I. Sergueev, H.C. Wille, R.P. Hermann, and M. Wuttig, “Phase-Change Materials: Vibrational Softening upon Crystallization and Its Impact on Thermal Properties” *Adv. Funct. Matter.* **21** (2011**)** 2232-2239.